Old Dominion University

ODU Digital Commons

Winter 2018

Computational Investigation of Energetic Materials: Influence of Intramolecular and Intermolecular Interactions on Sensitivity

Ashley Lauren Shoaf
Old Dominion University, ashoa001@odu.edu

Follow this and additional works at: https://digitalcommons.odu.edu/chemistry_etds

Part of the Numerical Analysis and Computation Commons, and the Physical Chemistry Commons

Recommended Citation

COMPUTATIONAL INVESTIGATION OF ENERGETIC MATERIALS: INFLUENCE OF

INTRAMOLECULAR AND INTERMOLECULAR INTERACTIONS ON SENSITIVITY

by

Ashley Lauren Shoaf
B.S. May 2013, Palm Beach Atlantic University

A Dissertation Submitted to the Faculty of
Old Dominion University in Partial Fulfillment of the
Requirements for the Degree of

DOCTOR OF PHILOSOPHY

CHEMISTRY

OLD DOMINION UNIVERSITY
December 2018

Approved by:

Craig A. Bayse, Director

Alvin Holder, Member

Bala Ramjee, Member

Jennifer Poutsma, Member

Lepsha Vuskovic, Member

ABSTRACT

COMPUTATIONAL INVESTIGATION OF ENERGETIC MATERIALS: INFLUENCE OF
INTRAMOLECULAR AND INTERMOLECULAR INTERACTIONS ON SENSITIVITY

Ashley Lauren Shoaf
Old Dominion University, 2018
Director: Dr. Craig A. Bayse

The development of novel high energy density materials (HEDMs) with superior energetic
properties depends on characterizing how and why detonation occurs. Detonation is highly
energetic and a nearly instantaneous process, making experimental studies challenging; thus,
computational modeling through density functional theory (DFT) and molecular dynamics (MD)
can be used to propose weakened, or activated, bonds that break to initiate explosive
decomposition, termed trigger bonds. Bond activation is characterized by the Wiberg bond index
(WBI), a measure of interatomic electron density. Trigger bonds in HEDMs are commonly found
in explosophores, functional groups that contribute to energetic potential such as $X-NO_2$
($X=N,C,O$) and $N-N_2$ linkages. Comparison of WBIs of potential trigger bonds to the same bond
type in reference molecules provides a relative scale for bond activation (%ΔWBIs) which could
be used to screen novel HEDMs for trigger bonds and potentially guide development of new
materials.

%ΔWBIs of nitroaromatic energetic materials indicate that intramolecular hydrogen
bonding deactivates $C-NO_2$ bonds through resonance, while steric effects activate trigger bonds
by increasing $C-NO_2$ dihedral angles. In aromatic azide-based and azole-based energetic materials,
%ΔWBIs and activation energies predict that that the $N-N_2$ bond of the azide and $N-NO_2$ are more
activated than $C-NO_2$. An *ortho* nitro group to an azide yields a lower activation energy for N_2

extrusion from the azide. Thus, %ΔWBIs only provide a clue into the influence of intramolecular interactions on the sensitivity of trigger bonds.

Detonation is unique to the solid state, making condensed-phase calculations necessary to characterize the effect of intermolecular interactions on trigger bond sensitivity. In models of ammonium nitrate, increased pressure compresses the unit cell and hydrogen bonding between ions becomes stronger. In molecular dynamics simulations at high pressure, hydrogen transfer from ammonium to nitrate producing ammonia and nitric acid, the initiation step for explosive decomposition, is observed around 40 GPa. These condensed-phase calculations can be extended to characterize the effect of pressure on intramolecular and intermolecular interactions to provide information that can be used to guide the synthesis of novel energetic materials.

This dissertation is dedicated to my parents, Jeff and Tami Shoaf.

ACKNOWLEDGEMENTS

I would first like to thank my advisor, Dr. Craig Bayse, for all of his guidance, direction, assistance, encouragement, and support throughout my time at Old Dominion University and for fostering my skills in research and writing. Thank you for pushing me to pursue high quality work. I would also like to thank my committee members, Dr. Alvin Holder, Dr. Jennifer Poutsma, Dr. Bala Ramjee, and Dr. Vuskovic for their guidance and support.

I am grateful to the Virginia Space Grant Consortium for graduate fellowships (2016-2018), the ODU College of Sciences for the Graduate Dominion Scholar Award (2016-2018) and ODU for summer funding through CIBA Scholarships (2015-2016). I am also thankful to ODU Information Technology Services for managing the Turing High-Performance Cluster, which was integral for my research. I would like to thank the ODU Chemistry Department for giving me this opportunity, and I am thankful to the faculty and staff for being helpful and kind throughout my time at ODU. To my former labmates in Dr. Bayse's lab, Patricia and Lenora, thank you for your encouragement over the years. I would also like to thank my current labmates, Eric and Ana, for their support. I wish you the best in your career endeavors.

I am thankful to my parents, Jeff and Tami, for their continuous support. They taught me to trust God, to be committed to my work, and to strive for excellence. I am incredibly grateful for all that you have done and continue to do for me. I want to give glory to my LORD and Savior, Jesus Christ, who has given me the strength, knowledge and ability to complete my degree. I am also thankful for my family and friends for keeping me in their prayers, offering encouragement, and supporting me throughout this process.

NOMENCLATURE

DFT   Density functional theory

MD   Molecular dynamics

PBC   Periodic boundary conditions

WBI   Wiberg bond index

BDE   Bond dissociation energy

AIM   Atoms-In-Molecules

φ Dihedral angle, [°]

d Bond distance, [Å]

I.S.   Impact sensitivity

Ω Oxygen balance

ΔH_F Heat of formation

Q Heat of explosion

V Volume of gas released upon detonation

D Detonation velocity

P Detonation pressure

E.S.   Electrical spark sensitivity

F.S.   Friction sensitivity

ReaxFF   Reactive force fields

NMR   Nuclear magnetic resonance

NB   Nitrobenzene

AzB   Azidobenzene

ESR	Electron-spin resonance
o-NAzB	*o*-nitroazidobenzene
m-NAzB	*m*-nitroazidobenzene
p-NAzB	*p*-nitroazidobenzene
NAB	Nitraminobenzene
MNAB	Methylnitraminobenzene
HEDM	High energy density material
NG	Nitroglycerin
AN	Ammonium nitrate
PA	Picric acid
TNT	2,4,6-trinitrotoluene
TETRYL	2,4,6-trinitrophenylmethylnitramine
PETN	Pentaerythritol tetranitrate
RDX	1,3,5-trinitro-1,3,5-triazacyclohexane
HMX	1,3,5,7-tetranitro-1,3,5,7-tetrazacyclooctane
HpNC	Heptanitrocubane
ONC	Octanitrocubane
CL-20	2,4,6,8,10,12-hexanitro-2,4,6,8,10,12-hexaazaisowurtzitane
HNS	Hexanitrostilbene
TATB	1,3,5-triamino-2,4,6-trinitrobenzene
TNB	Trinitrobenzene
DNB	1,3-dinitrobenzene
TETNB	1,2,3,5-tetranitrobenzene

PNB   Pentanitrobenzene

HNB   Hexanitrobenzene

HNBP   2,2',4,4',6,6'-hexanitrobiphenyl

HNDPM   2,2',4,4',6,6'-hexanitrodiphenylmethane

DNT   2,6-dinitrotoluene

o-TETNT   2,3,4,5-tetranitrotoluene

m-TETNT   2,3,4,6-tetranitrotoluene

p-TETNT   2,3,5,6-tetranitrotoluene

PNT   Pentanitrotoluene

DMTNB   1,3-dimethyl-2,4,6-trinitrobenzene

TMTNB   1,3,5-trimethyl-2,4,6-trinitrobenzene

ATNT   3-amino-2,4,6-trinitrotoluene

o-ATETNT   2-aminotetranitrotoluene

m-ATETNT   3-aminotetranitrotoluene

p-ATETNT   4-aminotetranitrotoluene

ClMTNB   Chloromethyl-2,4,6-trinitrobenzene

TNBMeOH   2,4,6-trinitrobenzenemethanol

TNBEtOH   2,4,6-trinitrobenzeneethanol

DNAN   2,4-dinitroanisole

TNAN   2,4,6-trinitroanisole

ATNAN   3-amino-2,4,6-trinitroanisole

DMOTNB   1,3-dimethoxy-2,4,6-trinitrobenzene

DClTNAN   3,5-dichloro-2,4,6-trinitroanisole

EOTNB	Ethoxy-2,4,6-trinitrobenzene
DMDNPy	2,6-dimethoxy-3,5-dinitropyridine
DNPH	2,4-dinitrophenylhydrazine
TNA	2,4,6-trinitroaniline
DATB	1,3-diamino-2,4,6-trinitrobenzene
TETNA	2,3,4,6-tetranitroaniline
PNA	Pentanitroaniline
DADNPy	2,6-diamino-3,5-dinitropyridine
LLM-105	2,6-diamino-3,5-dinitropyrazine-1-oxide
HNDPA	2,2,',4,4',6,6'-hexanitrodiphenylamine (dipicryl amine)
TETNPO	1,3,7,9-tetranitro-10H-phenoxazine
DAHNBP	3,3'-diamino-2,2',4,4',6,6'-hexanitrobiphenyl
2,4-DNP	2,4-dinitrophenol
2,6-DNP	2,6-dinitrophenol
2,4-DNR	2,4-dinitroresorcinol
4,6-DNR	4,6-dinitroresorcinol
TNR	2,4,6-trinitroresorcinol
THTNB	1,3,5-trihydroxy-2,4,6-trinitrobenzene
MTNP	3-methyl-2,4,6-trinitrophenol
TNAP	4-amino-2,3,5-trinitrophenol
DATNP	3,5-diamino-2,4,6-trinitrophenol
HTNA	3-hydroxy-2,4,6-trinitroaniline
DHTNA	3,5-dihydroxy-2,4,6-trinitroaniline

1,5-DNN	1,5-dinitronaphthalene
1,8-DNN	1,8-dinitronaphthalene
TNN	1,4,5-trinitronaphthalene
TETNN	1,4,5,8-tetranitronaphthalene
ClTNB	Chloro-2,4,6-trinitrobenzene
TNBN	2,4,6-trinitrobenzonitrile
TNBAl	2,4,6-trinitrobenzaldehyde
TNBA	2,4,6-trinitrobenzoic acid
ENTNB	2,4,6-trinitrophenylethanone
METNBA	3-methylester-2,4,6-trinitrobenzoic acid
AzTNB	Azido-2,4,6-trinitrobenzene
AzPNB	Azidopentanitrobenzene
TAzTNB	1,3,5-triazido-2,4,6-trinitrobenzene, crystal structure
TAzTNB-1	1,3,5-triazido-2,4,6-trinitrobenzene, pin-wheel conformation
TAzTNB-2	1,3,5-triazido-2,4,6-trinitrobenzene, azide out of the plane of the ring
1	4-(*N*-methylnitramino)-3,5-dinitropyrazole
2	1-(3,5-dinitropyrazol-4-yl)-3-nitroguanidine
3	*N*-methyl-3,4,5-trinitropyrazole
4	*N*-methyl-4-amino-3,5-dinitropyrazole
5	4-guanidino-3,5-dinitropyrazole
6	*N*-methyl-4-azido-3,5-dinitropyrazole
7	*N*-methyl-3-nitro-4-diazo-5-oxide pyrazole
8	1-amino-4-nitropyrazole

TABLE OF CONTENTS

Page

Page

LIST OF TABLES

LIST OF FIGURES

Figure   Page

LIST OF SCHEMES

CHAPTER 1

INTRODUCTION

Energetic Materials Development

Energetic materials (**Scheme 1**) are desirable for military, aeronautics, mining, sample collection and pyrotechnics applications.[1-3] Due to the ever-changing nature of international conflicts and the increase in terrorism over the past 10 years, the development of high energy density materials (HEDMs) with superior properties are crucial for enhancing current methods and tactics.[1] Furthermore, the synthesis of HEDMs for aeronautics is essential for improving personal safety and reducing environmental contamination.[1-4] Recently, the development of novel HEDMs with similar or superior properties to energetic materials currently applied in advanced weapons systems (i.e., 1,3,5,7-tetranitro-1,3,5,7-tetrazacyclooctane (HMX), **Scheme 1**) and aeronautics (i.e., hydrazine, N_2H_4) has been a priority.[1, 5] However, energetic materials have been of considerable interest since the unintentional discovery of black powder around 220 BC in China.[6]

In the 19th century, however, the limitations of the energetic potential of black powder were determined; thus, investigations into energetic materials specifically with reduced sensitivity became a priority.[7] Alfred Nobel developed nitroglycerine (NG), mercury fulminate ($Hg^{II}(CNO)_2$) blasting caps,[6-8] and dynamite, which is a NG and nitrocellulose gel,[6, 8] as some of the first compounds that were used to replace black powder. Nobel later determined that dynamite was enhanced with ammonium nitrate (AN),[7, 9] but the energetic properties and dangers (i.e., accidental detonation) of AN were not fully understood until after World War II.[7] Picric acid (PA, 2,4,6-trinitrophenol) was formed in the mid-1700s, but was not used as an energetic material until the

---

This dissertation follows the format of *Physical Chemistry Chemical Physics.*

late 19th century.[6] Shortly thereafter, 2,4,6-trinitrotoluene (TNT) and 2,4,6-trinitrophenylmethylnitramine (TETRYL) were discovered,[6] and TNT replaced PA as the standard energetic material for use in World War I.[7] More powerful energetic materials, such as pentaerythritol tetranitrate (PETN), 1,3,5-trinitro-1,3,5-triazacyclohexane (RDX), and 1,3,5,7-tetranitro-1,3,5,7-tetrazacyclooctane (HMX), were also formulated[6, 7] in the late 19th to early 20th centuries for use during World War II.[6, 7] Conventional energetic materials like PETN, RDX and HMX are accepted as standards for energetic properties in the development of novel HEDMs,[5, 6] such as heptanitrocubane (HpNC), octanitrocubane (ONC), 2,4,6,8,10,12-hexanitro-2,4,6,8,10,12-hexaazaisowurtzitane (CL-20), hexanitrostilbene (HNS), and 1,3,5-triamino-2,4,6-trinitrobenzene (TATB). In recent years, research has focused on synthesizing 'green' HEDMs with superior properties compared to energetic materials applied in current systems.[3, 5, 7, 10, 11]
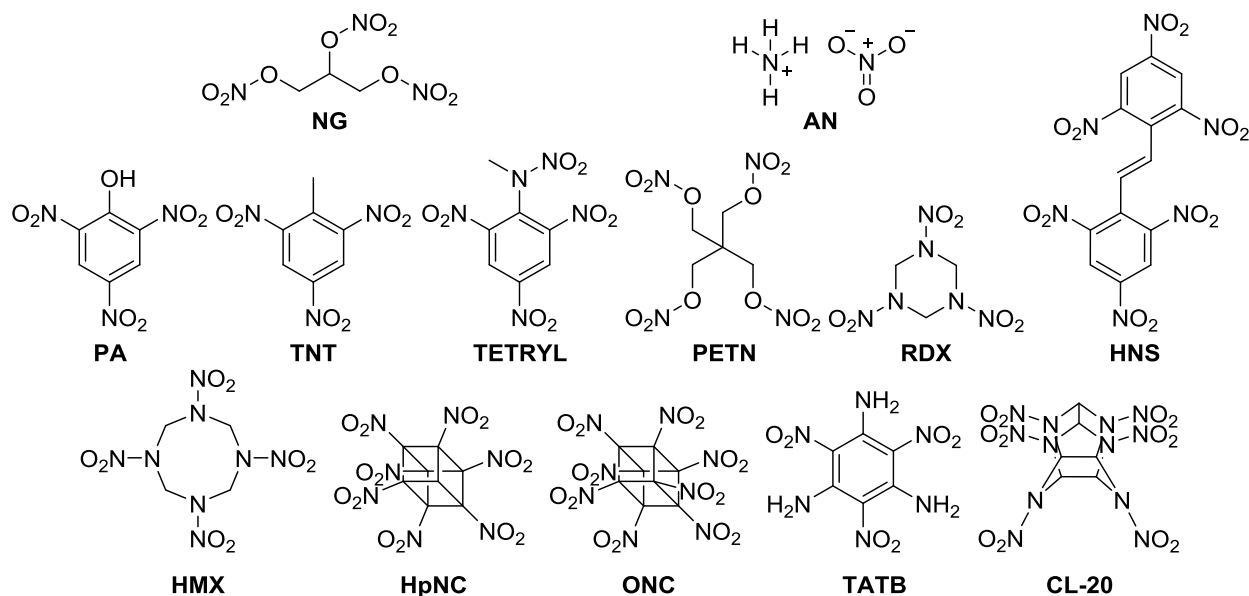
Scheme 1. Examples of conventional energetic materials.

'Green' energetic materials (**Scheme 2**) contain higher nitrogen content (i.e., tetrazoles, pyrazoles, etc.) and are desirable because they modify burn rates,[1, 10] produce nontoxic nitrogen gas,[1, 10] enhance performance,[10] increase stability by greater heats of formation,[8, 10] and improve energetic properties (i.e., impact sensitivity, detonation pressure, etc.).[4] Superior performance, stability, and environmentally-friendly qualities are important for developing explosives to be used in advanced weapons systems.[1] While in aeronautics,[4, 12] propellants with enhanced properties are essential for replacing hazardous compounds such as hydrazine.[1, 3, 4, 8, 10, 12] While 'green' HEDMs have yet to be used in real-world systems, incentives for exchanging conventional energetic materials for 'green' HEDMs are eliminating potential health hazards,[10] reducing environmental pollution,[10, 13] and decreasing contamination.[12]
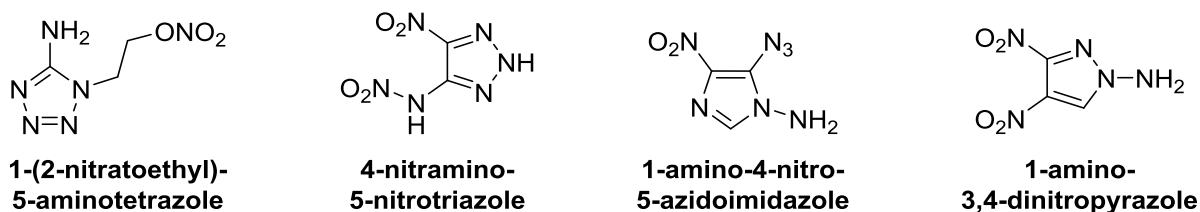
Scheme 2. Examples of novel, 'green' HEDMs.

Therefore, understanding how and why detonation occurs in conventional energetic materials is crucial for determining the mechanism in novel, 'green' HEDMs. Progress has been made to develop 'green' HEDMs that could replace conventional energetic materials in real-world systems; however, a systematic means of predicting and understanding energetic properties is necessary in order to guide their syntheses.[1, 3, 4, 8, 10, 13] Since detonation is nearly an instantaneous process, experimental kinetic studies to determine a mechanism are difficult to perform.[14] Thus, computational modeling with density functional theory (DFT) and molecular dynamics (MD)[1, 15,

[16] is a promising means to propose explosive decomposition initiation and detonation mechanisms from measures of bond strength and intermolecular interactions to understand energetic properties and guide syntheses. Characterizing explosive decomposition and detonation can help interpret the degree to which energetic properties, energy release, and chemical composition impact the environment, in order to streamline the design of novel, 'green' HEDMs.[1, 3, 4, 8, 10, 12, 14]

Chemistry of Energetic Materials

Energetic materials are compounds that release substantial amounts of energy and pressure upon detonation,[7, 8, 11] and can be categorized as propellants, primary explosives and secondary explosives. Propellants deflagrate, which is a self-propagating process where the compound burns rapidly to produce enough gas for propulsion.[7, 11] Explosives undergo detonation, defined as the propagation of highly energetic reactions under the influence of high pressure from a shockwave through the energetic material.[6, 17] Primary and secondary explosives differ in sensitivity, where primary explosives are highly sensitive to external stimuli (i.e., heat, impact, and friction)[5, 6, 11] while secondary explosives are initiated by the shockwave produced by the detonation of a primary explosive.[7, 11] Primary explosives used in typical formulations include lead azide ($Pb^{II}(N_3)_2$) and lead styphnate ($C_6HN_3O_8 \cdot Pb^{II}$), while one less frequently used is mercury fulminate ($Hg^{II}(CNO)_2$).[6, 7] The more powerful secondary explosives include TNT, PETN, RDX, HMX, HpNC, ONC, CL-20, HNS and TATB.

HEDMs with high nitrogen content are desirable in order to enhance energetic properties and improve environmental compatibility.[3, 5, 6, 10] HEDMs contain large amounts of nitrogen and oxygen, along with other oxidizable elements such as carbon and hydrogen.[6, 7] Various energetic properties are used to further classify HEDMs, including oxygen balance (Ω), heat of formation

(ΔH_F), heat of explosion (Q), detonation velocity (D), detonation pressure (P), and measures of sensitivity.[7] Oxygen balance (Ω) is the amount of oxygen released in the gaseous products of detonation, determined by comparing the proportion of oxygen in the HEDM to the oxygen required for complete oxidation of the fuel elements (i.e., carbon and hydrogen).[6, 7, 18] For energetic materials containing the general formula $C_aH_bN_cO_d$ and molecular weight (MW), the oxygen balance can be calculated by Equation 1.[6, 7, 18]

$$\Omega = \frac{\left[d - (2a) - \left(\frac{b}{2}\right)\right] \times 1599.940}{MW} \tag{1}$$

A positive oxygen balance indicates a high proportion of oxygen so that complete oxidation occurs; however, an insufficient amount of oxygen, leading to incomplete oxidation, is designated by a negative oxygen balance.[6, 7, 18] A large and negative oxygen balance means carbon dioxide will not form due to an oxygen deficiency; thus, toxic gases are released,[6, 7] such as carbon monoxide and nitrogen dioxide. For example, PETN ($C_5H_8N_4O_{12}$, MW = 316 g/mol) has an oxygen balance of -10.13%. For HEDMs with an oxygen balance greater than -40.0%, the detonation products can be proposed based on the Kistiakowsky-Wilson rules: (1) carbon atoms are converted to CO, (2) hydrogen is oxidized to water if oxygen remains, (3) CO is oxidized to CO_2 if oxygen still remains, and (4) all nitrogen atoms are converted to N_2.[7] For example, the final detonation products of PETN based on the Kistiakowsky-Wilson rules are (Equation 2):

$$C_5H_8N_4O_{12} \rightarrow 2CO + 4H_2O + 3CO_2 + 2N_2 \tag{2}$$

However, if HEDMs have an oxygen balance less than -40.0% like TNT ($C_7H_5N_3O_6$, MW = 227 g/mol, Ω = -74.01%), detonation products are proposed by the Springall-Roberts rules: (1) carbon atoms are converted to CO, (2) hydrogen is oxidized to water if oxygen remains, (3) CO is oxidized to CO_2 if oxygen still remains, (4) all nitrogen atoms are converted to N_2, (5) one third of the original CO is converted to C and CO_2, and (6) one sixth of the original CO is converted to C and

H_2O.[6,7] Therefore, the final detonation products of TNT based on the Springall-Roberts rules are (Equation 3):

$$C_7H_5N_3O_6 \rightarrow 3CO + \frac{3}{2}N_2 + 3C + \frac{3}{2}H_2 + CO_2 + H_2O \tag{3}$$
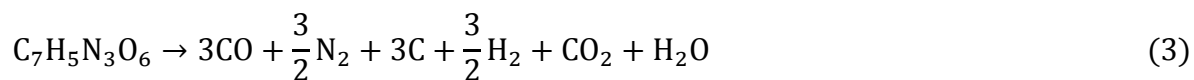
The final products of detonation are necessary in order to calculate heats of formation (ΔH_F), the heat evolved during complete oxidation; however, when incomplete oxidation occurs, the energy released is termed the heat of explosion (Q).[6,7] Energetic materials should have negative heats of formation (ΔH_F), since that indicates an exothermic reaction and the release of large amounts of heat.[7] For example, PETN and TNT have negative ΔH_F (-531 kJ/mol and -62 kJ/mol, respectively) and positive Q values (+1838 kJ/mol and +929 kJ/mol, respectively), but the larger negative ΔH_F and positive Q of PETN indicates more heat liberation and a more powerful energetic material when compared to TNT.[7] The explosive power of an energetic material is the product of the heat of explosion (Q) and the volume of gas released upon detonation (V), determined from the detonation products (Equation 4).[6,7]

$$\text{Explosive Power} = Q \times V \tag{4}$$

Comparing the explosive power of an HEDM ($Q \times V$) to that of a standard energetic material ($Q_{standard} \times V_{standard}$) results in the power index (Equation 5).[6,7]

$$\text{Power Index} = \frac{Q \times V}{Q_{standard} \times V_{standard}} \tag{5}$$

Other measures of energetic power include detonation velocity (D, the speed at which the shockwave propagates through an energetic column) and detonation pressure (P, the pressure of the shockwave). Impact sensitivity (I.S.), friction sensitivity (F.S.), and electrical spark sensitivity (E.S.) describe the stability of energetic materials when exposed to external stimuli. Specifically

for I.S., the values for conventional HEDMs range from ~10 cm (i.e., sensitive) to ~500 cm (i.e., stable).

Even though detonation products can be proposed based on the structure, many of the mechanisms remain unknown due to the rapid nature of the reactions. Thus, computational tools are necessary to understand this phenomena by identifying activated bonds that break first to initiate explosive decomposition, termed trigger bonds,[16] which are categorized based on explosophores (i.e., nitro ($-NO_2$) and azide ($-N_3$) functional groups[5]).[1, 14, 15] Assigning trigger bonds with an efficient computational method can be used to screen energetic potential, understand energetic properties, and guide HEDM synthesis with less waste and improved 'green' qualities for applications in advanced weapons systems, aeronautics, asteroid mining and sample collection.[1-4, 7, 19] Furthermore, understanding the influence of intramolecular and intermolecular interactions on energetic material sensitivity can help rationalize the complexity behind the energetic reactions in order to guide the synthesis of novel HEDMs and screen their energetic potential. In this study, trigger bonds of conventional and novel HEDMs are characterized using computational methods to determine how intramolecular and intermolecular interactions might influence initiation of energetic reactions.

Computational Methods

Density Functional Theory Overview, Functionals, Basis Sets

In this dissertation, DFT is used as the basis for all theoretical calculations to show how intramolecular and intermolecular interactions influence the sensitivity of energetic materials. DFT is a quantum mechanical computational method that determines electronic and molecular

properties from the electron density (ρ) of a system.[20] The Schrödinger equation (Equation 6) is a quantum mechanical equation that describes the measurable properties of subatomic particles.

$$\hat{H}\psi = E\psi \tag{6}$$

In the Schrödinger equation, $\hat{H}$ represents the electronic Hamiltonian operator which acts upon a wavefunction, ψ, and returns the original function, termed the eigenfunction, multiplied by the electronic energy of the system, E. $\hat{H}$ is comprised of the electronic kinetic energy, nucleic kinetic energy, and potential energy (i.e., attraction between electrons and nuclei, electron-electron repulsion, and proton repulsion in the nucleus) (Equation 7).[20]

$$\hat{H} = -\sum_i \frac{1}{2}\nabla_i^2 - \sum_k \frac{1}{2m_k}\nabla_k^2 - \sum_i\sum_k \frac{Z_k}{r_{ik}} + \sum_{i>j} \frac{1}{r_{ij}} + \sum_{k>l} \frac{Z_k Z_l}{r_{kl}} \tag{7}$$

The nucleic kinetic energy takes into account the mass of the nucleus (m_k). The potential energy of the electron-nuclei attraction is defined as the interaction at position r_{ik} between the electron (i) and nucleus (k) with charge Z_k. The potential energy of the electron-electron repulsion is the interaction at position r_{ij} between the electrons (i and j). The potential energy of the proton repulsion in the nucleus is expressed as the interaction at position r_{kl} between the proton (l) with charge Z_l and the nucleus (k) with charge Z_k.[20] The Born-Oppenheimer approximation reduces the number of terms in the Hamiltonian by assuming the heavier and slower nuclei do not contribute to the kinetic energy of the system as the electrons do.[20] Thus, the kinetic energy of the nuclei of the system, which is taken into account in Equation 7, can be ignored (Equation 8).

$$\hat{H}_{electronic} = -\sum_i \frac{1}{2}\nabla_i^2 - \sum_i\sum_k \frac{Z_k}{r_{ik}} + \sum_{i>j} \frac{1}{r_{ij}} + \sum_{k>l} \frac{Z_k Z_l}{r_{kl}} \tag{8}$$

It is not possible to solve the Schrödinger equation for many-electron systems; thus, the Hartree-Fock (HF) method is used in order to estimate the energy of the system.[21] The HF method uses the variation method to get an approximate solution to a many-electron Hamiltonian using a

single Slater determinant as the wave function. The electron wavefunction describing the set of electrons is described as (Equation 9),

$$\psi(r_1, S_{z1}, r_2, S_{z2}, \dots, r_i, S_{zi}, \dots, r_I, S_{zI}) \tag{9}$$

where r_i is the position of electron i, S_{zi} is the spin of electron number i in direction z, and I is the total number of electrons. The HF method approximates ψ using single-electron functions, termed molecular orbitals (MOs), from a linear combination of basis functions which are often atom-centered Gaussian functions[21] (Equation 10),

$$\psi_j = \sum_{i=1}^{N} c_{si}\chi_s \tag{10}$$

where the group of N basis functions, χ_s, is the basis set, and the coefficients, c_{si}, are the MO expansion coefficients for electron i in orbital j.[22] The Hamiltonian operator changes when the electrons are treated individually (Equation 11),

$$\hat{H} = \sum_{i=1}^{I} h_i \text{ , and } h_i = -\frac{1}{2}\Delta_i^2 - \sum_{k=1}^{I} \frac{Z_k}{r_{ik}} + \mathrm{U}_i\{j\} \text{ , and } \mathrm{U}_i\{j\} = \sum_{j \neq i} \int \frac{\rho_j}{r_{ij}} dr \tag{11}$$

where I is the total number of electrons and h_i is the one electron Hamiltonian. $\mathrm{U}_i\{j\}$ is the interaction of electron i with all the electrons in orbital j. Furthermore, the wavefunction can be written as a product of single-electron wavefunctions or a Hartree-product wavefunction (Equation 12).

$$\psi_{HP} = \psi_1\psi_2\psi_3 \dots \psi_I \tag{12}$$

The HF method represents the antisymmetric wavefunction and can be written as a Slater determinant, the sum of the $I!$ Hartree-products.

The main problem with the HF method is that electron correlation is not fully considered; thus, the error can be large and dispersion interactions cannot be modeled. Therefore, post-HF

methods or multireference methods have been developed to improve upon the HF method, including configuration interaction (CI),[23] coupled cluster (CC),[24] and Møller-Plesset perturbation theory[25] (i.e., MP2, MP3, etc.). Post-HF methods include more of the electron correlation; however, these calculations are computationally expensive. As such, DFT is advantageous because it has comparable computational cost to HF and can be as accurate as MP2 calculations.[26] While HF is based on the molecular wavefunction, DFT is based on the electron probability density function.[27] Hohenberg and Kohn determined that molecular properties can be described by the ground state electron density. The total energy is defined as (Equation 13),

$$E_0 = E_v[\rho_0] = T_0[p] + V_{Ne}[\rho_0] + V_{ee}[\rho_0] \tag{13}$$

where E_0 is a function of the ground state energy but dependent on the external potential, v.[20] $T_0[p]$ is the kinetic energy, $V_{Ne}[\rho_0]$ is the electron density-nuclei attraction, and $V_{ee}[\rho_0]$ is the electron repulsion.[20]

The Kohn and Sham (KS) method approximates electron density in terms of MOs.[28] The KS method uses a reference system (s) of n non-interacting electrons with the same density as the real system (0) (Equation 14), and the electron-nuclei attraction is determined from the nucleic external potential, $v_s(r_i)$.

$$\rho_s(r) = \rho_0(r) \tag{14}$$

Therefore, the Hamiltonian for the reference system would be (Equation 15)

$$\hat{H}_s = \sum_{i=1}^{n} \left[-\frac{1}{2} \nabla_i^2 + v_s(r_i) \right] \equiv \sum_{i=1}^{n} \hat{h}_i^{KS} \text{ and } \hat{h}_i^{KS} \equiv -\frac{1}{2} \nabla_i^2 + v_s(r) \tag{15}$$

where $\hat{h}_i^{KS}$ is the KS one electron operator and $v_s(r)$ is composed of the exchange-correlation potential.[20] Thus, the KS ground-state electronic energy of a system can be written as (Equation 16)

$$E_0 = \int \rho(r)v(r)dr + \frac{1}{2}\int \frac{\rho(r_1)(r_2)}{r_{12}}dr_1 dr_2 + E_{xc}[\rho] \tag{16}$$

where $E_{xc}[\rho]$ is the exchange-correlation energy functional, a term previously ignored in the HF method. $E_{xc}[\rho]$ includes electron-nuclei attraction, the kinetic energy of non-interacting electrons, and the electron repulsion correction.[29] $E_{xc}[\rho]$ is difficult to determine, but only accounts for a small portion of the total energy. The electron density is calculated by squaring the sum of the KS orbitals (ψ_i^{KS}) (Equation 17).

$$\rho = \rho_s = \sum_i |\psi_i^{KS}|^2 \tag{17}$$

Since the exchange-correlation energies are unknown, accurate approximations are necessary to estimate the total energy of the system. The exchange-correlation energy can be approximated by DFT functionals, including Local Density Approximation (LDA) or Generalized Gradient Approximation (GGA).

LDAs are functionals that do not uniformly distribute the electron density (Equation 18),

$$E_{xc}^{LDA}[\rho] = \int \rho(r)\varepsilon_{xc}(\rho)dr \tag{18}$$

where ε_{xc} is the exchange (ε_x) and correlation (ε_c) energy for each electron (Equation 19).

$$\varepsilon_{xc}[\rho] = \varepsilon_x(\rho) + \varepsilon_c(\rho) = -\frac{3}{4}\left(\frac{3}{\pi}\right)^{\frac{1}{3}}(\rho(r))^{\frac{1}{3}} + \varepsilon_c^{VWN}(\rho) \tag{19}$$

The expression for the correlation energy (ε_c^{VWN}) is a function developed by Vosko, Wilk and Nusair (VWN).[30] The LDA functional can be improved by using the Local-Spin-Density Approximation (LSDA). LDA treats paired electrons with the same KS orbitals while LSDA allows electrons with opposite spins to occupy different orbitals. Thus, LSDA is a better description for open-shell molecules.

GGAs functionals improve both LDA and LSDA by including the position of electron density. The exchange-correlation energy (E_{xc}^{GGA}) adds the electron densities of both α- (ρ^α) and β-spin electrons (ρ^β) (Equation 20).

$$E_{xc}^{GGA}[\rho^\alpha, \rho^\beta] = \int f\big(\rho^\alpha(r), \rho^\beta(r), \nabla\rho^\alpha(r), \nabla\rho^\beta(r)\big)dr \tag{20}$$

Similarly to LDA and LSDA, the exchange and correlation energies are calculated separately and then added together. Common GGA functionals include PBE,[31] developed by Perdew, Burke and Ernzerhof, and PW91,[32] developed by Perdew, Chevary, Vosko, Jackson, Pederson, Singh and Fiolhais, both containing exchange-correlation without empirical parameters. Another common GGA functional, BLYP,[33, 34] has an exchange functional developed by Becke (B) and a correlation functional developed by Lee, Yang and Parr (LYP). Meta-GGA functionals include the second derivatives of electron density instead of simply the first derivatives as in GGA functionals.[22] Hybrid meta-GGA functionals can more accurately calculate the exchange-correlation energy, but are more computationally expensive than GGA functionals.[22] Hybrid meta-GGA functionals are a mixture of DFT and HF exchange functionals with DFT correlation functionals (Equation 21),

$$E_{xc}^{hybrid} = c^{HF}E_x^{HF} + c^{DFT}E_{xc}^{DFT} \tag{21}$$

where c^{HF} and c^{DFT} are constants. For example, Zhao and Trular's hybrid meta-GGA functional M06-2X is reliable in describing thermochemistry, kinetics, and noncovalent interactions in nonmetal systems.[35] In this study, we use M06-2X because it has been shown to have the lowest mean unsigned errors (i.e., absolute deviations of calculated values relative to a reference)[16, 35, 36] and most efficiently describe noncovalent interactions compared to other functionals.[35, 37]

In HF and DFT, the MOs that contribute to the wavefunction or density are a linear combination of basis functions, χ_s, which forms the basis set (see Equation 10). The two types of basis functions are Slater-Type Orbitals (STOs) and Gaussian-Type Orbitals (GTOs). An

advantage of STOs over GTOs is that STOs are similar to the hydrogenic atomic orbitals (AOs); however, the two-electron integrals of STOs are computationally expensive. To lower computational cost, Boys[38] proposed using GTOs since they are two-center two-electron integrals. Multiple GTOs are necessary in order to represent one STO because GTOs do not accurately represent the cusp at the nucleus.[39] However, using multiple GTOs are used to correct the problem while still maintaining faster calculations than STOs.

Larger basis sets more accurately model orbitals by allowing electrons to have positional freedom.[21] Gaussian functions are termed primitives while basis functions are called contracted functions. A contracted basis function contains only one Gaussian function for both core and valence electrons and are termed minimal basis sets. For example, the minimal basis set STO-3G uses three primitive Gaussian functions (3G) per basis function to resemble an STO.[22] Basis sets with more than one Gaussian function for valence orbitals are termed double-, triple-, quadruple-zeta basis sets.[39] Split-valence basis sets developed by Pople[40] describe the number of primitive Gaussian functions on the core electrons as well as the basis functions for each valence orbital in the form a-bcG. The a is the number of primitive Gaussian functions for core orbitals and b and c denote the number of functions the valence orbitals are split into and the number of primitive Gaussian functions for each. Polarization functions add GTOs to the angular momentum and allow AOs to distort as the charges change,[41] while diffuse functions let the AOs spread out in space. Correlation-consistent polarized (cc-p) basis sets include electron correlation, and the prefix *aug* is used to add diffuse and polarization functions.[42] The TZVP basis set is a split valence triple zeta basis set with added polarization functions.[43] Even with a slightly higher computational cost, an advantage of using TZVP is that the valence electrons are uncontracted[44] whereas the Pople basis sets have contracted valence electrons.

Periodic Boundary Conditions, Plane Wave Basis Sets, Pseudopotentials

In order to accurately represent condensed-phase models, periodic boundary conditions are used. The model is assumed to be a unit cell of an ideal crystal, or a box (**Figure 1**), which can be duplicated in all directions.[22, 39] In periodic boundary conditions, the model is quasi-periodic (i.e., an atom or molecule leaves the central box on the right side and reappears on the left side), with periodicity equal to the dimensions of the box.[39] Since electrostatic interactions extend beyond the boundary of the box, cutoff distances are used to evaluate intermolecular interactions.[22, 39] A key advantage of periodic boundary conditions is that structural anomalies, such as segregation of atoms with partial charges of like sign, are avoided.[22] Furthermore, *k-points* are used to describe the dimensions of the first Brillouin zone, or the box (**Figure 1**), and are determined based on the size of the unit cell and the periodicity of the system.[45]
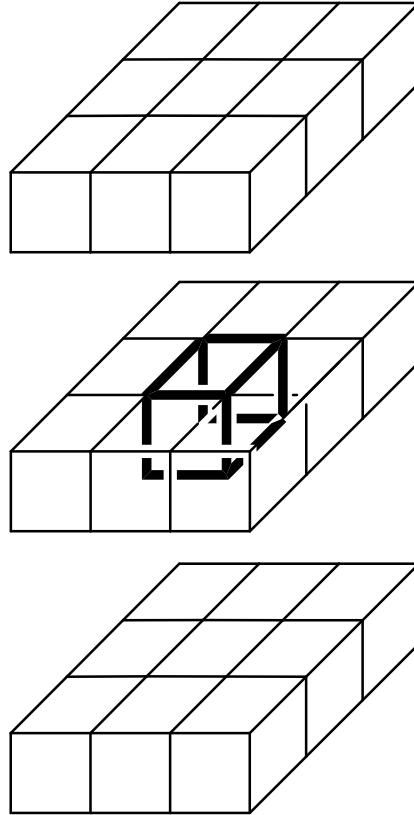
Figure 1. Unit cell (in bold) surrounded by 26 periodic images generated by periodic boundary conditions.

Rather than using basis functions to model AOs, a linear combination can describe the orbitals for the entire system.[39] Plane waves as basis sets are used for periodic infinite (extended) systems, which are represented using periodic boundary conditions,[22, 27] since these are exact solutions for free electrons.[39] Unit cells of complex systems have inconsistent densities, where the basis functions can be localized (Gaussian) or delocalized (plane wave). Once the KS method is subjected to periodic boundary conditions, the electron density from Equation 17 is modified (Equation 22),

$$\rho = \sum_{nk} \left| \psi_{nk}^{KS} \right|^2 \tag{22}$$

where n is the band index and k is described as a frequency factor (i.e. high values mean rapid oscillation) and related to the crystal momentum.[27, 39] For finite systems, the MOs combine into bands described by orbitals expanded in a plane wave basis set[39] (Equation 23),

$$\psi_{nk} = \sum_{i=1}^{N} c_{ki} \frac{\chi_k(r)}{\sqrt{V_{uc}}} \text{ , and } \chi_k(r) = e^{ik \cdot r} \tag{23}$$

where V_{uc} is the volume of the unit cell, c_{ik} are the MO expansion coefficients, and a group of N basis functions produces the basis set, χ_k.

In order to accurately describe the wavefunction, multiple plane waves (i.e., large N) are required. Plane wave basis functions are best for describing delocalized, slowly changing electron densities. The core electrons are localized around the nuclei while the valence orbitals are delocalized. Since it is nearly impossible to describe the nucleus-electron interaction in a plane wave basis set, pseudopotentials are used with plane wave basis sets.[39] Pseudopotentials smear the nuclear charge, model the effect of the core electrons, and are characterized by a core radius that is dependent on the angular momentum of the valence orbitals. Furthermore, a hard pseudopotential requires more plane wave basis functions for describing the region beyond the core radius while soft pseudopotentials require less plane wave basis functions. A disadvantage to plane wave basis sets are that multiple rapidly oscillating functions are required to describe the unit cell densities and are thus larger than Gaussian basis sets; however, the integrals are relatively simple to solve, making this approach applicable in solid-state calculations.[22, 27, 39]

Software Packages

In this dissertation, Gaussian 09[46] and Quantum Espresso[47] software packages have been used in order to study the energetic properties and mechanisms of conventional energetic materials

and novel HEDMs. DFT calculations were employed using Gaussian 09 and the hybrid functional M06-2X[35] with a triple-ζ basis set (TZVP)[48] in order to understand electronic and molecular properties. Several method and basis set combinations were studied in order to determine the best correlation with available experimental data[16, 49] before settling on this particular combination. The structures are optimized and characterized as minima on the potential energy surface through vibrational analysis. The strength of bonds in the energetic materials were determined through the Wiberg bond index, calculated using Natural Bond Orbital (NBO) version 3.1.[50, 51] The gas-phase calculations are used to understand the influence of intramolecular interactions on the sensitivity of energetic materials. Quantum Espresso uses a pseudopotential approach, which reduces computational time by exploring the valence electrons rather than the full electron system. The Perdew-Burke-Ernzerhof (PBE)[31] pseudopotentials are used for the Quantum Espresso calculations due to good correlation with experimental data. Structures are optimized until the energy and forces are well converged, and then MD is used to determine how the optimized structures change over time with increasing pressure. The condensed-phase calculations are used to understand how intermolecular interactions within energetic materials change over time with increasing pressure. In this dissertation, the goal is to rationalize the varying sensitivities observed in different classes of energetic materials using gas-phase and condensed-phase calculations by characterizing the intramolecular and intermolecular interactions of the activated bonds, termed trigger bonds, within each of the molecules.

CHAPTER 2

TRIGGER BOND ANALYSIS OF NITROAROMATIC ENERGETIC MATERIALS USING

WIBERG BOND INDICES

Introduction

High energy density materials (HEDMs) with enhanced performance, reduced sensitivity and controlled energy release are important for the development of advanced weapons systems.[1, 7, 19] In aeronautics,[4] propellants with exceptional energetic properties are essential to replace hazardous materials, such as hydrazine, to reduce environmental contamination.[1-4] How and why explosive decomposition occurs in conventional energetic molecules is critical for the design of novel HEDMs. Since explosive decomposition is practically instantaneous, mechanisms of highly energetic reactions present a significant challenge to experimental analysis.[14] Thus, much effort to understand decomposition has relied upon information from molecular dynamics and density functional theory (DFT) to predict performance and sensitivity from measures of bond strength and mechanisms.[1, 14, 15]

Explosophores[5] such as nitro ($-NO_2$)[52-56] and azide ($-N_3$)[11] functional groups are generally needed to sensitize energetic materials. $X-NO_2$ (X=N,C,O) bonds substituted on energetic materials have been proposed to form 'trigger bonds', activated (i.e., more readily cleaved) bonds that break to initiate an explosive reaction.[16] Initiation steps proposed based on mass

spectrometry[57-61] and DFT[62-66] for common secondary explosives (1,3,5-trinitro-1,3,5-triazacyclohexane (RDX), 1,3,5,7-tetranitro-1,3,5,7-tetrazacyclooctane (HMX), 2,4,6-trinitrotoluene (TNT), trinitrobenzene (TNB), and pentaerythritol tetranitrate (PETN)) generally include homolytic bond cleavage, interatomic rearrangements, molecular eliminations, and/or ring fission. Studies of TNT[61, 66-69] suggest that C-NO$_2$ homolytic cleavage is the most favorable initiation step. Other pathways proposed for nitroaromatic energetic materials include nitronic acid formation by hydrogen transfer in nitrophenols[70-72] and cyclization by heating nitroanilines to form furazan or furoxan derivatives[67, 73] (**Figure 2**). However, the hydrogen transfer pathway is endothermic (ΔE+ZPE (DFT(M06-2X/TZVP) = +29 kcal/mol) and lacks a clear pathway to explosive decomposition because the HONO group is doubly bonded to the aromatic ring rather than cleaved (**Figure 2a**). In contrast, RDX, HMX, and PETN eliminate HONO by extracting a hydrogen from a neighboring –CH$_2$– group (**Figure 2b**).[62-65] For the cyclization pathway, Green and Rowe[74, 75] proposed the oxidation of *o*-dinitroanilines to dinitroazobenzenes or the furazan oxides based on synthesis under neutral and alkaline conditions, respectively. However, decomposition either of these two pathways would require the initial loss of either H$_2$ or H$_2$O which are necessarily multi-step (**Figure 2c**)[73] and seem unlikely to result in a chain reaction. In addition, a DFT study on 1,3,5-triamino-2,4,6-trinitrobenzene (TATB) did not consider cyclization as the primary method of initiation due to high activation barriers.[76]
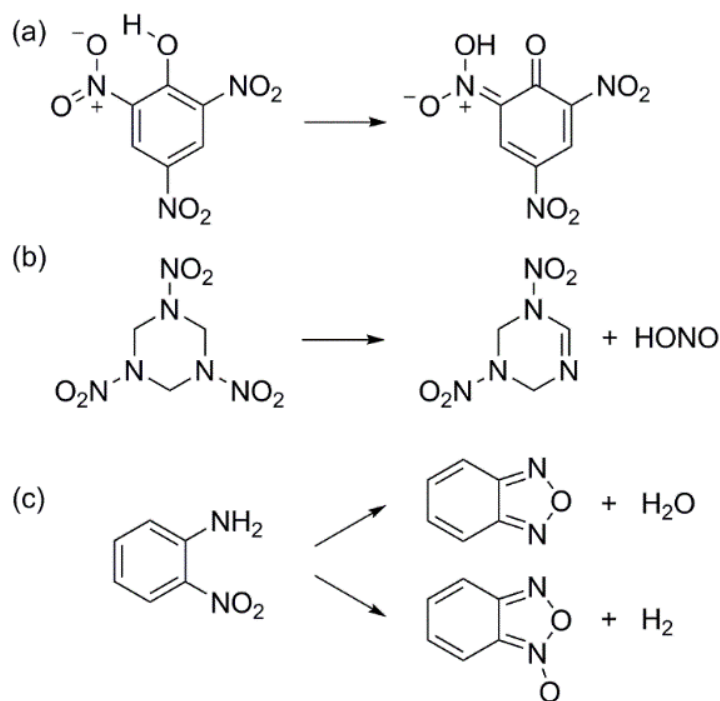
Figure 2. Example of (a) HONO molecular rearrangement, (b) HONO elimination in RDX, and (c) cyclization in nitroaromatics.

Although many factors unique to the solid state can influence the sensitivity of energetic materials,[1, 7, 19, 67] gas-phase calculations can contribute to understanding how intramolecular interactions influence sensitivity. Theoretical measures of bond strength include the Atoms-In-Molecules (AIM) method,[77, 78] unimolecular decomposition activation barriers,[62, 63] bond dissociation energies (BDEs),[79] and Mulliken population analysis.[70, 72, 80] Our group has recently examined the use of the Wiberg bond index (WBI) analysis as an efficient method for assigning trigger bonds. WBIs are determined as the sum of the squares of the off-diagonal elements of the density matrix (Equation 24):[81]

$$\text{WBI}_{AB} = \sum_{p \in A} \sum_{q \in B} \left(D_{pq} \right)^2 \tag{24}$$

WBIs are similar in magnitude to the bond order expected from valence bond theory[82] in contrast to the Mulliken population, which is well-known to be basis set dependent.[81] WBIs on an optimized closed-shell molecular structure have a potential advantage over BDEs which require multiple calculations on open-shell molecular fragments. Interpreting the factors that activate trigger bonds in novel HEDMs through WBI analysis can guide determination of decomposition initiation and may allow prediction of energetic properties (i.e., impact sensitivity, electrical spark sensitivity, etc.).[16]

The strength of possible trigger bonds in HEDMs will be affected by steric effects, electron withdrawing groups, and ring strain.[16] Activated bonds are expected to be longer and have lower electron density relative to reference molecules with the same bond type, hybridization and explosophore. A relative scale for the activation of each potential trigger bond can be determined by comparing the difference of the WBI for specific bond types in the HEDMs and the reference molecules (%ΔWBI) (Equation 25).[16]

$$\%\Delta WBI_{AB} = \frac{WBI_{AB}(\text{HEDM}) - WBI_{AB}(\text{reference})}{WBI_{AB}(\text{reference})} \times 100 \tag{25}$$
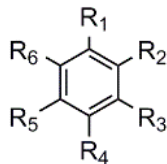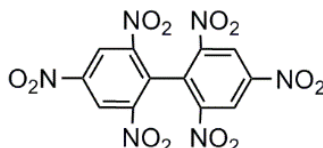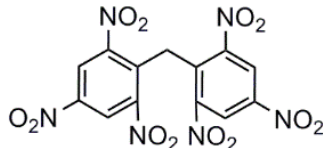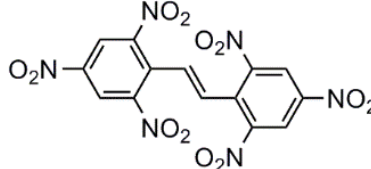
The trigger bond for a molecule is assigned based on the most negative %ΔWBIs. For example, o-C-NO$_2$ and p-C-NO$_2$ bonds in TNT were compared to the C(sp^2)-NO$_2$ bond in reference molecule nitrobenzene (NB) for %ΔWBIs of -1.11% and -0.33%, respectively (**Figure 3**).[16] The trigger bond is assigned as the more activated o-C-NO$_2$ bond,[16] in agreement with the results of previous computational and experimental studies.[61, 67-69] Previous studies on energetic materials using WBIs[83-91] did not apply reference molecules to determine a relative scale for bond activation which could lead to inaccurate trigger bond assignment. For PETN,[60, 65, 92-94] DFT studies[65, 92] found O-NO$_2$ homolysis to be more energetically favorable than C-ONO$_2$ homolytic cleavage and HONO elimination, consistent with experimental thermal decomposition studies of nitrate and nitrite

esters.[93, 94] Direct comparison of absolute WBIs would suggest that $C-ONO_2$ is more activated than $O-NO_2$ (0.892 and 0.901, respectively); however, referencing to bonds in methyl nitrate correctly assigns $O-NO_2$ rather than $C-ONO_2$ as the trigger bond (%ΔWBIs = -2.92% and -1.33%, respectively).[16] In addition, our %ΔWBIs were able to distinguish between the trigger bond strength in conformations of HMX which could help explain different sensitivities observed among its polymorphs.[16] Thus, %ΔWBIs are a promising method for interpreting experimental impact sensitivity for a set of conventional and novel HEDMs.[16] In this study, DFT %ΔWBIs were calculated for a set of 63 conventional nitroaromatic energetic molecules (**Table 1**) and compared to experimental energetic properties to determine how intramolecular steric and substituent effects can influence the trigger bond.
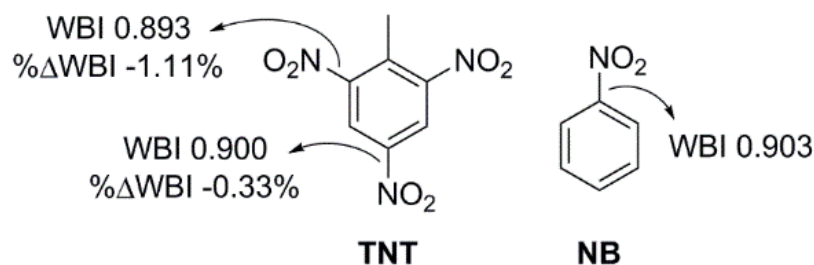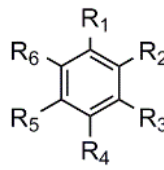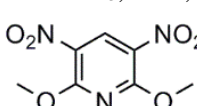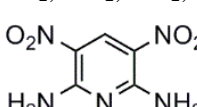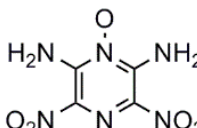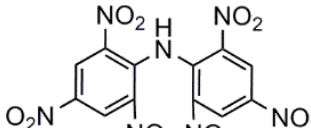
Figure 3. Example of WBI analysis of TNT and reference molecule NB.
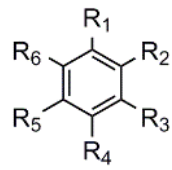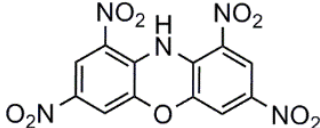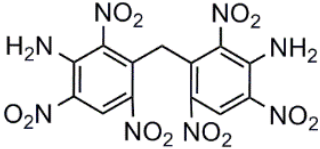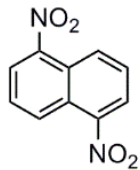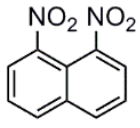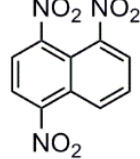
Table 1. The 63 conventional nitroaromatic energetic materials included in this study.

Compound	Chemical Name		
			R_1, R_2, R_3, R_4, R_5, R_6

Nitrobenzenes		
DNB	1,3-dinitrobenzene	NO_2, H, NO_2, H, H, H
TNB	1,3,5-trinitrobenzene	NO_2, H, NO_2, H, NO_2, H
TETNB	1,2,3,5-tetranitrobenzene	NO_2, NO_2, NO_2, H, NO_2, H
PNB	Pentanitrobenzene	NO_2, NO_2, NO_2, NO_2, NO_2, H
HNB	Hexanitrobenzene	NO_2, NO_2, NO_2, NO_2, NO_2, NO_2,
HNBP	2,2',4,4',6,6'-hexanitrobiphenyl	
HNDPM	2,2',4,4',6,6'-hexanitrodiphenylmethane	
HNS	2,2',4,4',6,6'-hexanitrostilbene	

Nitrobenzyls		
DNT	2,6-dinitrotoluene	CH_3, NO_2, H, H, H, NO_2
TNT	2,4,6-trinitrotoluene	CH_3, NO_2, H, NO_2, H, NO_2
o-TETNT	2,3,4,5-tetranitrotoluene	CH_3, NO_2, NO_2, NO_2, NO_2, H
m-TETNT	2,3,4,6-tetranitrotoluene	CH_3, NO_2, NO_2, NO_2, H, NO_2
p-TETNT	2,3,5,6-tetranitrotoluene	CH_3, NO_2, NO_2, H, NO_2, NO_2
PNT	Pentanitrotoluene	CH_3, NO_2, NO_2, NO_2, NO_2, NO_2
DMTNB	1,3-dimethyl-2,4,6-trinitrobenzene	CH_3, NO_2, CH_3 NO_2, H NO_2
TMTNB	1,3,5-trimethyl-2,4,6-trinitrobenzene	CH_3, NO_2, CH_3, NO_2, CH_3, NO_2
ATNT	3-amino-2,4,6-trinitrotoluene	CH_3, NO_2, NH_2, NO_2, H NO_2
o-ATETNT	2-aminotetranitrotoluene	CH_3, NH_2, NO_2, NO_2, NO_2, NO_2
m-ATETNT	3-aminotetranitrotoluene	CH_3, NO_2, NH_2, NO_2, NO_2, NO_2
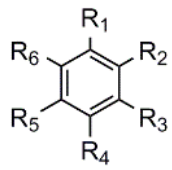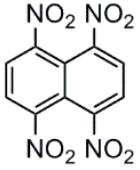
Table 1 (continued)

Compound	Chemical Name	R₁, R₂, R₃, R₄, R₅, R₆
p-ATETNT	4-aminotetranitrotoluene	CH_3, NO_2, NO_2, NH_2, NO_2, NO_2
ClMTNB	Chloromethyl-2,4,6-trinitrobenzene	CH_2Cl, NO_2, H, NO_2, H, NO_2
TNBMeOH	2,4,6-trinitrobenzenemethanol	CH_2OH, NO_2, H, NO_2, H, NO_2
TNBEtOH	2,4,6-trinitrobenzeneethanol	CH_2CH_2OH, NO_2, H, NO_2, H, NO_2

Nitroanisoles

Compound	Chemical Name	R₁, R₂, R₃, R₄, R₅, R₆
DNAN	2,4-dinitroanisole	OCH_3, NO_2, H, NO_2, H, H
TNAN	2,4,6-trinitroanisole	OCH_3, NO_2, H, NO_2, H, NO_2
ATNAN	3-amino-2,4,6-trinitroanisole	OCH_3, NO_2, NH_2, NO_2, H, NO_2
DMOTNB	1,3-dimethoxy-2,4,6-trinitrobenzene	OCH_3, NO_2, OCH_3, NO_2, H, NO_2
DClTNAN	3,5-dichloro-2,4,6-trinitroanisole	OCH_3, NO_2, Cl, NO_2, Cl, NO_2
EOTNB	Ethoxy-2,4,6-trinitrobenzene	OCH_2CH_3, NO_2, H, NO_2, H, NO_2
DMDNPy	2,6-dimethoxy-3,5-dinitropyridine	

Nitroanilines

Compound	Chemical Name	R₁, R₂, R₃, R₄, R₅, R₆
DNPH	2,4-dinitrophenylhydrazine	$NHNH_2$, NO_2, H, NO_2, H, H
TNA	2,4,6-trinitroaniline	NH_2, NO_2, H, NO_2, H, NO_2
DATB	1,3-diamino-2,4,6-trinitrobenzene	NH_2, NO_2, NH_2, NO_2, H, NO_2
TATB	1,3,5-triamino-2,4,6-trinitrobenzene	NH_2, NO_2, NH_2, NO_2, NH_2, NO_2
TETNA	2,3,4,6-tetranitroaniline	NH_2, NO_2, NO_2, NO_2, H, NO_2
PNA	Pentanitroaniline	NH_2, NO_2, NO_2, NO_2, NO_2, NO_2
DADNPy	2,6-diamino-3,5-dinitropyridine	
LLM-105	2,6-diamino-3,5-dinitropyrazine-1-oxide	
HNDPA	2,2',4,4',6,6'-hexanitrodiphenylamine (dipicryl amine)	

Table 1 (continued)

Compound	Chemical Name		R_1, R_2, R_3, R_4, R_5, R_6
TETNPO	1,3,7,9-tetranitro-10H-phenoxazine		
DAHNBP	3,3'-diamino-2,2',4,4',6,6'-hexanitrobiphenyl		

Nitrophenols

2,4-DNP	2,4-dinitrophenol	OH, NO_2, H, NO_2, H, H
2,6-DNP	2,6-dinitrophenol	OH, NO_2, H, H, H, NO_2
2,4-DNR	2,4-dinitroresorcinol	OH, NO_2, OH, NO_2, H, H
4,6-DNR	4,6-dinitroresorcinol	OH, H, OH, NO_2, H, NO_2
PA	2,4,6-trinitrophenol (picric acid)	OH, NO_2, H, NO_2, H, NO_2
TNR	2,4,6-trinitroresorcinol	OH, NO_2, OH, NO_2, H, NO_2
THTNB	1,3,5-trihydroxy-2,4,6-trinitrobenzene	OH, NO_2, OH, NO_2, OH, NO_2
MTNP	3-methyl-2,4,6-trinitrophenol	OH, NO_2, CH_3, NO_{23}, H, NO_2
TNAP	4-amino-2,3,5-trinitrophenol	OH, NO_2, NO_2, NH_2, NO_2, H
DATNP	3,5-diamino-2,4,6-trinitrophenol	OH, NO_2, NH_2, NO_2, NH_2, NO_2
HTNA	3-hydroxy-2,4,6-trinitroaniline	NH_2, NO_2, OH, NO_2, H, NO_2
DHTNA	3,5-dihydroxy-2,4,6-trinitroaniline	NH_2, NO_2, OH, NO_2, OH, NO_2

Nitronaphthalenes

1,5-DNN	1,5-dinitronaphthalene	
1,8-DNN	1,8-dinitronaphthalene	
TNN	1,4,5-trinitronaphthalene	

Table 1 (continued)

Compound	Chemical Name		R_1, R_2, R_3, R_4, R_5, R_6

| TETNN | 1,4,5,8-tetranitronaphthalene | |

Miscellaneous

ClTNB	Chloro-2,4,6-trinitrobenzene	Cl, NO_2, H, NO_2, H, NO_2
TNBN	2,4,6-trinitrobenzonitrile	CN, NO_2, H, NO_2, H, NO_2
TNBAl	2,4,6-trinitrobenzaldehyde	CHO, NO_2, H, NO_2, H, NO_2
TNBA	2,4,6-trinitrobenzoic acid	COOH, NO_2, H, NO_2, H, NO_2
ENTNB	2,4,6-trinitrophenylethanone	$COCH_3$, NO_2, H, NO_2, H, NO_2
METNBA	3-methylester-2,4,6-trinitrobenzoic acid	$COOCH_3$, NO_2, H, NO_2, H, NO_2

Computational Methods

DFT-optimized geometries of the 63 conventional nitroaromatic energetic molecules (**Table 1**) were calculated using Gaussian 09[46] and the hybrid functional M06-2X[35] with a triple-ζ basis set (TZVP).[48] Unrestricted DFT(M06-2X) BDEs for homolysis of the C-NO_2 bonds were calculated for comparison with WBIs. All structures were characterized as minima on the potential energy surface through vibrational analysis. WBIs for each potential trigger bond were calculated using Natural Bond Orbital (NBO) version 3.1.[50, 51] %ΔWBIs were determined by comparing to the C(sp^2)-NO_2 bond in reference molecule NB which contains the same bond type, hybridization and explosophore as the energetic materials. In our previous paper, diffuse functions (TZVP+) were included on all heavy atoms because that basis set gave the lowest mean unsigned errors for the bond distances in common energetic materials (RDX, HMX, TNT, TNB, PETN).[16] However,

WBIs using TZVP+ deviated significantly from the parent basis set (i.e., TZVP), indicating a basis set dependence similar to that known for Mulliken population analysis, but not previously reported for WBI analysis. Thus, the following results were obtained using TZVP which produced WBI and geometry trends comparable to calculations that included diffuse functions.

Results and Discussion

The DFT(M06-2X)/TZVP optimized structures are in good agreement with available X-ray crystallographic data[95-135] and previous DFT calculations[16, 37, 72, 84, 105, 106, 136-145] for 35 of the 63 nitroaromatic energetic molecules. The optimized structures of the 63 nitroaromatic energetic molecules are included in the appendices (**Figures A1-A7**). Generally, the DFT-optimized C-NO$_2$ bond distances are slightly longer than experimental values (**Table 2**) and intramolecular NH···ONO and OH···ONO interactions are shorter than those found in experiment.[102-107, 111, 112, 115, 130-133, 146-148] Intramolecular interactions between the nitro and amino[102-105, 130-133, 146] or hydroxyl[111, 112, 115, 148] groups force near-planar ring conformations for the aniline- and phenol-based energetic materials (**Scheme 3**). These hydrogen bonds as well as steric effects between functional groups influence the strength of the potential C-NO$_2$ trigger bonds. The nitroaromatic energetic molecules were grouped according to functional group following Kamlet and Adolph's[149] conclusion that impact sensitivity behavior of energetic materials will follow most closely with the trend of the most activated substitution. For example, ATNT and (*o*-, *m*-, *p*-)ATETNT were classified as nitrobenzyls, since the methyl group is more activating than the amino group due to steric effects. TNAP, DATNP, DHTNA and HTNA were grouped with the nitrophenols because the –OH is more activating than the –NH$_2$ due to repulsion. MTNP was also categorized with the nitrophenols since repulsion by the hydroxyl group is more influential than

steric effects by the methyl group, but was excluded from the following analysis due to its well-documented anomalous impact sensitivity.[149]
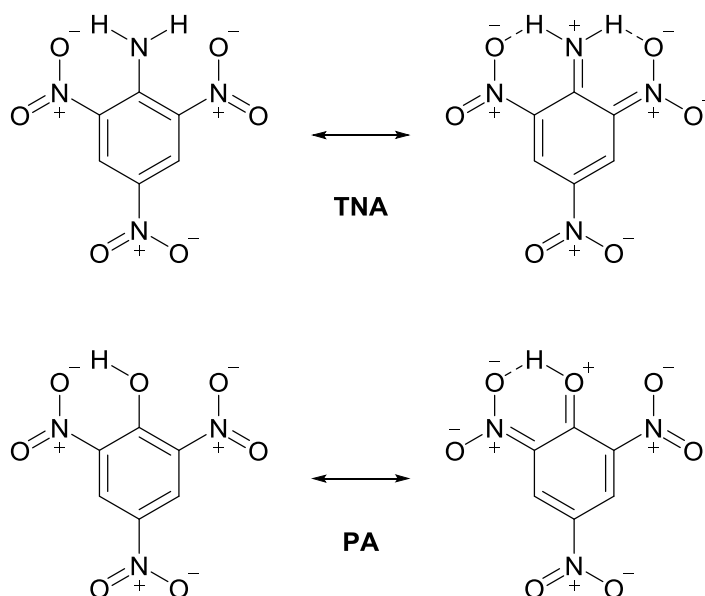
Scheme 3. C-NO$_2$ trigger bond stability from intramolecular interactions with the amino group in TNA and the hydroxyl group in PA.

Table 2. Comparison of available experimental[95-135] and DFT(M06-2X)/TZVP bond distances [Å], dihedral angles [°] and WBIs for C-NO$_2$ bonds in the nitroaromatic energetic materials with the corresponding experimental impact sensitivity (I.S.) [cm] and electrical spark sensitivity (E.S.) [J] and reference nitrobenzene (NB).[150]

HEDM	Position[a]	d_{DFT} [Å]	d_{exp} [Å]	φ_{DFT} [°]	φ_{exp} [°]	WBI	%ΔWBI [%][b]	I.S. [cm][c]
Reference								
NB	R$_1$	1.481	1.464[d]	0.0	1.7	0.902	0	100[71]
Nitrobenzenes								
DNB	R$_1$/R$_3$	1.483	1.463, 1.465	-0.1, 0.0	-10.0, 10.1	0.897	-0.55	>100[151]
TNB	R$_1$/R$_3$/R$_5$	1.485	1.474	0.0	-1.2, -4.0, 28.4	0.893	-1.00	100[149]
TETNB	R$_2$**	1.487	-	65.5	-	0.871	-3.44†	
	R$_1$*/R$_3$*	1.484	-	31.9, 32.8	-	0.889	-1.44	28[152]
	R$_5$	1.486	-	1.8	-	0.892	-1.11	

Table 2 (continued)

HEDM	Position[a]	d_{DFT} [Å]	d_{exp} [Å]	φ_{DFT} [°]	φ_{exp} [°]	WBI	%ΔWBI [%][b]	I.S. [cm][c]
PNB	R$_1$*/R$_5$*	1.485	-	-33.1, 33.0	-	0.887	-1.66	
	R$_2$**/R$_4$**	1.488	-	-60.6, 59.9	-	0.872	-3.33†	11[152]
	R$_3$**	1.487	-	-52.3	-	0.876	-2.88	
HNB	R$_1$**/R$_6$**	1.488	1.46	53.6	54.0, 54.9	0.873	-3.22	
	R$_2$**/R$_5$**	1.488	1.48	53.9	53.9, 54.0	0.872	-3.33†	11[152]
	R$_3$**/R$_4$**	1.489	1.40	53.8, 53.9	50.7, 53.1	0.872	-3.33†	
HNBP	R$_2$*/R$_{2'}$*/R$_6$*/R$_{6'}$*	1.481	1.468, 1.479, 1.472, 1.478	-30.7, ±27.9, 3.4	-26.5, 24.4, -10.0, -11.9	0.894	-0.89†	
	R$_4$/R$_{4'}$	1.483	1.474, 1.476	-3.4, 30.7	8.3, 27.5	0.895	-0.78	70[152]
HNDPM	R$_2$*	1.487	1.477	39.3	43.1	0.885	-1.88	
	R$_4$	1.482	1.491	2.7	-7.4	0.896	-0.67	
	R$_6$*	1.484	1.468	-124.3	-99.8	0.880	-2.44†	
	R$_{6'}$*	1.485	1.474	-41.5	-82.5	0.888	-1.55	39[70]
	R$_{4'}$	1.482	1.479	-0.4	4.2	0.897	-0.55	
	R$_{2'}$*	1.481	1.479	-32.3	-33.0	0.895	-0.78	
HNS	R$_2$/R$_{2'}$/R$_6$/R$_{6'}$	1.485	1.472, 1.466, 1.471	-31.3, 32.8	-13.2, 15.1, 42.0, -43.9	0.890	-1.33†	
	R$_4$/R$_{4'}$	1.484	1.468, 1.468	0.4	-22.8, 19.3	0.895	-0.78	54[152]

Nitrobenzyls

HEDM	Position[a]	d_{DFT} [Å]	d_{exp} [Å]	φ_{DFT} [°]	φ_{exp} [°]	WBI	%ΔWBI [%][b]	I.S. [cm][c]
DNT	R$_2$*/R$_6$*	1.480	1.482, 1.475	±38.2	-38.0, 53.2	0.896	-0.67	(50 J)[153]
TNT	R$_2$*/R$_6$*	1.482	1.478	±38.6	-50.7, 47.2	0.892	-1.11†	98[152]
	R$_4$	1.481	1.471	0.3	22.1	0.899	-0.33	
o-TETNT	R$_2$**	1.481	-	-56.1	-	0.881	-2.33	
	R$_3$**	1.484	-	-52.0	-	0.880	-2.44	
	R$_4$**	1.483	-	-57.6	-	0.878	-2.66†	15[152]
	R$_5$*	1.482	-	-34.5	-	0.889	-1.44	
m-TETNT	R$_2$**	1.485	-	-65.2	-	0.876	-2.88†	
	R$_3$**	1.485	-	-58.2	-	0.876	-2.88†	
	R$_4$*	1.480	-	-30.7	-	0.893	-1.00	19[152]
	R$_6$*	1.485	-	-34.0	-	0.891	-1.22	

Table 2 (continued)

HEDM	Position[a]	d_{DFT} [Å]	d_{exp} [Å]	φ_{DFT} [°]	φ_{exp} [°]	WBI	%ΔWBI [%][b]	I.S. [cm][c]
p-TETNT	R₂**/R₆**	1.482	-	-67.5, 67.7	-	0.874	-3.10†	
	R₃*/R₅*	1.483, 1.482	-	-27.1, -27.0	-	0.893	-1.00	25[152]
PNT	R₂**	1.484	-	-58.7	-	0.876	-2.88	
	R₃**	1.485	-	-51.5	-	0.877	-2.77	
	R₄**	1.484	-	-52.3	-	0.878	-2.66	18[152]
	R₅**	1.486	-	-52.0	-	0.877	-2.77	
	R₆**	1.485	-	-63.5	-	0.875	-2.99†	
DMTNB	R₂**/R₆**	1.481	1.480	90.0	75.6	0.869	-3.66†	
	R₄*	1.479	1.475	-30.3, 28.9	-34.9, -36.2	0.899	-0.33	100[154]
TMTNB	R₂**	1.479	1.479	-60.5	-68.0	0.881	-2.33	
	R₄**	1.480	1.473	-69.2	-76.0	0.877	-2.77†	110[155]
	R₆**	1.478	1.479	58.6	79.9	0.884	-2.00	
ATNT	R₂*#	1.474	-	-48.0	-	0.906	+0.44†	
	R₄#	1.465	-	-5.2	-	0.941	+4.32	174[154]
	R₆*	1.472	-	28.3	-	0.914	+1.33	
o-ATETNT	R₆**	1.484	-	-65.9	-	0.874	-3.10	
	R₅**	1.474	-	-44.3	-	0.898	-0.44	
	R₄**	1.488	-	-60.5	-	0.872	-3.33†	36[152]
	R₃*#	1.468	-	-33.0	-	0.922	+2.22	
m-ATETNT	R₆**	1.478	-	-56.3	-	0.890	-1.33	
	R₅**	1.489	-	-58.6	-	0.871	-3.44†	
	R₄*#	1.466	-	-31.1	-	0.925	+2.55	37[152]
	R₂*#	1.476	-	-53.3	-	0.898	-0.44	
p-ATETNT	R₂**/R₆**	1.485, 1.486	-	64.1, -64.3	-	0.872	-3.33†	
	R₃*#/R₅*#	1.471	-	34.1, -34.3	-	0.919	+1.88	47[152]
ClMTNB	R₂*	1.485	-	-42.6	-	0.885	-1.88†	
	R₄	1.483	-	-0.6	-	0.896	-0.67	44[70]
	R₆*	1.483	-	39.9	-	0.890	-1.33	
TNBMeOH	R₂**	1.486	-	-39.4	-	0.887	-1.66†	
	R₄	1.483	-	-0.2	-	0.896	-0.67	52[70]
	R₆*#	1.483	-	35.9	-	0.893	-1.00	

Table 2 (continued)

HEDM	Position[a]	d_{DFT} [Å]	d_{exp} [Å]	φ_{DFT} [°]	φ_{exp} [°]	WBI	%ΔWBI [%][b]	I.S. [cm][c]
TNBEtOH	R$_2$*	1.482	-	-43.9	-	0.890	-1.33	
	R$_4$	1.480	-	-2.5	-	0.899	-0.33	68[70]
	R$_6$**	1.487	-	-42.4	-	0.883	-2.11[†]	
Nitroanisoles								
DNAN	R$_2$*	1.475	1.469	41.0	18.4	0.903	+0.11[†]	>220[156]
	R$_4$	1.473	1.460	1.1	-15.4	0.913	+1.22	
TNAN	R$_2$	1.476	1.482	32.7	19.1	0.904	+0.22	
	R$_4$	1.477	1.470	1.0	0.9	0.905	+0.33	192[70]
	R$_6$	1.478	1.470	45.4	39.8	0.894	-0.89[†]	
ATNAN	R$_2$*#	1.469	1.471	-47.3	-51.4	0.915	+1.44[†]	
	R$_4$#	1.463	1.464	-5.0	8.8	0.946	+4.88	>325[70]
	R$_6$*	1.465	1.459	-24.9	-19.2	0.927	+2.77	
DMOTNB	R$_2$**	1.474	-	-62.5	-	0.891	-1.22[†]	
	R$_4$*/R$_6$*	1.477	-	-21.7, -21.6	-	0.909	+0.78	251[70]
DClTNAN	R$_2$**	1.478	-	-71.9	-	0.881	-2.33	
	R$_4$**	1.479	-	74.9	-	0.878	-2.66[†]	75[70]
	R$_6$**	1.476	-	-69.1	-	0.885	-1.88	
EOTNB	R$_2$*	1.480	1.462	30.8	-29.7	0.901	-0.11	
	R$_4$	1.479	1.467	1.6	-2.2	0.903	+0.11	190[70]
	R$_6$*	1.477	1.479	43.6	64.0	0.896	-0.67[†]	
DMDNPy	R$_3$*/R$_5$*	1.465	-	-25.8	-	0.925	+2.55	N/A
Nitroanilines								
DNPH	R$_2$#	1.461	1.437, 1.443	0.1	-8.3	0.952	+5.54	N/A
	R$_4$	1.466	1.450, 1.454	0.0	8.9	0.923	+2.33[†]	
TNA	R$_2$#/R$_6$#	1.472	1.453, 1.459	1.3, 1.5	-12.5, 26.0	0.936	+3.77	141[152]
	R$_4$	1.469	1.452	0.7	6.2	0.917	+1.66[†]	
DATB	R$_4$#/R$_6$#	1.458	1.435, 1.449	-0.3, 2.5	-4.1, 4.4	0.961	+6.54[†]	320[152]
	R$_2$##	1.444	1.430	11.0	2.5	1.015	+12.53	

Table 2 (continued)

HEDM	Position[a]	d_{DFT} [Å]	d_{exp} [Å]	φ_{DFT} [°]	φ_{exp} [°]	WBI	%ΔWBI [%][b]	I.S. [cm][c]
TATB	R$_2$##	1.437	1.416	-22.0	-0.8	1.032	+14.41	
	R$_4$##	1.437	1.417	-21.9	-2.4	1.032	+14.41	490[152]
	R$_6$##	1.437	1.423	-21.8	1.9	1.031	+14.30†	
TETNA	R$_6$#	1.472	1.461	-2.9	3.1	0.931	+3.22	
	R$_4$*	1.471	1.446	-24.8	-14.5	0.908	+0.67	
	R$_3$**	1.490	1.487	-65.3	-66.1	0.868	-3.77†	41[70]
	R$_2$*#	1.474	1.467	-40.1	-45.1	0.912	+1.11	
PNA	R$_2$*#/R$_6$*#	1.474	1.466, 1.467	-39.8, -36.4	-38.2, -34.3	0.911	+1.00	
	R$_3$**/R$_5$**	1.491	1.481, 1.480	-61.8, 119.1	-67.0, 114.7	0.868	-3.77†	22[152]
	R$_4$**	1.478	1.474	-47.1	-39.6	0.890	-1.33	
DADNPy	R$_3$#/R$_5$#	1.448	-	0.0	-	0.968	+7.32	N/A
LLM-105	R$_3$#/R$_5$#	1.471	1.455	0.0	18.1, -2.7	0.900	-0.22	117[157]
HNDPA	R$_2$#/R$_2$,#	1.474	1.473, 1.474	27.5	4.4, 10.7	0.912	+1.11	
	R$_4$/R$_4$,	1.478	1.467, 1.463	1.3	3.4, -11.8	0.903	+0.11	48[149]
	R$_6$/R$_6$,	1.482	1.487, 1.478	-38.7	-35.2, -40.5	0.897	-0.55†	
TETNPO	R$_5$#/R$_5$,#	1.472	-	-3.1, -3.6	-	0.928	+2.88	
	R$_3$/R$_3$,	1.476	-	-0.9, -1.0	-	0.908	+0.67†	N/A
DAHNBP	R$_6$*/R$_6$,*	1.473	-	-45.9, -44.2	-	0.910	+0.89†	
	R$_4$#/R$_4$,#	1.468	-	-1.6, -6.6	-	0.937	+3.88	67[152]
	R$_2$*#/R$_2$,*#	1.467	-	5.5	-	0.912	+1.11	
Nitrophenols								
2,4-DNP	R$_2$#	1.462	1.457	0.0	-4.0	0.942	+4.43	(>90 cm)[158]
	R$_4$	1.473	1.456	0.0	3.9	0.912	+1.11†	
2,6-DNP	R$_2$#	1.463	1.457	2.3	-0.8	0.944	+4.66	N/A
	R$_6$*	1.476	1.473	40.2	13.4	0.903	+0.11†	
2,4-DNR	R$_2$*#	1.459	-	24.5	-	0.951	+5.43†	296[149]
	R$_4$#	1.449	-	-0.7	-	0.971	+7.65	
4,6-DNR	R$_4$#/R$_6$#	1.455	1.444, 1.447	±2.2	-1.5, 1.3	0.955	+5.88	>320[149]

Table 2 (continued)

HEDM	Position[a]	d_{DFT} [Å]	d_{exp} [Å]	φ_{DFT} [°]	φ_{exp} [°]	WBI	%ΔWBI [%][b]	I.S. [cm][c]
PA	R$_2$*	1.478	1.482	-39.0	-18.8	0.899	-0.33[†]	
	R$_4$	1.475	1.464	-0.7	-4.8	0.907	+0.55	87[70]
	R$_6$[#]	1.467	1.458	-2.0	-3.5	0.935	+3.66	
TNR	R$_4$[#]/R$_6$[#]	1.457	1.456, 1.455	-1.5, -0.8	2.1, 2.7	0.948	+5.10	43[70]
	R$_2$**	1.477	1.468	68.4	66.1	0.888	-1.55[†]	
THTNB	R$_2$*[#]	1.454	1.436	21.3	4.7	0.964	+6.87	
	R$_4$[##]	1.429	1.435	4.8	6.8	1.031	+14.30	27[70]
	R$_6$**	1.475	1.465	68.3	62.7	0.891	-1.22[†]	
MTNP	R$_2$**	1.479	-	70.8	-	0.880	-2.44[†]	
	R$_6$[#]	1.461	-	1.9	-	0.940	+4.21	191[149]
	R$_4$*	1.476	-	-27.5	-	0.907	+0.55	
TNAP	R$_3$*[#]	1.468	-	38.6	-	0.920	+2.00	
	R$_2$*[#]	1.472	-	38.4	-	0.910	+0.89[†]	138[71]
	R$_5$[#]	1.476	-	11.1	-	0.923	+2.33	
DATNP	R$_2$[##]	1.423	1.409	-1.0	7.5	1.064	+17.96	
	R$_4$[##]	1.437	1.423	5.4	-13.3	1.034	+14.63	112[70]
	R$_6$*[#]	1.463	1.463	44.6	50.7	0.932	+3.33[†]	
HTNA	R$_2$*[#]	1.468	-	-43.5	-	0.922	+2.22[†]	
	R$_6$[#]	1.463	-	-5.6	-	0.947	+4.99	138[70]
	R$_4$[#]	1.449	-	-2.4	-	0.966	+7.10	
DHTNA	R$_2$[##]	1.429	1.420	-3.0	-11.8	1.041	+15.41	
	R$_4$**	1.474	1.449	-68.1	-57.2	0.893	-1.00[†]	32[70]
	R$_6$[##]	1.430	1.430	-4.0	1.4	1.041	+15.41	

Nitronaphthalenes

1,5-DNN	R$_1$/R$_5$	1.479	1.486	±37.6	±48.4	0.900	-0.22	(11.02 J)[159]
1,8-DNN	R$_1$*/R$_8$*	1.478	1.471, 1.476	-35.6, -35.7	-39.6, -37.7	0.895	-0.78	(18.37 J)[159]
TNN	R$_5$*	1.479	-	-39.5	-	0.894	-0.89	
	R$_4$*	1.481	-	-39.4	-	0.889	-1.44[†]	(9.52 J)[159]
	R$_1$	1.482	-	39.5	-	0.893	-1.00	
TETNN	R$_1$*/R$_4$*/ R$_5$*/R$_8$*	1.482	1.471, 1.486	40.6, ±36.9, -40.7	-	0.888	-1.55	(9.65 J)[159]

Table 2 (continued)

HEDM	Position[a]	d_{DFT} [Å]	d_{exp} [Å]	φ_{DFT} [°]	φ_{exp} [°]	WBI	%ΔWBI [%][b]	I.S. [cm][c]
Miscellaneous								
ClTNB	R$_2$/R$_6$	1.483	1.474, 1.476	-43.5, 46.0	-31.8, 69.4	0.888	-1.55[†]	79[70]
	R$_4$	1.481	1.467	0.7	-12.5	0.898	-0.44	
TNBN	R$_2$/R$_6$	1.485	-	34.0	-	0.890	-1.33[†]	140[70]
	R$_4$	1.486	-	2.1	-	0.892	-1.11	
TNBAl	R$_2$/R$_6$	1.484	-	±19.3	-	0.893	-1.00[†]	36[70]
	R$_4$	1.485	-	0.0	-	0.894	-0.89	
TNBA	R$_2$*	1.485	1.477	24.6	10.5	0.891	-1.22	
	R$_4$	1.485	1.477	1.9	-13.1	0.894	-0.89	109[70]
	R$_6$*	1.485	1.487	29.0	15.5	0.890	-1.33[†]	
ENTNB	R$_2$/R$_6$	1.485	-	±20.7	-	0.893	-1.00[†]	79[70]
	R$_4$	1.484	-	0.2	-	0.895	-0.78	
METNBA	R$_2$	1.485	-	-25.9	-	0.890	-1.33[†]	
	R$_4$	1.484	-	-2.1	-	0.894	-0.89	90[70]
	R$_6$	1.485	-	-29.0	-	0.891	-1.22	

[a] Energetic materials with [#] indicate the number of hydrogen bonds and * indicate the number of steric effects and/or repulsion. [b] The trigger bond is designated by a [†] when there is more than one. [c] Nitroaromatics with a lower limit for IS or IS with inconsistent methods (values in parentheses) were excluded from correlations with %ΔWBIs. [d] NB is documented as 1.464 Å in the cif and 1.467 Å by Boese et al.[150]

Wiberg Bond Index Analysis of Potential Trigger Bonds

WBIs were calculated from the DFT(M06-2X)/TZVP optimized geometries for the C(sp^2)-NO$_2$ trigger bonds of the 63 conventional nitroaromatic energetic molecules and compared to the C(sp^2)-NO$_2$ bond in reference molecule NB. The energetic molecules generally become more sensitive (i.e., more negative %ΔWBIs of the C-NO$_2$ trigger bond) with an increasing number of nitro groups as in the series DNT > TNT > TETNT > PNT (%ΔWBIs = -0.67%, -1.11%, -2.88% (average) and -2.99%); TNA > TETNA > PNA (%ΔWBIs = +1.66%, -3.77% and -3.77%,); 2,4-DNP > 2,6-DNP > PA (%ΔWBIs = +1.11%, +0.11% and -0.33%, respectively), 4,6-DNR > 2,4-

DNR > TNR (%ΔWBIs = +5.88%, +5.43% and -1.55%, respectively); and DNAN > TNAN (%ΔWBIs = +0.11% and -0.89%, respectively) as reflected in %ΔWBIs, consistent with available experimental sensitivity data (**Table 2**). Chlorination also activates $C-NO_2$ trigger bonds for ClMTNB versus TNT (%ΔWBIs = -1.88% and -1.11%, respectively) and DClTNAN versus TNAN (%ΔWBIs = -2.66% and -0.89%, respectively). Biphenyl systems with steric effects between $-CH_2-$ and repulsion between nitro groups enhance sensitivity in the series HNDPM < HNS < HNBP (%ΔWBIs = -2.44%, -1.33% and -0.89%, respectively), consistent with experiment. DNPH and DADNPy lack experimental impact sensitivity data, but are predicted to be more stable than TNA and LLM-105, respectively, based on %ΔWBIs (+2.33%, +9.31%, +1.66% and -0.22%, respectively) due to additional nitro groups and increased repulsion.

Under-prediction of the sensitivity based on the %ΔWBIs in the series DNB > TNB > TETNB > PNB > HNB (-0.55%, -1.00%, -3.44%, -3.33% and -3.33%, respectively) could be attributed to the differences in the dihedral angle of the nitro group with respect to the ring in the gas-phase versus the condensed phase. As the twist of the $-NO_2$ group increases from planar (0°) to perpendicular with the ring (90°) in NB, the $C-NO_2$ trigger bond becomes more activated (WBI (%ΔWBIs) = 0.902 (0.00%) and 0.873 (-3.22%), respectively) (**Figure 4**) because conjugation of the aromatic π-system with the nitro group is reduced. When the dihedral angles are constrained to the values in the X-ray structure of HNB (**Table 2**), the %ΔWBI shifts to -3.99% in agreement with the series. Similarly, %ΔWBI over-prediction of the sensitivity for TETNB could be attributed to dihedral angle differences between the phases, but experimental X-ray crystallographic evidence is necessary for validation. Similarly, crystal packing effects on condensed-phase dihedral angles for TETNA (-65.3° and -66.1°) and PNA (-61.8°/119.1° and -

67.0°/114.7°, respectively) may lead to under-estimation of their impact sensitivity from gas-phase structures.
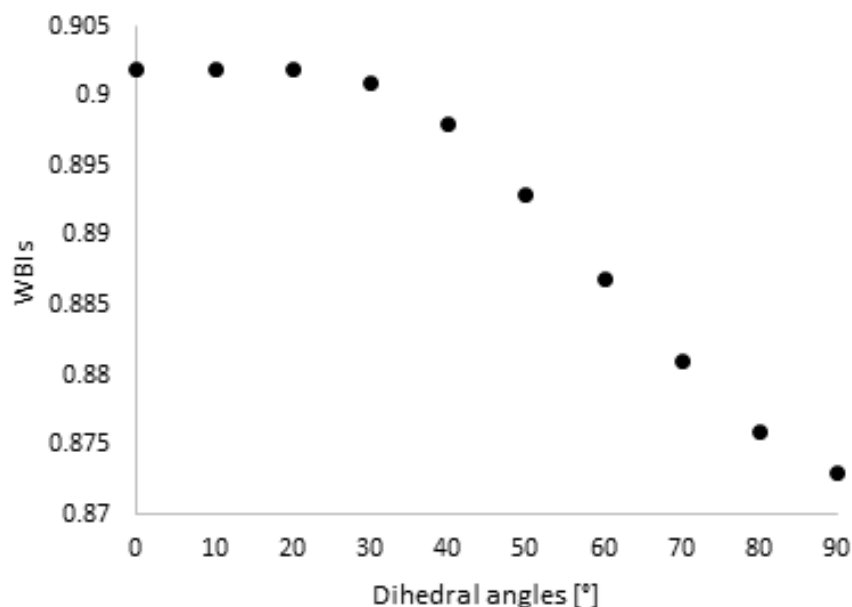
Figure 4. Bond Activation represented by smaller WBIs and increasing C-NO$_2$ dihedral angles in NB.

Intramolecular hydrogen bonding generally strengthens and deactivates C-NO$_2$ bonds. Energetic materials with these interactions would be expected to be less sensitive to decomposition. Contributions from resonance structures with C=N double bond character induced by intramolecular hydrogen bonding (**Figure 5**)[70-72] favor nearly planar nitro groups with shortened C-NO$_2$ bond lengths which are deactivated toward explosive decomposition. Therefore, C-NO$_2$ bonds influenced by hydrogen bonding interactions will not break as easily relative to isolated C-NO$_2$ bonds. Overall, C-NO$_2$ trigger bonds are deactivated by an increased number of –NH$_2$ substituents as in the series TNB < TNA < DATB < TATB (%ΔWBIs = -1.00%, +1.66%, +6.54% and +14.30%, respectively), as found in previous studies,[105, 136] TNAN to ATNAN

(%ΔWBIs = -0.89% and +1.44%, respectively) and TNT to ATNT (%ΔWBIs = -1.11% and +0.44%, respectively). Intramolecular hydrogen bonding in TATB strengthens all C-NO$_2$ trigger bonds to the extent that it is classified as an 'insensitive high explosive'.[7] Within this series not all nitro groups form trigger bonds. For example, TNB has three equivalent trigger bonds, but only the p-C-NO$_2$ bond of TNA can be assigned as such because it lacks the hydrogen bonding of the *ortho* groups (**Table 2** and **Figure 5**). Further increasing the number of hydrogen bonding interactions to a nitro group from one to two further enhances the double-bond character. In DATB, the trigger bond is the nitro with one hydrogen bond (dC-NO$_2$ = 1.458 Å (%ΔWBI = +6.54%)) given that the nitro group with two hydrogen bonding interactions is stabilized by enhanced partial double bond character (dC-NO$_2$ = 1.444 Å (%ΔWBI = +12.53%)) which agrees with previous results.[106] In addition, HNDPA and TETNPO have intramolecular hydrogen bonding with an –NH group which stabilized those C-NO$_2$ trigger bonds (**Scheme 4**). In HNDPA and TETNPO, *ortho* nitro groups are deactivated due to hydrogen bonding (%ΔWBIs = +1.11% and +0.67%, respectively) while the other *ortho* nitro groups in HNDPA are activated by steric effects (%ΔWBI = -0.55%). In addition, HNDPA would be more activated than TETNPO due to the number of nitro groups (i.e., 6 nitro groups and 4 nitro groups). However, %ΔWBIs indicate the opposite trend from TETNTs to ATETNTs (-2.88% (average) and -3.37% (average), respectively) because the planarity generally induced by hydrogen bonding interactions to the adjacent nitro groups force greater twists in nitro groups *meta* to the amine.
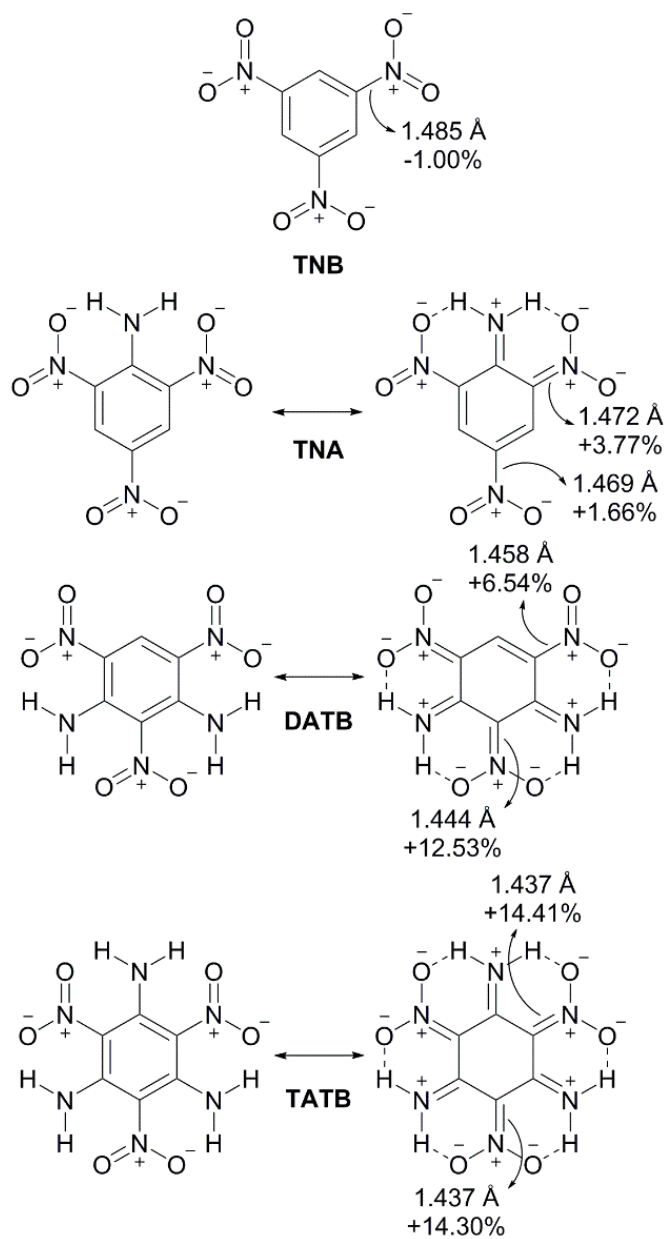
Figure 5. Resonance structures explaining trigger bond strength for nitro-amino interactions with select bond distances (Å) and %ΔWBIs (%).
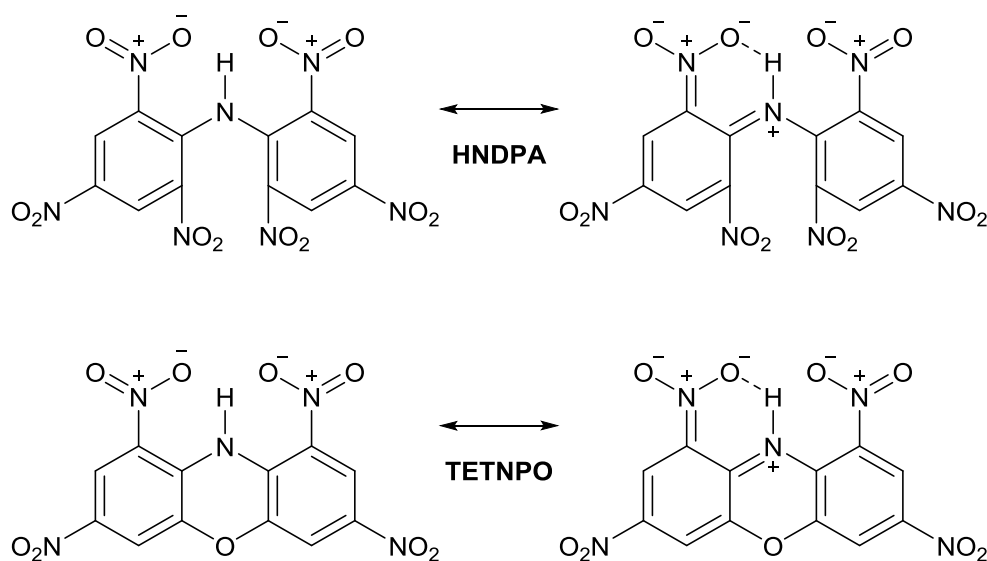
Scheme 4. C-NO$_2$ trigger bond stabilization from the intramolecular interaction with the –NH group in HNDPA and TETNPO.

In the phenol-based energetic molecules, resonance structures induced by hydrogen bonding with hydroxyl groups also enhance the double bond character of nitro groups (**Figure 2a** and **Table 2**). However, the unidirectionality of the phenol's hydrogen bonding leads to a repulsive interaction with its lone pair that forces a twist in the other *ortho* nitro group, activating it for decomposition as reflected in the %ΔWBIs and experimental data.[70, 152] For example, in PA (**Figure 6**), the bond to the nitro group involved in hydrogen bonding is strengthened by resonance (%ΔWBI = +3.66%) and its dihedral is near planar (-2.0°), but the nitro interacting with the lone pair is twisted (-39.0°) and activated (%ΔWBI = -0.33%). These results are in contrast with TNA in which hydrogen bonding leads to planarity in both *ortho* nitro groups (%ΔWBI = +3.77%) and shifts the trigger bond to the *para* position (%ΔWBI = +1.66%). Unlike the proposed nitronic acid, nitro groups in phenolic HEDMs are activated by the lone pairs from unidirectional hydrogen bonding.
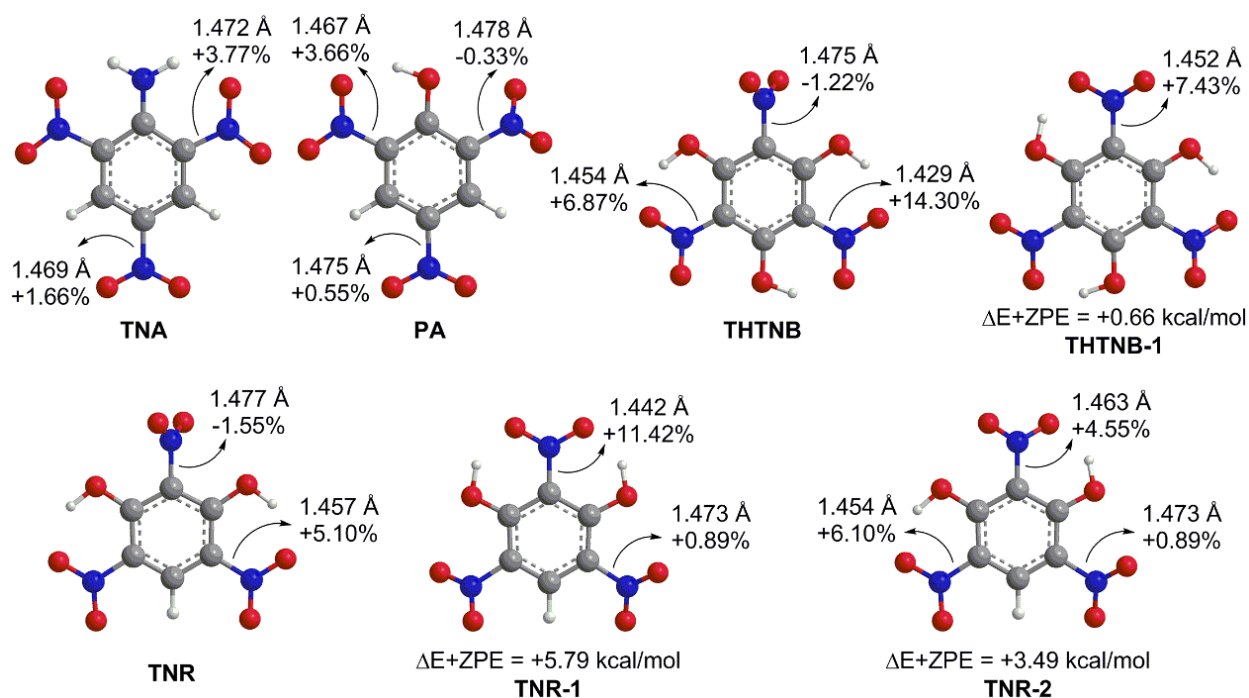
Figure 6. Select bond distances (Å) and %ΔWBIs (%) for trigger bonds in TNA, PA, TNR and THTNB.

In trinitrophenols with additional –OH groups, trigger bonds lacking hydrogen bonding are the most activated. In TNR (**Figure 6**), the –OH groups hydrogen bond to the nitro groups at the 4- and 6- positions and their lone pairs induce a twist in the 2-nitro group (68.4°) to activate it toward decomposition (%ΔWBI = -1.55%). Rearrangement of the hydrogen bonding pairs in **TNR-1** and **TNR-2** is less stable and results in less activated trigger bonds because the nitro groups are repelled by only one –OH lone pair. Similarly, the trigger bond in THTNB structure has no hydrogen bonding to its nitro, but those with one or two hydroxyl interactions are strengthened and more planar (**Figure 6**). Conformation **THTNB-1** with one hydrogen bond to each nitro is slightly higher in energy with planar, deactivated C-NO$_2$ bonds. Based on experiment, impact sensitivity should increase with the number of hydroxyl groups (PA > TNR > THTNB), which is

inconsistent with the trend in the gas-phase %ΔWBIs (-0.33%, -1.55% and -1.22%, respectively), possibly due to secondary crystal packing effects.

Steric effects should activate trigger bonds if they force an increase in the dihedral angle of the nitro group. For example, C-NO$_2$ bonds in TNT, TNBEtOH and TNBMeOH are more activated than TNB based on %ΔWBIs (-1.11%, -2.11% and -1.66%, respectively), consistent with experimental trends (**Table 2**). However, additional methyl groups stabilize nitrobenzyls for less impact sensitivity in the series TNT < DMTNB < TMTNB (**Table 2**) where %ΔWBIs predict increasing activation of the trigger bond (-1.11%, -3.10% and -2.77%, respectively). Similarly, in nitroanisoles, %ΔWBIs predict an increase in activation from TNAN to DMOTNB (-0.89% and -1.33%, respectively) that is not reflected in the experiment impact sensitivities (192 cm and 251 cm, respectively). The nitronaphthalenes have more activated C-NO$_2$ trigger bonds with repulsion from additional nitro groups in the series 1,5-DNN > 1,8-DNN > TNN > TETNN (%ΔWBIs = -0.22%, -0.78%, -1.44% and -1.55%, respectively), which do not agree with experimental impact sensitivity data. These anomalous results could be due to the differences in the nitro dihedral angles in the gas-phase and X-ray structure, resulting in over- or under-prediction of the trigger bond activation, or due to other crystal packing effects, such as shear slide.[160] Replacement of methoxy with ethoxy has little effect on the sensitivity of EOTNB relative to TNAN, where %ΔWBIs under-predict a differential in experimental sensitivity (-0.44% and -0.89%, respectively) due to larger nitro group dihedral angles in EOTNB (64.0° versus 40.8°). DMDNPy has deactivated nitro groups (%ΔWBI = +2.55%) and would be predicted to be relatively insensitive.

The activation of trigger bonds as measured by %ΔWBIs were compared with literature impact sensitivities determined using consistent experimental methods as these measurements often vary depending on the technique used.[17, 37, 131, 149, 152, 161-164] Values were selected from drop

hammer tests using Type 12 tooling (i.e., sandpaper) and a 2.5 kg drop weight[17, 149, 152, 161, 165] with the exception of TATB which was estimated from oxygen balance correlations.[17] In addition, nitroaromatic energetic materials with a reported lower limit for experimental impact sensitivity were excluded from the analysis of correlation with %ΔWBIs. The uncertainty in the drop hammer test can be large, by up to 15%,[166, 167] which will affect the quality of the comparison to %ΔWBI analysis. Since impact sensitivity tests are carried out in the condensed phase, intermolecular interactions not accounted for in gas-phase calculations will have a strong influence on the sensitivity of energetic materials. However, correlations with %ΔWBIs (i.e., information from gas-phase calculations) can provide a clue into how intramolecular interactions affect the sensitivity of these molecules.

%ΔWBIs for the nitroaromatic energetic molecules correlate well with experimental impact sensitivity ($R^2 = 0.741$) (**Figure 7a**) but not electrical spark sensitivity (**Figure A8**), which is highly dependent upon the configuration of the experiment.[168] %ΔWBIs measure bond strength and would not be expected to correlate with properties such as detonation velocity (the speed of a shock wave moving through an explosive column) or heat of explosion (a measure of breaking and re-forming bonds). Friction sensitivity was not compared with %ΔWBIs because these measurements are sparse and difficult to obtain for secondary explosives.[169] Early studies by Politzer and co-workers using low-level Mulliken population analysis (HF/STO-5G without geometry optimization) as an estimate of the electrostatic potential of the C-NO$_2$ bond found good correlation ($R^2 = 0.73$, note: the reported value of 0.86 in ref 70 is incorrect) to impact sensitivity for a set of 26 nitroaromatic compounds, but excluded nitrophenols as anomalous[70, 72] ($R^2 = 0.21$ including the nitrophenols). %ΔWBIs improve upon this method by using a higher level of theory

and larger basis sets on an optimized geometry and more directly measure the bond strength for a comparable correlation with a larger data set.

Individual subsets of the nitroaromatic energetic materials (**Figures 7c**) correlated well with experimental impact sensitivity for the nitrobenzenes ($R^2 = 0.878$), nitroanilines ($R^2 = 0.951$) and nitrophenols ($R^2 = 0.829$). However, %ΔWBIs are less predictive for the nitrobenzyls ($R^2 = 0.425$) and nitroanisoles ($R^2 = 0.645$) which could be attributed to secondary effects including strong hydrogen bonding networks, intermolecular repulsions, ring strain and other secondary effects in crystal packing. Eliminating these groups increases the overall correlation ($R^2 = 0.922$) (**Figure 7b**) indicating that further studies in the solid state may improve the computational prediction of trigger bond activation.
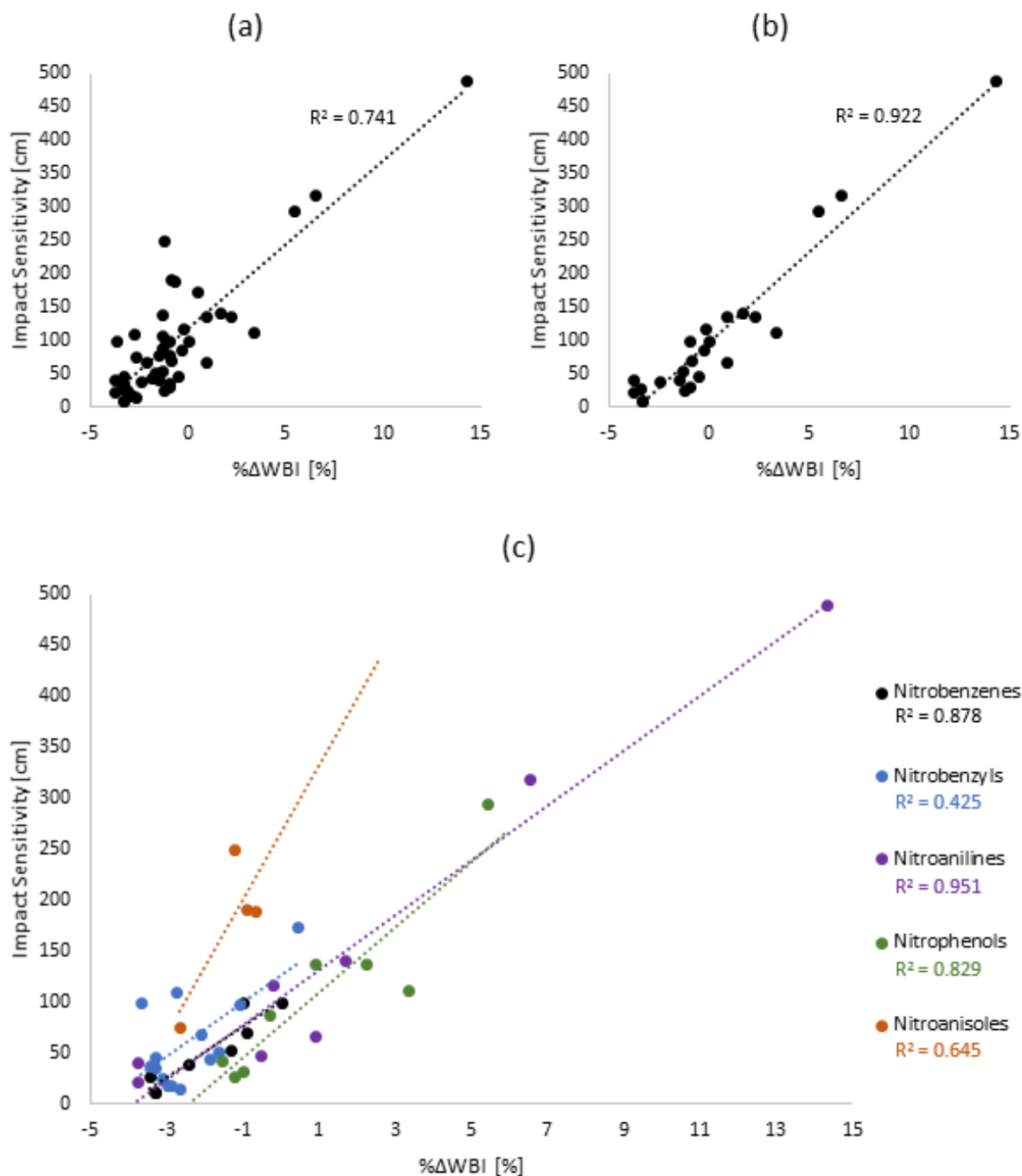
Figure 7. Correlation between %ΔWBIs and (a) experimental impact sensitivities (cm) (**Table 2**), (b) experimental impact sensitivities for the nitrobenzenes, nitroanilines and nitrophenols, excluding the nitrobenzyls, nitroanisoles, and miscellaneous (**Table 2**), (c) experimental impact sensitivities broken down by functional group excluding the miscellaneous (**Table 2**).

Comparison with Bond Dissociation Energies

DFT(M06-2X)/TZVP BDEs for homolysis of C-NO$_2$ bonds of the 63 nitroaromatic energetic molecules (**Table A1**) were compared to %ΔWBIs and energetic properties. %ΔWBIs are expected to be a better measure of bond strength for predicting sensitivity, as they focus on the strength of the intact bond rather than the energy of the broken bond. The range of BDEs are in agreement with experimental values from pyrolysis studies (~71 kcal/mol[61]) with additional –NO$_2$ and –OH groups contributing 1-4 kcal/mol.[61, 67] Although a previous study of BDEs on nitrophenols found that the O-H bond is the weakest,[143] the study was limited to the hydrogen bonded nitro *ortho* to –OH groups and did not consider BDEs for nitro groups not involved in hydrogen bonding which are more likely to be the trigger bond. Previous research has found nearly linear correlations with BDEs and the log of impact sensitivity[167] and impact sensitivity[157, 166] as well as roughly exponential correlation with impact sensitivity[160] for smaller datasets. Assignment of the trigger bond based on the BDE generally agrees with %ΔWBI, except in cases where intramolecular hydrogen bonding is important. Generally, BDEs are found to be poor predictors of impact sensitivity ($R^2 = 0.482$) (**Figure 8a**) for the present dataset with only slight improvement using BDEs of the trigger bonds assigned by %ΔWBIs ($R^2 = 0.490$) (**Figure 8b**). The correlations with BDEs are inferior when compared to WBIs likely due to the fact that BDEs are calculated for a bond that has already been broken while WBIs are calculated for bond that remains intact.
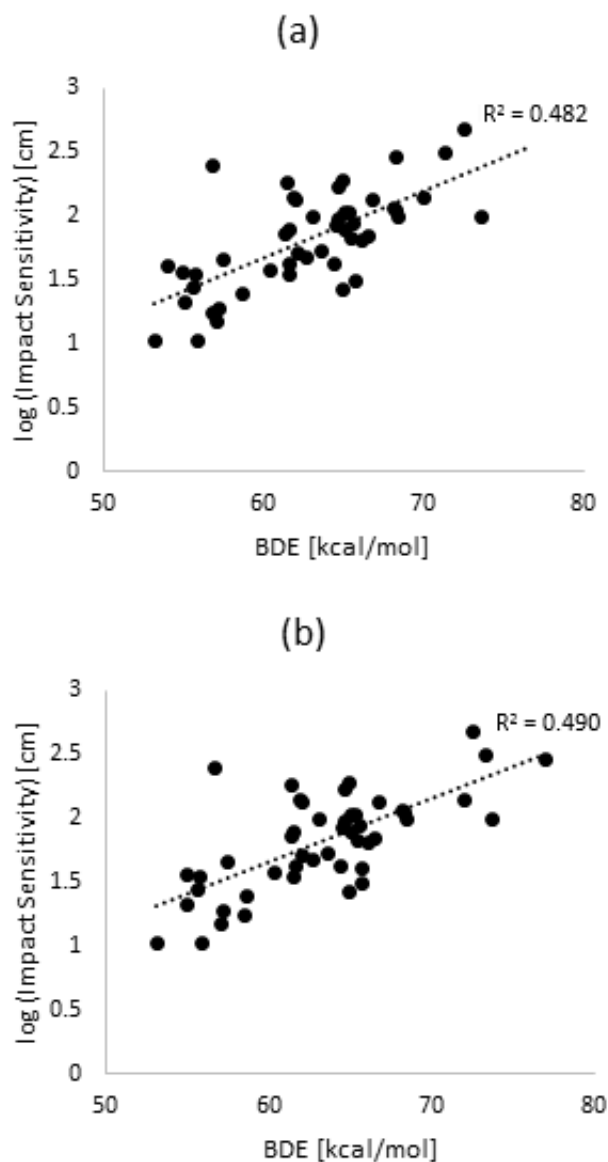
Figure 8. Correlations between log (impact sensitivity) (cm) and (a) BDEs, (b) BDEs as assigned by WBIs.

Conclusions

Trigger bonds were assigned to 63 nitroaromatic energetic materials by comparing their WBIs to those in reference molecule NB for a relative measure of activation of the $C-NO_2$ bond. Based on this definition, trigger bonds with lower electron density than the reference as reflected in a negative %ΔWBI are therefore more susceptible to cleavage under stress. These bonds were

activated as the number of nitro groups was increased. Greater twists in the nitro group with respect to the ring (i.e., closer to 90°) lead to more negative %ΔWBIs. Based on the analysis, all nitro groups within a molecule are not necessarily equally activated to contribute to explosive decomposition initiation. Generally, steric effects and repulsion with adjacent functional groups induce twists that activate the C-NO$_2$ trigger bonds, but intramolecular hydrogen bonding interactions favor planarity, enhanced stability, and deactivated C-NO$_2$ bonds as found in the series of nitroanilines (TNB < TNA < DATB < TATB). However, unidirectional hydrogen bonding interactions in nitrophenols deactivate the nitro involved in hydrogen bonding, but activate any nitro repelled by the lone pair of the –OH group. In some subsets, secondary effects are not recovered through gas-phase calculations and may need to be modeled in the condensed-phase. Overall, %ΔWBIs can assign trigger bonds to help interpret impact sensitivities by understanding the influence of intramolecular interactions and explore trends with energetic properties in novel, 'green' HEDMs.

CHAPTER 3

MECHANISTIC STUDY OF SIMPLE AROMATIC AZIDE COMPOUNDS AS A MODEL

FOR EXPLOSIVE DECOMPOSITION IN AROMATIC AZIDE-BASED ENERGETIC

MATERIALS

Introduction

Since the discovery of phenyl azide (PhN_3) in 1864,[170] the chemistry of azides is of interest in organic synthesis,[171] nanotechnology,[172, 173] pharmacology[174] and photochemistry.[175-179] Azide functional groups are often incorporated into high energy density materials (HEDMs) in order to enhance efficiency, increase stability and lower environmental toxicity by releasing nontoxic nitrogen gas.[1, 4, 10, 12, 180] Explosophores[5] such as azide ($-N_3$)[11] and nitro ($-NO_2$)[52-56] are functional groups that form trigger bonds, activated bonds that break to initiate explosive decomposition.[16, 49] Our group has shown that the Wiberg bond index (WBI), a measure of interatomic electron density, is a computationally efficient means of proposing trigger bonds in energetic materials (Equation 24).[16, 49] Identifying these bonds with WBIs can guide the characterization of the initiation mechanisms of explosive decomposition and rationalization of energetic properties, such as impact sensitivity. Understanding the mechanisms of N_2 release in azide-based HEDMs is necessary in order to rationalize their enhanced sensitivity.

$$WBI_{AB} = \sum_{p \in A} \sum_{q \in B} (D_{pq})^2 \tag{24}$$

Trigger bonds are influenced by steric effects, electron-withdrawing groups and ring strain.[16, 49] Trigger bonds are expected to be longer and have lower electron density relative to inactivated bonds of the same type, hybridization and explosophore (i.e., bonds in reference molecules). A relative scale for trigger bond activation (%ΔWBI) has been previously proposed

by our group (Equation 25) by comparing the WBI of bond in HEDMs to those in chemically similar reference molecules.[16, 49] More negative $\%\Delta$WBIs indicate more activated trigger bonds and will most likely break first to initiate explosive decomposition.[16, 49] Our previous study considered only HEDMs with $-NO_2$ trigger bonds. In this paper, azide trigger bonds are characterized to differentiate between the sensitivities of the two explosophores.

$$\%\Delta\text{WBI}_{AB} = \frac{\text{WBI}_{AB}^{\text{HEDM}} - \text{WBI}_{AB}^{\text{reference}}}{\text{WBI}_{AB}^{\text{reference}}} \times 100 \tag{25}$$

Many simple azide-based molecules have been studied both theoretically[181-190] and experimentally.[176, 177, 191-200] Pyrolysis studies have shown that the mechanism of methyl azide (CH_3N_3) involves $N-N_2$ bond cleavage with the formation of a triplet methylnitrene $(^3CH_3N)$ through intersystem crossing.[196, 197] However, other experimental studies indicate the dominant pathway involves hydrogen transfer connected with $N-N_2$ bond cleavage to form a singlet methyleneimine (CH_2NH).[198-200] Studies on ethyl azide $(CH_3CH_2N_3)$ produce nitrogen gas and ethyleneimine (CH_3CHNH), further supporting the hydrogen transfer pathway.[198-200] Several MP2 studies of methyl azide agree with the hydrogen transfer pathway[184, 201] while higher level CASSCF calculations indicate that the intersystem crossing path is more probable.[182-184, 202] Experimental photochemical studies on azidobenzene (AzB) indicate the loss of N_2 and the formation of phenylnitrene[176, 177, 179] in the singlet state (^1PhN) or the triplet state (^3PhN)[179] via intersystem crossing (**Figure 9**).[186] Electron-spin resonance (ESR) studies of AzB have found that the triplet is more stable than the singlet.[177, 203] Decomposition of AzB is concentration dependent. At low concentrations, dimerization of phenyl nitrene occurs upon irradiation whereas phenyl nitrene reacts with AzB at higher concentrations.[177]
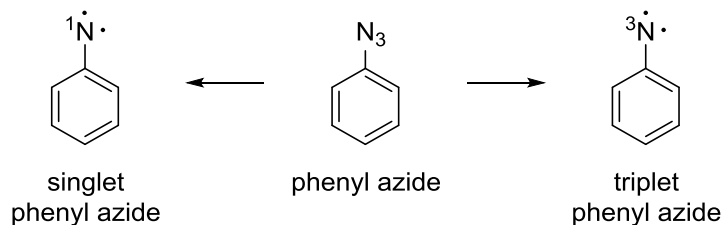
Figure 9. Decomposition of AzB.

In o-nitroazidobenzene (o-NAzB), the azide group will undergo cyclization with the *ortho* nitro group,[67, 187] similar to proposed cyclization reactions of nitro groups with adjacent methyl or amino groups (**Figure 10**).[67] Experimentally, the reaction rate is slower for *meta* and *para* nitro groups (i.e., E_a = +40.6 kcal/mol (p-NO$_2$) and +26.1 kcal/mol (o-NO$_2$)), since cyclization is not possible (**Figure 10**).[67] In contrast, based on ESR studies of AzB,[177] it is expected that *m*-nitroazidobenzene (m-NAzB) and p-nitroazidobenzene (p-NAzB) would also decompose as a triplet, since the nitro group is not in the *ortho* position. Thermolysis indicates that o-NAzB derivatives are insensitive to the presence of other groups because cyclization is the dominant reaction (**Figure 10c**); however, the homolysis pathway (**Figure 10d**) is accelerated by electron-withdrawing groups substituted in the *para* position.[67, 204]

Azide-based HEDMs have been studied due to their high nitrogen content, which can improve burning rates, performance, and nontoxic nitrogen gas production,[1, 10] as well as enhance energetic properties.[4, 8, 10] 2-azido-1,3-imidazole, 3-azido-1H-1,2,4-triazole, 5-azido-1H-tetrazole and azidopentazole have comparable energetic properties to 1,3,5,7-tetranitro-1,3,5,7-tetrazacyclooctane (HMX), and therefore have been studied to understand their decomposition mechanisms.[190] The study included possible mechanisms involving azide bond (-N-N≡N) breaking as well as ring fission pathways, where azide-azole isomerization participates in the pyrolysis of 2-azido-1,3-imidazole and 3-azido-1H-1,2,4-triazole while ring fission occurs in the pyrolysis of

5-azido-1*H*-tetrazole and azidopentazole.[190] Azidonitroaromatic derivatives have been studied due to their relatively high velocities of detonation, which are comparable and often superior to TNT.[165] Furthermore, the energetic properties of TAzTNB were found to be comparable to HMX,[13] which makes it a candidate to potentially replace HMX in real-world systems. Thermal decomposition investigations have determined that azidonitroaromatic derivatives form benzofuroxan derivatives upon N_2 extrusion.[67, 205] Additionally, the experimental activation energy of TAzTNB from thermal decomposition is comparable to that of *o*-NAzB and lower than the activation energy of *p*-NAzB (E_a = +26.0 kcal/mol, +26.1 kcal/mol and +40.6 kcal/mol, respectively), suggesting that TAzTNB will decompose through cyclization.[67]
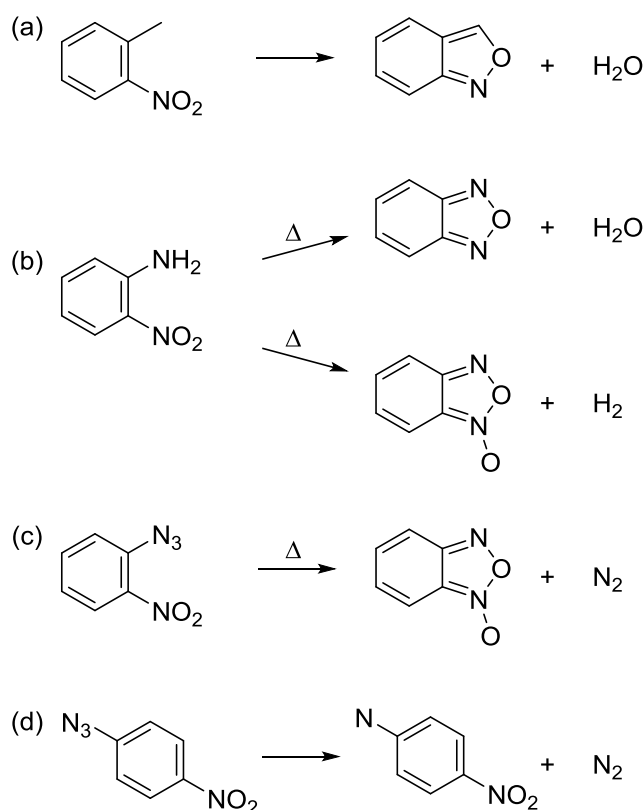
Figure 10. Cyclization reactions in nitroaromatics with (a) *ortho* methyl, (b) *ortho* amino, (c) *ortho* azide and (d) *para* azide groups.

In this study, density functional theory (DFT) calculations were used to propose reaction pathways important to the explosive decomposition of several simple azides and azide-based HEDMs, including *o*-NAzB, *m*-NAzB, *p*-NAzB, AzB, azido-2,4,6-trinitrobenzene (AzTNB), azidopentanitrobenzene (AzPNB), and 1,3,5-triazido-2,4,6-trinitrobenzene (TAzTNB). The potential explosive decomposition pathways include azide homolysis as well as cyclization when an *ortho* nitro group is present. The results will be used to rationalize the sensitivity observed in azide-based energetic materials and differentiate between the explosophore activations.

Computational Methods

DFT-optimized geometries of the simple azides and azide-based HEDMs (**Scheme 5**) were calculated using Gaussian 09[46] and the hybrid functional M06-2X[35] paired with a triple-ζ basis set (TZVP),[48] as in our previous study.[49] WBIs for each potential trigger bond were calculated using Natural Bond Orbital (NBO) version 3.1.[50, 51] %ΔWBIs were determined from reference molecules nitrobenzene (NB) and azidobenzene (AzB), which contain the same bond type, hybridization and explosophore as the HEDMs. Vibrational analysis characterized the structures as minima on the potential energy surface. Transition states were identified by only one imaginary vibrational frequency. Transition states were found by mapping the potential energy surface of the compounds along the N-N_2 coordinate. Unrestricted open-shell and restricted closed-shell calculations for potential initiation of explosive decomposition were used to determine the most probable pathway within the energetic materials.
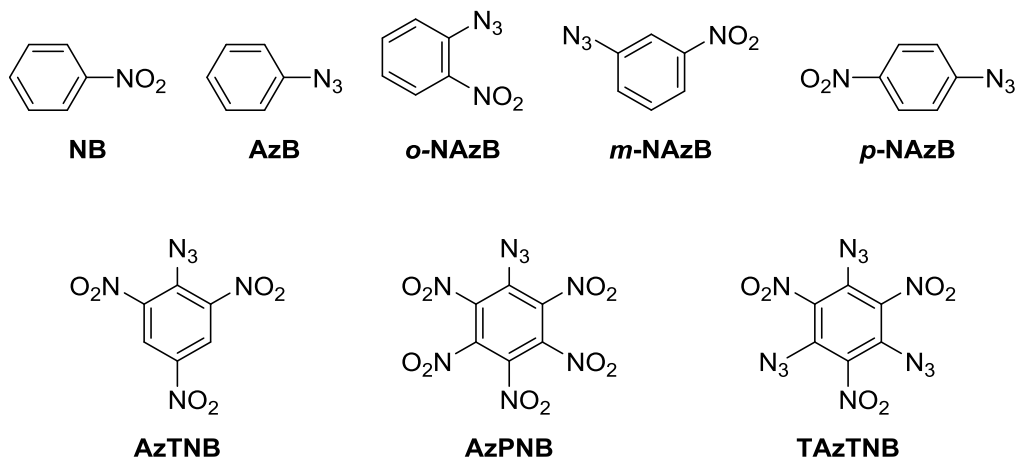
Scheme 5. The simple azide and azide-based HEDMs included in this study.

Results and Discussion

The DFT(M06-2X)/TZVP optimized structures of the simple azides (**Figure 11**) and azide-based HEDMs (**Figure 12**) are in good agreement with available X-ray crystallographic data[13, 150, 205, 206] (**Table 3**) and previous computational results.[13, 205] Generally, the DFT-optimized N-N_2 bond distances are shorter than experimental values while the C-NO_2 bond distances are slightly longer (**Table 3**).[13, 150, 205, 206] The simple aromatic azides prefer to have the azide group in the plane of the ring (**Figure 11**). Additionally, the nitro groups in *m*-NAzB and *p*-NAzB are planar with the ring, while the nitro group in *o*-NAzB is slightly twisted due to repulsion with the adjacent azide group.
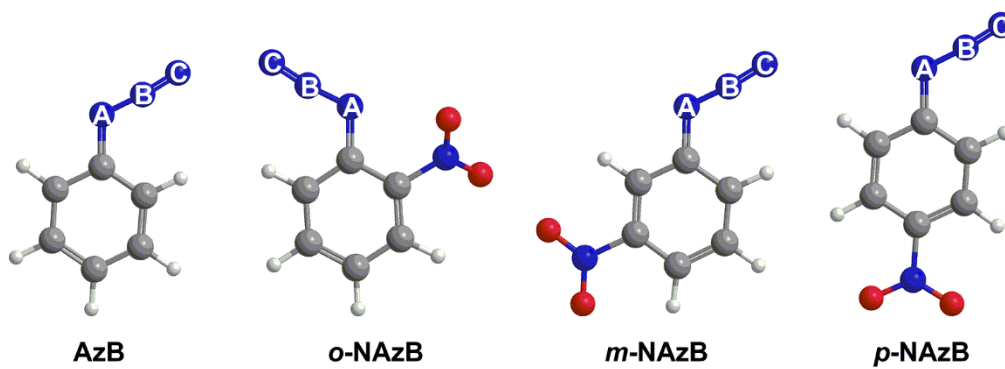
Figure 11. DFT(M06-2X)/TZVP optimized structures of the simple aromatic azides.
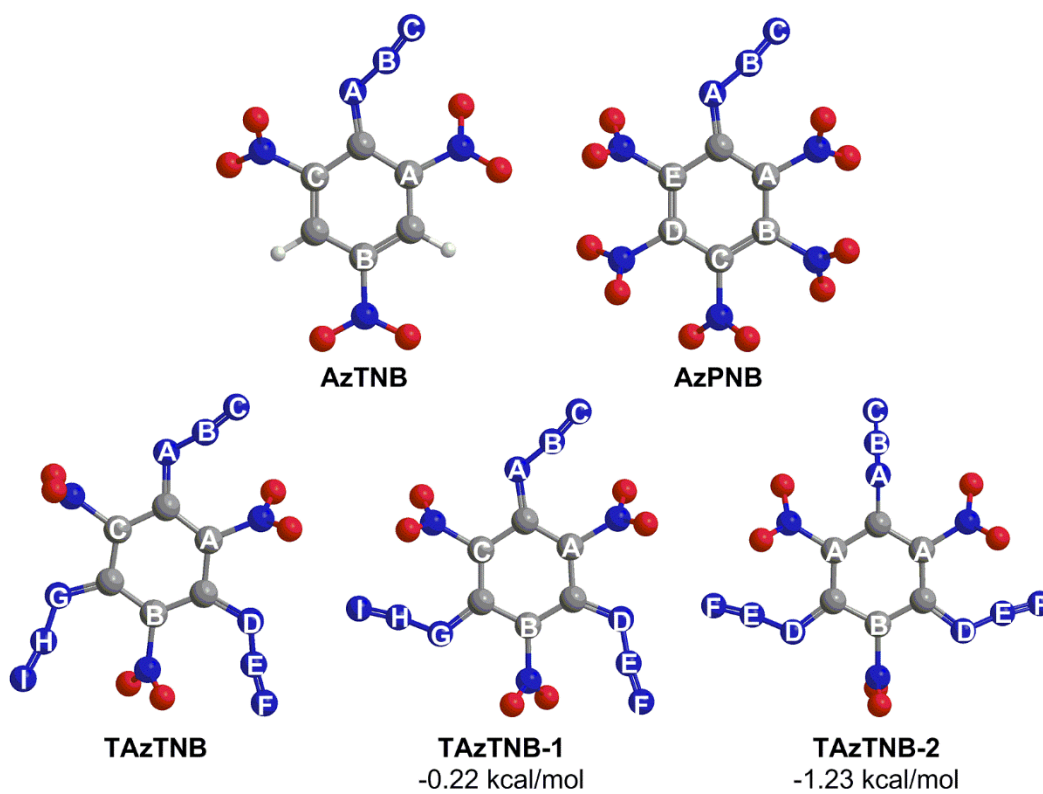
Figure 12. DFT(M06-2X)/TZVP optimized structures of the azide-based HEDMs.

Table 3. Comparison of available experimental and DFT(M06-2X)/TZVP bond distances [Å], dihedral angles [°] and WBIs for C-NO$_2$ and N-N$_2$ bonds in the energetic materials and references with the corresponding experimental impact sensitivity (I.S.) [cm].[13, 150, 205, 206]

Compound	Bond	d_{DFT} [Å]	d_{exp} [Å]	φ_{DFT} [°]	φ_{exp} [°]	WBI	%ΔWBI [%]	I.S. [cm]
Reference								
NB[49]	C-NO$_2$	1.481	1.464	0.0	1.7	0.9022	0	100
AzB	N$_A$-N$_B$	1.228	-	0.0	-	1.4627	0	N/A
	N$_B$-N$_C$	1.192	-	-	-	2.3904	0	
o-NAzB	N$_A$-N$_B$	1.231	1.247	3.4	-2.9	1.4401	-1.55	N/A
	N$_B$-N$_C$	1.117	1.129	-	-	2.4110	+0.86	
	C-NO$_2$	1.475	1.467	39.4	-37.7	0.9029	+0.08	
m-NAzB	N$_A$-N$_B$	1.231	-	0.0	-	1.4463	-1.12	N/A
	N$_B$-N$_C$	1.117	-	-	-	2.4072	+0.70	
	C-NO$_2$	1.483	-	0.0	-	0.8983	-0.43	
p-NAzB	N$_A$-N$_B$	1.233	-	0.1	-	1.4376	-1.72	N/A
	N$_B$-N$_C$	1.117	-	-	-	2.4163	+1.08	
	C-NO$_2$	1.474	-	0.0	-	0.9128	+1.17	
HEDMs								
AzTNB	N$_A$-N$_B$	1.239	1.251	-29.9	-	1.3852	-5.30	19[152]
	N$_B$-N$_C$	1.111	1.115	-	-	2.4682	+3.25	
	o-C$_A$-NO$_2$	1.477	1.467	-31.9	-18.9	0.9066	+0.49	
	p-C$_B$-NO$_2$	1.477	1.467	-0.9	0.9	0.9044	+0.24	
	o-C$_C$-NO$_2$	1.481	1.472	-50.4	-73.5	0.8880	-1.57	
AzPNB	N$_A$-N$_B$	1.244	-	21.2	-	1.3676	-6.50	17[152]
	N$_B$-N$_C$	1.110	-	-	-	2.4813	+3.80	
	o-C$_A$-NO$_2$	1.480	-	56.3	-	0.8859	-1.81	
	m-C$_B$-NO$_2$	1.489	-	56.5	-	0.8723	-3.31	
	p-C$_C$-NO$_2$	1.482	-	49.4	-	0.8826	-2.17	
	m-C$_D$-NO$_2$	1.487	-	53.5	-	0.8745	-3.07	
	o-C$_E$-NO$_2$	1.485	-	64.4	-	0.8758	-2.93	
TAzTNB	N$_A$-N$_B$	1.243	1.236	-18.5	-22.4	1.3826	-5.48	60[13]
	N$_B$-N$_C$	1.111	1.129	-	-	2.4678	+3.24	
	N$_D$-N$_E$	1.240	1.245	23.2	23.1	1.3890	-5.04	
	N$_E$-N$_F$	1.111	1.120	-	-	2.4607	+2.94	
	N$_G$-N$_H$	1.240	1.252	28.3	24.8	1.3908	-4.92	
	N$_H$-N$_I$	1.111	1.115	-	-	2.4615	+2.97	
	C$_A$-NO$_2$	1.475	1.464	-68.3	-66.8	0.8898	-1.37	
	C$_B$-NO$_2$	1.467	1.471	49.1	61.3	0.9137	+1.27	
	C$_C$-NO$_2$	1.477	1.473	-91.4	-87.9	0.8781	-2.67	
TAzTNB-1	N$_A$-N$_B$	1.242	-	-15.5	-	1.3844	-5.35	
	N$_B$-N$_C$	1.111	-	-	-	2.4644	+3.10	
	N$_D$-N$_E$	1.241	-	-22.8	-	1.3882	-5.09	
	N$_E$-N$_F$	1.111	-	-	-	2.4615	+2.97	
	N$_G$-N$_H$	1.242	-	14.9	-	1.3834	-5.42	
	N$_H$-N$_I$	1.111	-	-	-	2.4651	+3.13	
	C$_A$-NO$_2$	1.474	-	-63.1	-	0.8944	-0.86	
	C$_B$-NO$_2$	1.475	-	-67.7	-	0.8905	-1.30	
	C$_C$-NO$_2$	1.474	-	66.5	-	0.8916	-1.17	

Table 3 (continued)

Compound	Bond	d_{DFT} [Å]	d_{exp} [Å]	φ_{DFT} [°]	φ_{exp} [°]	WBI	%ΔWBI [%]	I.S. [cm]
TAzTNB-2	N_A-N_B	1.240	-	96.6	-	1.3936	-4.72	
	N_B-N_C	1.110	-	-	-	2.4738	+3.49	
	N_D-N_E	1.242	-	22.5, -22.6	-	1.3833	-5.43	
	N_E-N_F	1.111	-	-	-	2.4689	+3.28	
	C_A-NO_2	1.468	-	50.1, -47.6	-	0.9078	+0.62	
	C_B-NO_2	1.478	-	92.1	-	0.8769	-2.80	

The azide-based HEDMs can have the azide oriented in or out of the plane of the ring (**Figure 12**). AzTNB, optimized from the X-ray crystal structure, and AzPNB have the azides in the plane of the ring. TAzTNB was optimized from the X-ray crystal structure, but conformations TAzTNB-1 (i.e., pin-wheel arrangement of the azides) and TAzTNB-2 (i.e., azide out of plane of the ring) were lower in energy (ΔE+ZPE = -0.22 kcal/mol and -1.23 kcal/mol, respectively) due to the orientations of the azide groups. In TAzTNB, the C_C-NO_2 nitro is nearly perpendicular to the ring thereby interacting with N_A and N_G electrostatically and the C_A-NO_2 nitro sterically interacts with N_D, while the C_B-NO_2 nitro lacks any intramolecular azide interaction. The nitro groups in TAzTNB-1 each have one azide interaction, which could explain why it is a lower energy conformation. In TAzTNB-2, the C_B-NO_2 nitro is nearly perpendicular to the ring and has two electrostatic interactions with the N_D azides while the C_A-NO_2 nitro lacks an azide interaction because N_A is not in the plane of the ring. Since N_A is out of the plane of the ring in TAzTNB-2, it does not interact with any of the nitro groups which could contribute to the lower energy. Similarly to our previous study,[49] steric effects between functional groups along with the number of explosophores influence the activation of the C-NO_2 trigger bonds . Furthermore, the activation of the N-N_2 trigger bond will likely be affected by repulsion with nitro groups as well as the number of -N_3 trigger linkages.

Mechanisms of Simple Azides and Azide-Based HEDMs

N_2 extrusion for the simple azides (i.e., N-N_2 bond breaking) (**Figures 13-14**) were modeled at the DFT(M06-2X)/TZVP level of theory in order to guide those in the more complex azide-based HEDMs. The activation energies of the structures are referenced to the singlet reactant. The transition states were determined by mapping the potential energy surface along the N-N_2 bond-breaking pathway. In our calculations, the triplet phenyl nitrene product is significantly lower in energy than the closed-shell or open-shell singlet nitrene (ΔE+ZPE = +45.56 and +11.54 kcal/mol, respectively), in agreement with ESR studies finding the triplet state to be the ground state[177] as well as the singlet-triplet gap to be +15 kcal/mol computationally[204] and +31.2 kcal/mol experimentally.[203] *m*-NAzB and *p*-NAzB would also be expected to decompose to the triplet phenyl nitrene, because the nitro group is not *ortho* to the azide group (**Figure 11**). Comparing the N-N_2 bond of AzB to the C-NO_2 bond in NB indicates that N_2 release has a lower activation energy (E_a = +38.29 kcal/mol, **Figure 13**) than C-NO_2 homolysis (E_a = +68.2 kcal/mol).[67]
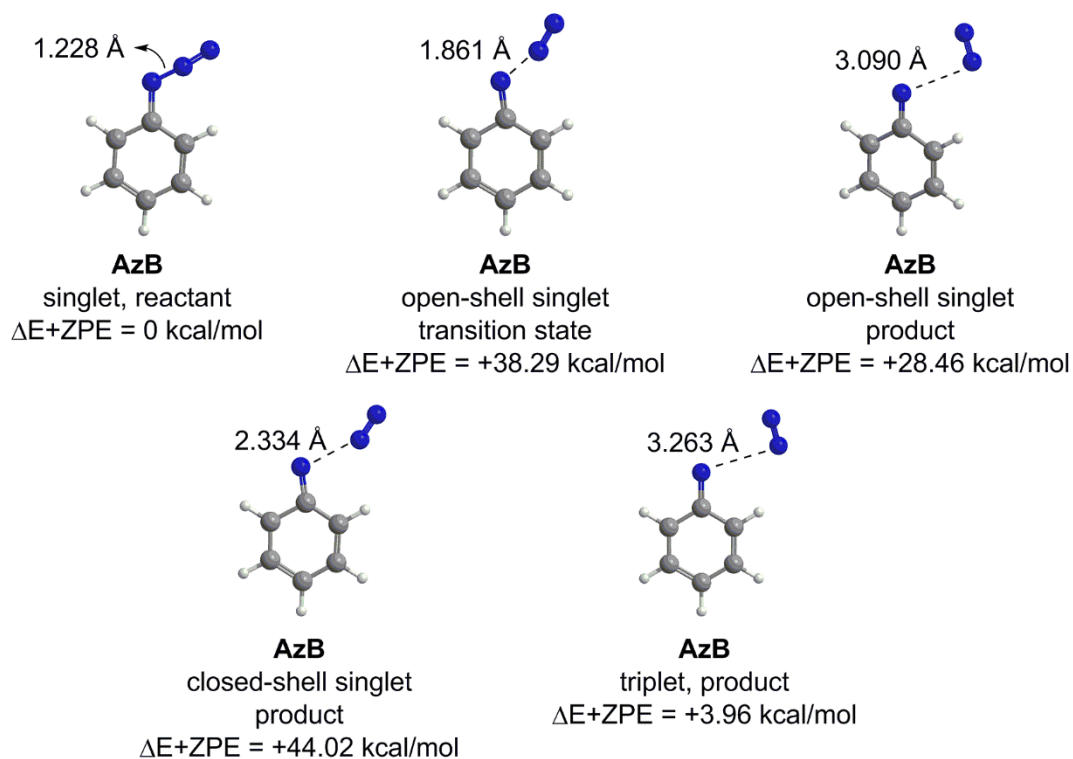
Figure 13. DFT(M06-2X)/TZVP optimized structures on the singlet and triplet surfaces of AzB for the reactant, transition state and products.
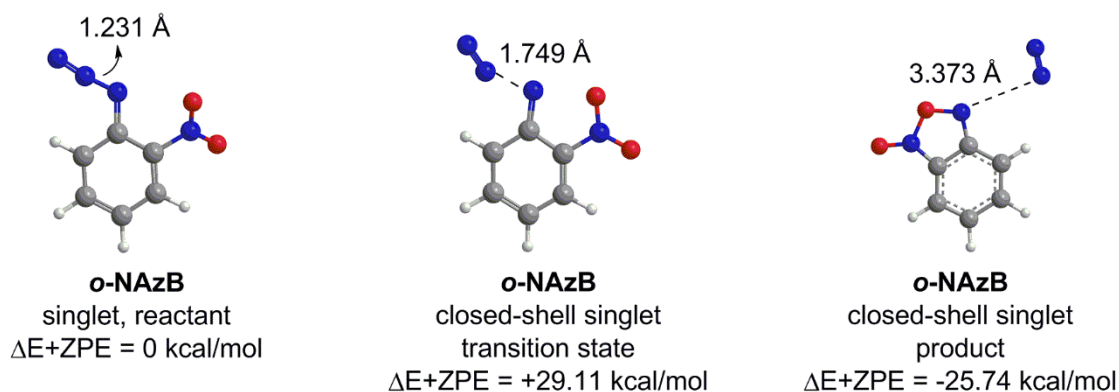
Figure 14. DFT(M06-2X)/TZVP optimized structrues of *o*-NAzB on the singlet surface for reactant, transition state and product.

Thermal decomposition of *o*-NAzB has a lower experimental activation energy than *p*-NAzB (E_a = +26.1 kcal/mol and +40.6 kcal/mol, respectively) and undergoes thermolysis at a

faster rate than m-NAzB and p-NAzB[67] due to release of N_2 through cyclization with the adjacent nitro group on the singlet surface. Our DFT(M06-2X)/TZVP activation barrier for o-NAzB (E_a = +29.11 kcal/mol, **Figure 14**) is in good agreement with experiment (E_a = +26.1 kcal/mol).[67] Adding the nitro group in o-NAzB further lowers the activation energy when compared to AzB (E_a = +29.11 kcal/mol and +38.29 kcal/mol, respectively). Since the activation energy of the azide group is significantly lower for o-NAzB (i.e., breaking the N-N_2 bond, +26.1 kcal/mol) than NB (i.e., breaking the C-NO_2 bond, +68.2 kcal/mol),[67] our study was limited to the mechanism of the azide even though both potential trigger bonds are observed in the aromatic azide-based HEDMs. The triplet nitrene is lower in energy for m-NAzB and p-NAzB than the closed-shell and open-shell singlet nitrenes (E_a = +45.43 kcal/mol (m-NAzB), +41.43 kcal/mol (p-NAzB); +12.09 kcal/mol (m-NAzB) and +11.44 kcal/mol (p-NAzB), respectively). The o-NAzB closed-shell singlet optimizes to the desired benzofuroxan and is lower in energy than the open-shell singlet nitrene and triplet nitrene (E_a = +32.16 kcal/mol and +20.44 kcal/mol, respectively). Therefore, the triplet and open-shell singlet surfaces were not considered for aromatic azide-based HEDMs with *ortho* nitro groups.

The DFT(M06-2X)/TZVP activation energies for N_2 extrusion in AzTNB and AzPNB (E_a = +28.05 kcal/mol and +31.91 kcal/mol, respectively, **Figure 15**) are consistent with experimental data for o-NAzB (E_a = +26.1 kcal/mol).[67] AzTNB has the azide in the plane of the ring, producing the desired benzofuroxan derivative (E_a = -28.78 kcal/mol, **Figure 15a**). AzPNB also formed the desired benzofuroxan derivative with the adjacent nitro group while releasing N_2 (E_a = -26.27 kcal/mol, **Figure 15b**). A three-membered ring, termed benzazirine, has been observed computationally for aryl azides but the very small activation barrier between benzazirine and the cyclic ketenimine makes experimental observation rare.[207]
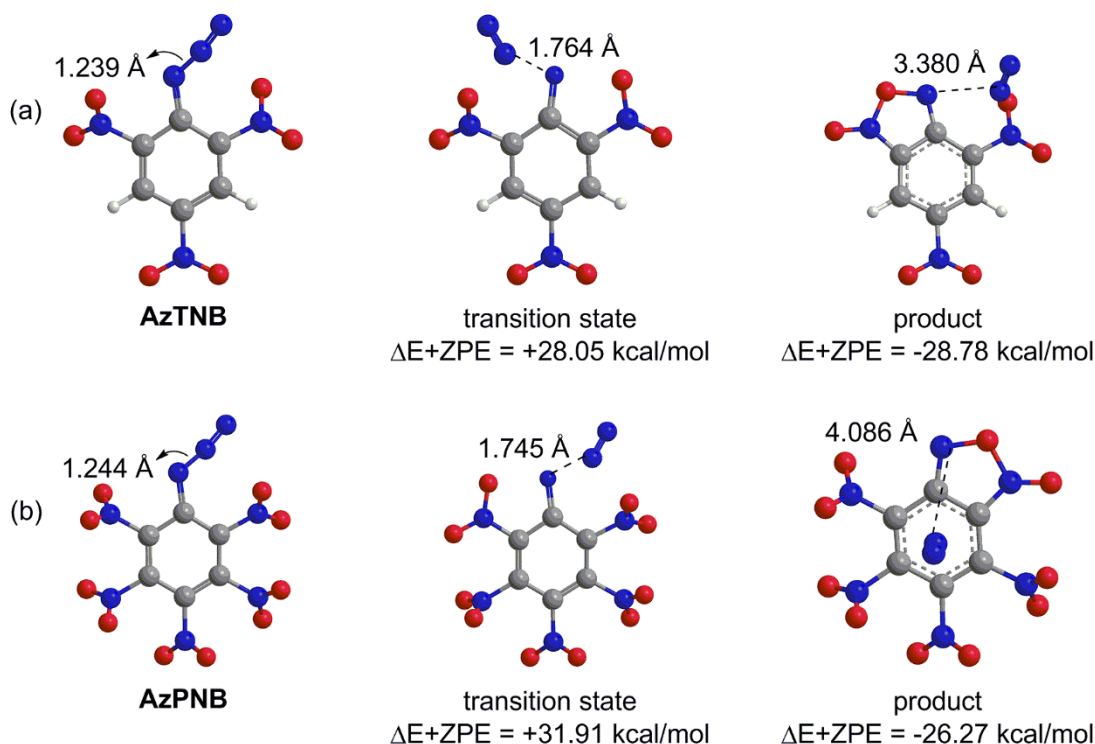
Figure 15. DFT(M06-2X)/TZVP optimized structures on the singlet surfaces for N_2 extrusion for (a) AzTNB and (b) AzPNB.

In order to propose the stability of multiple azide groups on a nitroaromatic backbone, three conformations of TAzTNB were examined (**Figure 12**), including the X-ray crystal structure (TAzTNB, **Figure 16**), a pin-wheel arrangement (TAzTNB-1, **Figure 17a**), and one with an azide out of plane with the ring (TAzTNB-2, **Figure 17b**). All conformations of TAzTNB extrude N_2 to produce a benzofuroxan derivative, similar to *o*-NAzB, AzTNB and AzPNB. The three azides are not equally activated in TAzTNB, finding that N_D-N_E has the lowest activation barrier (pathway 2, E_a = +30.62 kcal/mol) when compared to N_A-N_B and N_G-N_H (pathway 1, E_a = +32.22 kcal/mol; pathway 3, +32.69 kcal/mol, respectively). Our activation energies for TAzTNB are in agreement with previous experimental results (E_a = +26.0 kcal/mol).[67] TAzTNB-1 releases N_2 by cyclizing

with the *ortho* nitro group (E_a = +30.34 kcal/mol, **Figure 17a**) and has a barrier comparable to that of the N_D-N_E bond break in TAzTNB (pathway 2, E_a = +30.62 kcal/mol, **Figure 16**). TAzTNB-2 has two potential pathways for N_2 release, one with an azide in the plane with the ring (pathway 1, N_D-N_e) and another with an azide out of the plane with the ring (pathway 2, N_A-N_B). The activation energies indicate that releasing N_2 from N_D-N_e bond breaking is more favorable than releasing N_2 from N_A-N_B bond breaking in TAzTNB-2 (E_a = +32.73 kcal/mol and +36.21 kcal/mol, respectively, **Figure 17b**), in agreement with AzTNB (E_a = +28.05 kcal/mol).
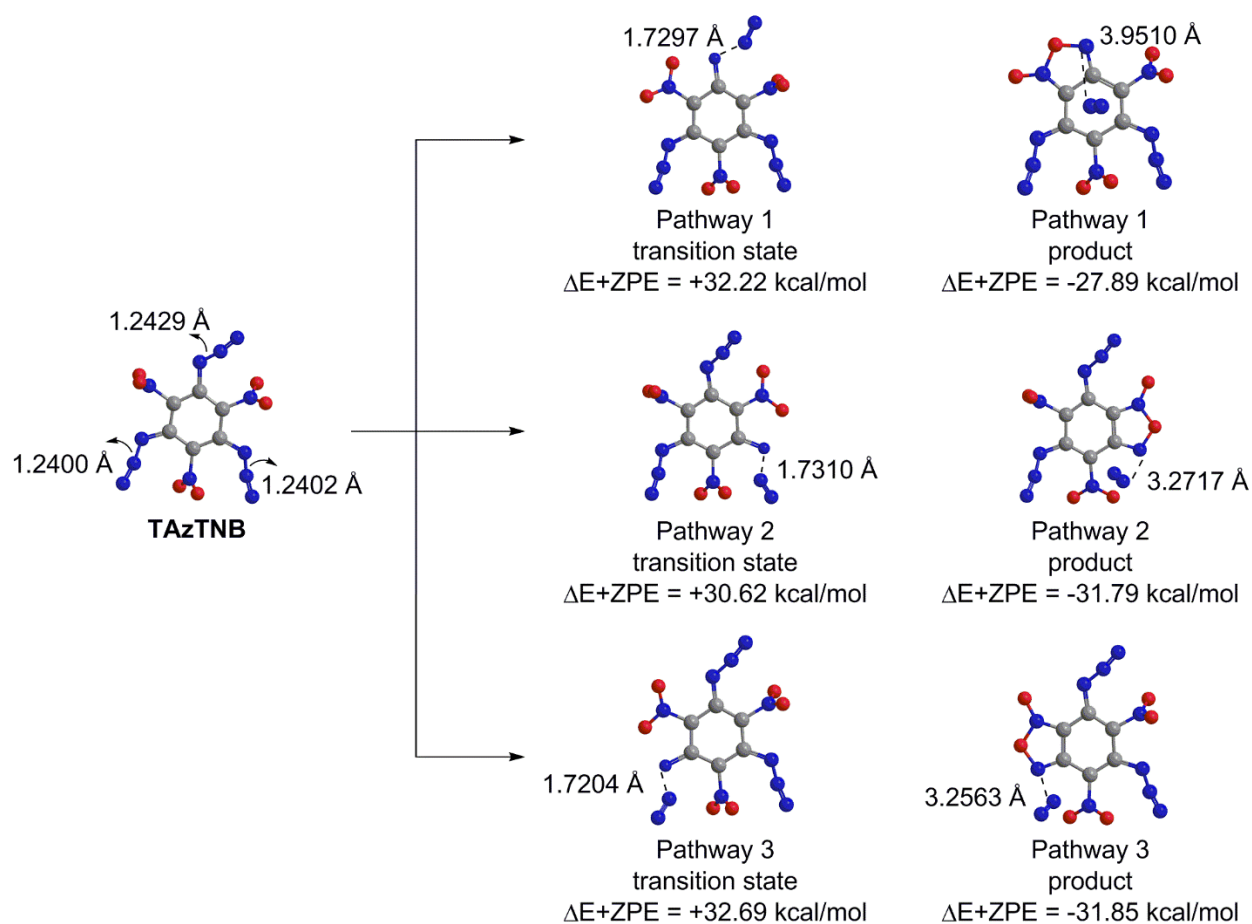
Figure 16. DFT(M06-2X)/TZVP optimized structures of TAzTNB for N_2 release on the singlet surface.
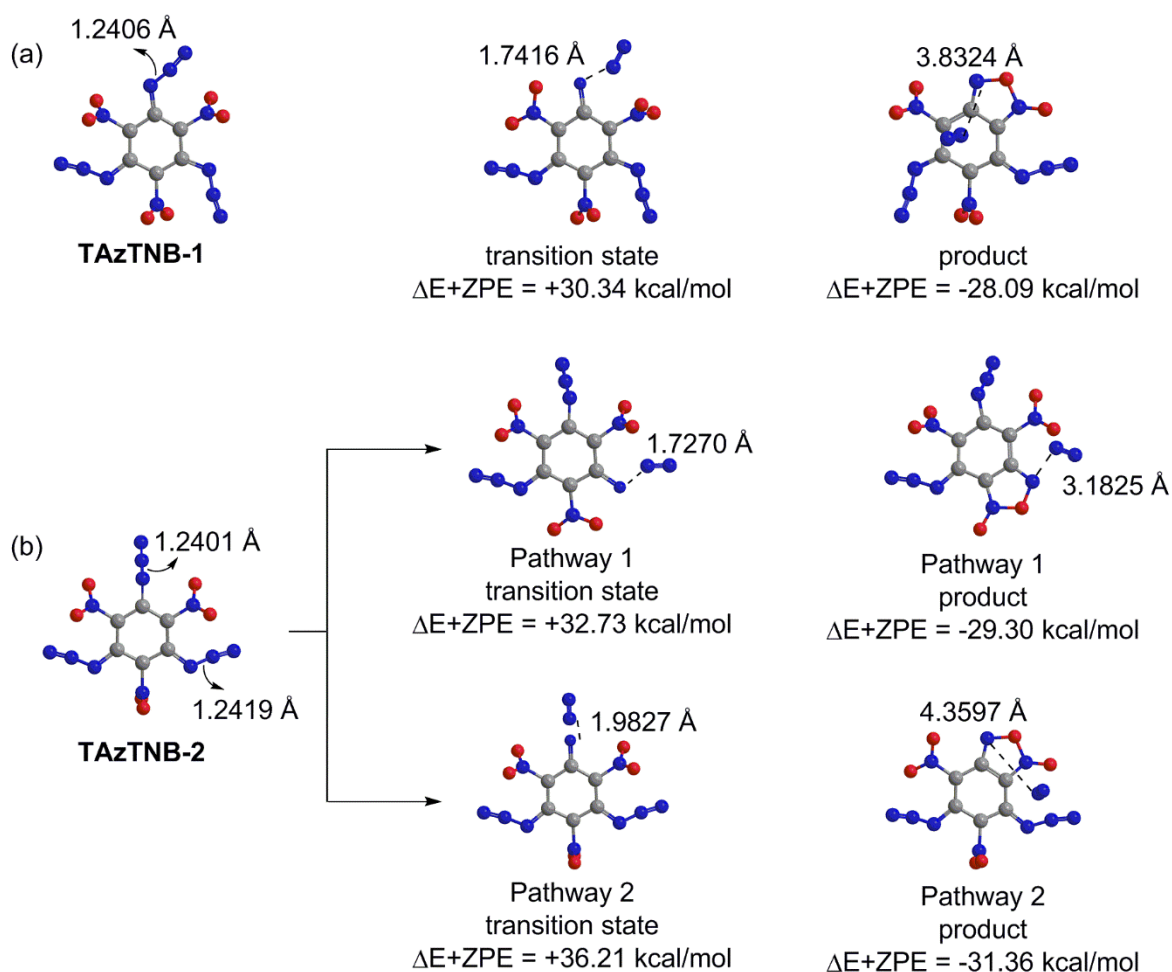
Figure 17. DFT(M06-2X)/TZVP optimized structures on the singlet surface for N_2 extrusion for conformations (a) TAzTNB-1 and (b) TAzTNB-2.

Wiberg Bond Index Analysis of Trigger Bonds

WBIs were calculated from the DFT(M06-2X)/TZVP optimized geometries for the $C-NO_2$ and $N-N_2$ bonds and compared to the corresponding reference molecule (**Table 3**) to identify the most activated (i.e., trigger) bonds. In AzB, the dihedral angle of the azide group influences the strength of the $N-N_2$ bond. As the dihedral angle increases from planar (0°) to perpendicular with the ring (90°), the $N-N_2$ bond becomes deactivated (WBI (%ΔWBIs) = 1.4627 (0.00%) and 1.4745 (+0.80%), respectively, **Figure 18**) due to resonance disruption between the aromatic π-system

and the azide group. The orbitals of the azide no longer overlap with those in the ring as the twist of the azide increases (i.e., closer to 90°), forcing an increase in double bond character on the N-N_2 bond in the azide (**Figure 19**). As such, over- and under-prediction of the sensitivity can be attributed to the change in the twist between the gas-phase and the condensed-phase. The azide and nitro bonds in *m*-NAzB (%ΔWBIs = -1.12% and -0.43%, respectively) are both activated relative to the bonds in AzB and NB. However, the azide is activated while the nitro is deactivated in *p*-NAzB (%ΔWBIs = -1.72% and +1.17%, respectively), attributed to the fact that electron-withdrawing groups decrease electron density through resonance in the *ortho* and *para* positions. Furthermore, the azide in *o*-NAzB is activated (%ΔWBIs = -1.55%), suggesting that steric and electronic effects between the azide and the nitro contribute to activation since the nitro group is twisted which allows the azide to be in the plane of the ring. Additionally, the terminal N-N bond in the azide is strengthened , as represented by more positive %ΔWBIs (**Table 3**), due to an increase in triple bond character, which confirms experimental data[67] that finds N_2 extrusion more favorable than NO_2 homolysis.
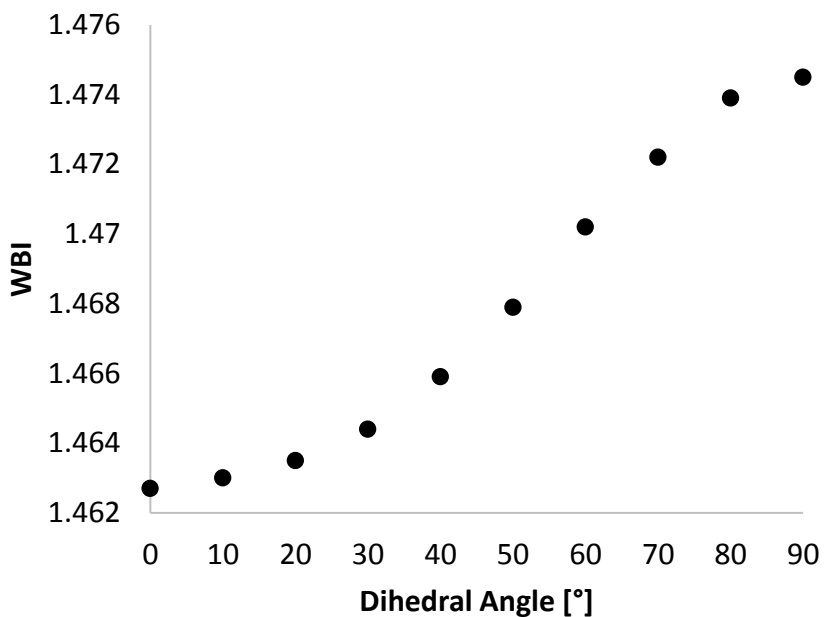
Figure 18. N-N$_2$ bond deactivation represented by increasing WBIs at larger dihedral angles in AzB.
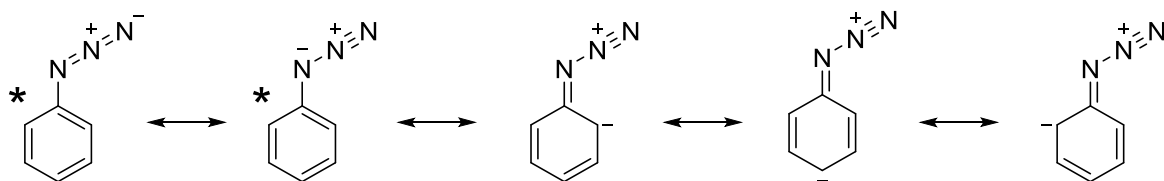
Figure 19. Resonance of AzB showing strengthening of the C-N bond to the aromatic ring and the terminal N-N bond of the azide when the azide is in the plane of the ring. The * indicates the resonance structures available when the azide is out of the plane of the ring.

The HEDMs are predicted to become more sensitive (i.e., more negative %ΔWBIs) with an increasing number of nitro groups as in the series AzTNB < AzPNB (%ΔWBIs = -5.30% and -6.50%, respectively), similar to our previous study.[49] A greater nitro twist allows the azide to be in the plane of the ring, which increases the activation of the $N-N_2$ bond. If the nitro groups are more in plane with the ring, then the azide group will be deactivated because it will be more perpendicular to the ring. AzTNB has the azide in the plane of the ring and is more activated than the nitro (%ΔWBIs = -5.30% and -1.57%, respectively). The additional electron-withdrawing nitro groups in AzPNB increase repulsion and thereby induces greater dihedral angles of the nitro groups. Therefore, the azide is more activated than the nitro from being in plane with the ring (%ΔWBIs = -6.50% and -3.31%, respectively) due to electronic effects, in agreement with previous work.[67] The azides are also more activated than the nitros in TAzTNB, TAzTNB-1 and TAzTNB-2, in agreement with AzTNB and AzPNB (**Table 3**). Conformation TAzTNB-1 is slightly more stable than TAzTNB but contains slightly less activated azides (%ΔWBIs = -5.42% and -5.48%, respectively). The decrease in activation could be attributed to a decrease in repulsion from the slightly greater symmetry in TAzTNB-1 which leads to each azide interacting with only one nitro. The two electrostatic interactions between C_C-NO_2 with N_A and N_G and the steric interaction of C_A-NO_2 with N_D could contribute to the greater azide activation in TAzTNB. Additionally, conformation TAzTNB-2 is more stable than TAzTNB and conformation TAzTNB-1, but it contains less activated trigger bonds (%ΔWBIs = -5.43%), which could be due to the azide twisted out of the plane with the ring thereby reducing the interaction with the *ortho* nitro group.

The greater activation of the azides compared to the nitros, represented by more negative %ΔWBIs, indicates that the trigger bond is located in the azide. The activation energies indicate N_2 extrusion in AzTNB and AzPNB (E_a = +28.05 kcal/mol and +31.91 kcal/mol, respectively)

rather than nitro homolysis (E_a = +68.2 kcal/mol),[67] in agreement with our %ΔWBIs finding the azide more activated than the nitro (%ΔWBIs = -5.30% and -1.57%, (AzTNB); -6.50% and -3.31% (AzPNB), respectively). For TAzTNB, the three azides are not equally activated according to the %ΔWBIs (**Table 3**) since each have a different dihedral angle with respect to the ring as well as a different number of interactions with adjacent nitro groups. The %ΔWBIs indicate that N_A-N_B is more activated than N_D-N_E and N_G-N_H in TAzTNB (%ΔWBIs = -5.48%, -5.04% and -4.92%, respectively) which is in slight disagreement with the barriers for our activation barriers (E_a = +32.22 kcal/mol, +30.62 kcal/mol, and +32.69 kcal/mol, respectively) which find N_D-N_E to be most activated. Our results agree that N_G-N_H is the least activated of the three azide bonds; however, the disagreement between N_A-N_B and N_D-N_E for our %ΔWBIs and activation barriers could be attributed to crystal packing effects.

Conclusions

Trigger bonds were assigned for AzTNB, AzPNB and TAzTNB and conformations by comparing their WBIs to those in reference molecules NB and AzB for a relative measure of activations of the C-NO_2 and N-N_2 bonds. Trigger bonds with lower electron densities than the reference molecules are indicated by a more negative %ΔWBIs and are therefore more susceptible to bond breakage under stress. The N-N_2 bonds, which were more activated than the C-NO_2 bonds, became more activated as the number of azide groups increased. Greater twists in the nitro group with respect to the ring (i.e., closer to 90°) induce more negative %ΔWBIs; however, greater twists in the azide group with respect to the ring (i.e., closer to 90°) lead to more positive %ΔWBIs due to an increase in double bond character. Based on the analysis, all nitro and azide groups within a molecule are not necessarily equally activated to contribute to explosive decomposition initiation.

Secondary effects are not considered through gas-phase calculations and may need to be modeled in the condensed-phase. Overall, %ΔWBIs can assign trigger bonds to help rationalize the sensitivities of azide groups compared to nitro groups.

The activation barriers for the simple aromatic azides indicate that without an adjacent nitro group (i.e., AzB, *m*-NAzB, *p*-NAzB), the azide extrudes N_2 through the triplet state as indicated by the triplet nitrene being lower in energy than the closed-shell and open-shell nitrenes (ΔE+ZPE = +45.56 kcal/mol and +11.54 kcal/mol, respectively). However, the adjacent nitro group in *o*-NAzB forces the release of N_2 in the singlet state to cyclization forming benzofuroxan. AzTNB, AzPNB, and TAzTNB undergo cyclization with the *ortho* nitro group, in agreement with our results for *o*-NAzB, andthe benzofuroxan derivative is produced when the azide is in the plane of the ring. The most favorable cyclization pathway for TAzTNB is for N_D-N_E (E_a = +30.62 kcal/mol), which disagrees with our %ΔWBIs likely due to crystal packing effects. Overall, %ΔWBIs and activation barriers can help understand the varying sensitivities of azide trigger bonds in aromatic azide-based energetic materials.

CHAPTER 4

TRIGGER BOND ANALYSIS OF EXPLOSOPHORE SENSITIVITY IN AZOLE-BASED

HIGH ENERGY DENSITY MATERIALS USING WIBERG BOND INDICES

Introduction

Improving performance, sensitivity and energy release are important for the development of high energy density materials (HEDMs) for advanced weapons systems.[1] In aeronautics,[4] propellants with exceptional energetic properties are essential to replace hazardous materials, such as hydrazine, to reduce pollution.[1-4] However, in order to replace conventional energetic materials with novel HEDMs, understanding how and why explosive decomposition occurs is necessary. Since detonation is practically instantaneous, mechanisms of energetic reactions present obstacles that experimental analysis must overcome.[14] Thus, models of explosive decomposition have relied upon information from molecular dynamics and density functional theory (DFT) to predict energetic properties from measures of bond activation and mechanisms of detonation.[1, 14, 15]

Explosophores[5] such as nitro ($-NO_2$)[52-56] and azide ($-N_3$)[11] functional groups form trigger bonds in HEDMs, activated bonds that break to initiate explosive decomposition.[16] Explosive decomposition proposed based on mass spectrometry[57-61] and DFT[62-66] for conventional energetic materials generally assigns initiation through homolytic bond cleavage, molecular rearrangements, eliminations, or ring fission. Theoretical measures of initiation include the Atoms-In-Molecules (AIM) method,[77, 78] unimolecular decomposition activation barriers,[62, 63] and bond dissociation energies (BDEs).[79] Our group has shown that the Wiberg bond index (WBI), a measure of interatomic electron density measured as the sum of the squares of the off-diagonal elements of the density matrix (Equation 24),[81] is an inexpensive method for assigning trigger bonds.[16, 49]

$$\text{WBI}_{\text{AB}} = \sum_{p \in A} \sum_{q \in B} \left(D_{pq}\right)^2 \tag{24}$$

Identifying trigger bonds in novel HEDMs through WBIs can guide mechanistic studies and predictions of energetic properties, like impact sensitivity.

The activation of trigger bonds in energetic materials will be influenced by steric effects, electron-withdrawing groups and ring strain.[16, 49] Activated HEDM trigger bonds are expected to be longer and have lower electron density relative to reference molecules (i.e., contain the same bond type, hybridization and explosophore). A relative scale for trigger bond activation can be determined by comparing the WBIs (%ΔWBI) (Equation 25).[16, 49]

$$\%\Delta\text{WBI}_{\text{AB}} = \frac{\text{WBI}_{\text{AB}}^{\text{HEDM}} - \text{WBI}_{\text{AB}}^{\text{reference}}}{\text{WBI}_{\text{AB}}^{\text{reference}}} \times 100 \tag{25}$$

The most negative %ΔWBI specifies the activated trigger bond expected to break to initiate explosive decomposition. For example, o-C-NO$_2$ and p-C-NO$_2$ bonds in picric acid (PA) were compared to the C(sp^2)-NO$_2$ bond in reference molecule nitrobenzene (NB) (**Figure 20**).[49] The trigger bond is assigned as the more activated o-C-NO$_2$ bond involved in repulsion from the lone pair on the oxygen of the –OH group.[49] The other o-C-NO$_2$ bond is deactivated due to the unidirectional hydrogen bond with the hydroxyl group.[49] Our previous studies determined that %ΔWBIs correlate with experimental impact sensitivity within conventional energetic materials[16, 49] and could be used to understand how intramolecular interactions influence the sensitivity.
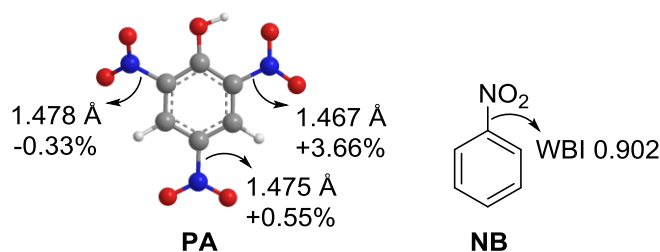
Figure 20. Example of %ΔWBI analysis of PA and reference molecule NB.

Conventional energetic materials have been extensively studied and thus results have been reproduced for experimental impact sensitivity across the literature. Since few novel HEDMs have been applied to real-world systems, the experimental studies on impact sensitivity are less reliable. Often, the results have not been reproduced or contain large variation between studies and methods.[11, 208, 209] Therefore, this study will focus on using %ΔWBIs to rationalize how different explosophores (i.e., C-NO_2, N-NO_2 and N-N_2) might influence the sensitivity of a set of 35 novel, azole-based HEDMs (**Table 4**). Based on activation energies of azide trigger bonds in simple azides and aromatic azide-based energetic materials as shown in the previous chapter, azide trigger bonds should be more activated than C-NO_2 trigger bonds. The results provide support that %ΔWBIs can be used to determine how intramolecular steric and substituent effects affect the sensitivity of the trigger bond.

Table 4. The 35 azole-based HEDMs included in this study.
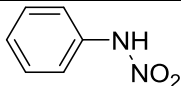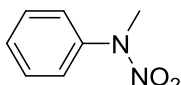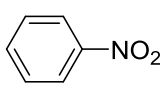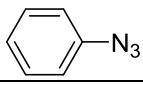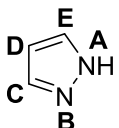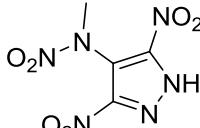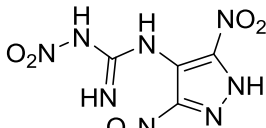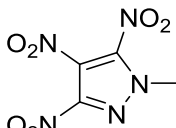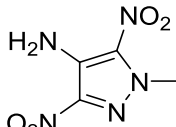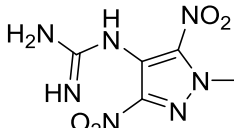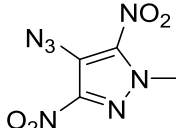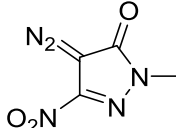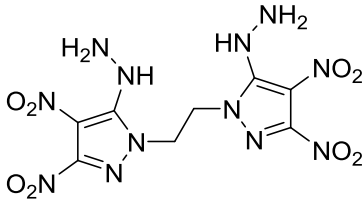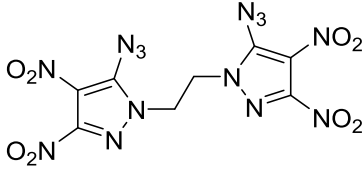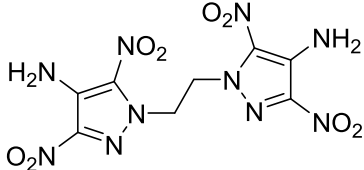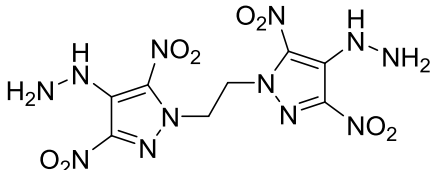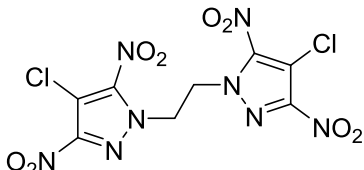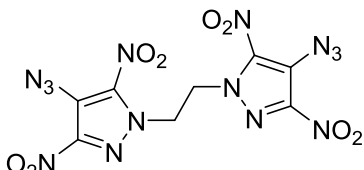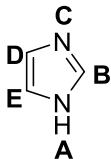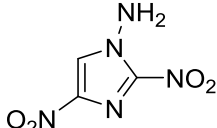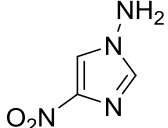
HEDM	Chemical Name	Chemical Structure
Reference		
NAB	Nitraminobenzene	
MNAB	methylnitraminobenzene	
NB	nitrobenzene	
AzB	azidobenzene	
Pyrazoles		
1	4-(*N*-methylnitramino)-3,5-dinitropyrazole	
2	1-(3,5-dinitropyrazol-4-yl)-3-nitroguanidine	
3	*N*-methyl-3,4,5-trinitropyrazole	
4	*N*-methyl-4-amino-3,5-dinitropyrazole	
5	4-guanidino-3,5-dinitropyrazole	
6	*N*-methyl-4-azido-3,5-dinitropyrazole	
7	*N*-methyl-3-nitro-4-diazo-5-oxide pyrazole	

Table 4 (continued)

HEDM	Chemical Name	Chemical Structure
8	1-amino-4-nitropyrazole	
9	1-amino-3,5-dinitropyrazole	
10	1-amino-3,4-dinitropyrazole	
11	1,5-diamino-3,4-dinitropyrazole	
12	1-amino-3,4-dinitro-5-cyanopyrazole	
13	1-amino-3,4-dinitro-5-azidopyrazole	
14	1,4-diamino-3,5-dinitropyrazole	
15	*N*-amino-4-(*N*-methylnitramino)-3,5-dinitropyrazole	
16	1,2-bis(3,4,5-trinitro-1*H*-pyrazol-1-yl)ethane	
17	1,1'-(ethane-1,2-diyl)bis(3,4-dinitro-1*H*-pyrazol-5-amine)	

Table 4 (continued)

HEDM	Chemical Name	Chemical Structure
18	*N,N'*-[1,1'-(ethane-1,2-diyl)bis(3,4-dinitro-1*H*-pyrazole-5,1-diyl)]dinitramide	
19	1,1'-(ethane-1,2-diyl)bis(3,4-dinitro-1*H*-pyrazol-5-azide)	
20	1,1'-(ethane-1,2-diyl)bis(3,5-dinitro-1*H*-pyrazol-4-amine)	
21	*N,N'*-[1,1'-(ethane-1,2-diyl)bis(3,5-dinitro-1*H*-pyrazole-4,1-diyl)]dinitramide	
22	1,2-bis(4-chloro-3,5-dinitro-1*H*-pyrazol-1-yl)ethane	
23	1,1'-bis(4-azido-3,5-dinitro-1*H*-pyrazol-1-yl)ethane	
Imidazoles		
24	1-amino-2,4-dinitroimidazole	
25	1-amino-4-nitroimidazole	

Table 4 (continued)

HEDM	Chemical Name	Chemical Structure
26	1-amino-4,5-dinitroimidazole	
27	1-amino-4-nitro-5-azidoimidazole	
Triazoles		
28	4-nitramino-5-nitro-2*H*-1,2,3-triazole	
29	4-nitro-5-azido-2*H*-1,2,3-triazole	
30	2-amino-4,5-dinitro-1,2,3-triazole	
31	2-amino-4-nitro-5-azido-1,2,3-triazole	
32	2-methyl-4,5-dinitro-1,2,3-triazole	
33	2-methyl-4-amino-5-nitro-1,2,3-triazole	
34	2-methyl-4-nitramino-5-nitro-1,2,3-triazole	
35	2-methyl-4-nitro-5-azido-1,2,3-triazole	

Computational Methods

DFT-optimized geometries of the 35 azole-based HEDMs were calculated using Gaussian 09[46] and the hybrid functional M06-2X[35] with a triple-ζ basis set (TZVP),[48] as in our previous study.[49] All structures were characterized as minima on the potential energy surface through vibrational analysis. WBIs for each potential trigger bond (i.e., $C-NO_2$, $N-NO_2$, and $N-N_2$) were calculated using Natural Bond Orbital (NBO) version 3.1.[50, 51] %ΔWBIs were determined from reference molecules nitraminobenzene (NAB), methylnitraminobenzene (MNAB), nitrobenzene (NB), and azidobenzene (AzB) which contain the same bond type, hybridization and explosophore as the HEDMs. Our previous study found basis set dependence for the WBIs;[49] therefore, the results were obtained using TZVP.

Results and Discussion

The DFT(M06-2X)/TZVP optimized structures of the 35 azole-based energetic materials are in good agreement with available X-ray crystallographic data[210-214] (**Table 5**). Generally, the DFT-optimized $C-NO_2$ and $N-NO_2$ bond distances are slightly longer than experimental values while the $N-N_2$ bond distances are shorter (**Table 5**).[210-214] Furthermore, intramolecular NH⋯ONO hydrogen bonding interactions are shorter than those found in experiment.[211, 212] Intramolecular interactions between the nitro and amino groups induce near-planar conformations for the azole-based HEDMs. Hydrogen bonding interactions as well as steric effects between functional groups influence the strength of the potential $C-NO_2$ trigger bonds, specifically. Steric effects between functional groups affect the activation of the $N-NO_2$ and $N-N_2$ trigger bonds. The azole-based energetic materials were grouped according to ring type (i.e., pyrazoles, imidazoles and triazoles) and compared by functional groups.

Table 5. Comparison of experimental and DFT(M06-2X)/TZVP bond distances [Å] and WBIs for C-NO$_2$, N-NO$_2$ and N-N$_2$ bonds of the azole-based HEDMs[210-214] with the corresponding experimental impact sensitivity (I.S.) [cm] and reference molecules.[71, 150, 215, 216]

Compound	Bond	d_{DFT} [Å]	d_{exp} [Å]	WBI	%ΔWBI [%]	I.S. [J]
References						
NAB	N-NO$_2$	1.387	-	1.0088	0	-
MNAB	N-NO$_2$	1.384	-	1.0182	+0.93	-
NB	C-NO$_2$	1.481	1.464^b	0.9022	0	100[71] [cm]
AzB	N-N$_2$	1.228	-	1.4627	0	-
Pyrazoles						
1	C$_C$-NO$_2$	1.458	-	0.9044	+0.24	
	C$_E$-NO$_2$	1.442	-	0.9364	+3.79	17[211]
	N$_D$-NO$_2$	1.397	-	0.9775	-4.00	
2	C$_C$-NO$_2$	1.454	-	0.9208	+2.06	
	C$_E$-NO$_2$	1.427	-	0.9638	+6.83	10[211]
	N$_D$-NO$_2$	1.385	-	1.0085	-0.03	
3	C$_C$-NO$_2$	1.458	-	0.9057	+0.39	
	C$_D$-NO$_2$	1.467	-	0.8876	-1.62	>40[211]
	C$_E$-NO$_2$	1.446	-	0.9319	+3.29	
4	C$_C$-NO$_2$	1.436	-	0.9508	+5.39	>40[211]
	C$_E$-NO$_2$	1.411	-	1.0102	+11.97	
5	C$_C$-NO$_2$	1.456	-	0.9095	+0.81	>40[211]
	C$_E$-NO$_2$	1.421	-	0.9778	+8.38	
6	C$_C$-NO$_2$	1.449	-	0.9246	+2.48	
	C$_E$-NO$_2$	1.439	-	0.9524	+5.56	14[211]
	N$_D$-N$_2$	1.241	-	1.3931	-4.76	
7	C$_C$-NO$_2$	1.451	1.430	0.9124	+1.13	22[211]
8	C$_D$-NO$_2$	1.435	-	0.9567	+6.04	>40[212]
9	C$_E$-NO$_2$	1.439	-	0.9438	+4.61	>40[212]
	C$_C$-NO$_2$	1.455	-	0.9128	+1.17	
10	C$_C$-NO$_2$	1.466	-	0.8839	-2.03	>40[212]
	C$_D$-NO$_2$	1.442	-	0.9433	+4.56	
11	C$_C$-NO$_2$	1.467	1.448	0.8804	-2.42	>40[212]
	C$_D$-NO$_2$	1.416	1.402	0.9988	+10.71	
12	C$_C$-NO$_2$	1.466	-	0.8871	-1.67	>40[212]
	C$_D$-NO$_2$	1.448	-	0.9297	+3.05	
13	C$_C$-NO$_2$	1.468	-	0.8804	-2.42	
	C$_D$-NO$_2$	1.429	-	0.9690	+7.40	1.5[212]
	N$_E$-N$_2$	1.245	-	1.3709	-6.28	
14	C$_E$-NO$_2$	1.408	1.398	1.0165	+12.67	>40[211]
	C$_C$-NO$_2$	1.429	1.406	0.9650	+6.96	
15	C$_C$-NO$_2$	1.453	-	0.9145	+1.36	
	C$_E$-NO$_2$	1.439	-	0.9394	+4.12	18[211]
	N$_D$-NO$_2$	1.400	-	0.9727	-4.47	
16	C$_{C/C'}$-NO$_2$	1.462	1.441	0.8987	-0.39	
	C$_{D/D'}$-NO$_2$	1.465	1.450	0.8931	-1.01	25[213]
	C$_{E/E'}$-NO$_2$	1.450	1.433	0.9237	+2.38	
17	C$_{C/C'}$-NO$_2$	1.465	-	0.8824	-2.19	>40[213]
	C$_{D/D'}$-NO$_2$	1.424	-	0.9812	+8.76	

Table 5 (continued)

Compound	Bond	d_{DFT} [Å]	d_{exp} [Å]	WBI	%ΔWBI [%]	I.S. [J]
18	C_C-NO_2	1.468	-	0.8810	-2.35	
	C_D-NO_2	1.439	-	0.9520	+5.52	
	N_E-NO_2	1.426	-	0.9307	-7.74	6^{213}
	$C_{C'}$-NO_2	1.465	-	0.8894	-1.42	
	$C_{D'}$-NO_2	1.439	-	0.9469	+4.95	
	$N_{E'}$-NO_2	1.424	-	0.9319	-7.62	
19	$C_{C/C'}$-NO_2	1.467	1.460	0.8822	-2.22	
	$C_{D/D'}$-NO_2	1.430	1.422	0.9663	+7.10	4^{213}
	$N_{E/E'}$-N_2	1.248	1.255	1.3585	-7.12	
20	$C_{C/C'}$-NO_2	1.439	-	0.9436	+4.59	$>40^{213}$
	$C_{E/E'}$-NO_2	1.411	-	1.0110	+12.06	
21	C_C-NO_2	1.453	-	0.9172	+1.66	
	N_D-NO_2	1.407	-	0.9608	-4.76	
	C_E-NO_2	1.448	-	0.9276	+2.82	7^{213}
	$C_{C'}$-NO_2	1.461	-	0.8985	-0.41	
	$N_{D'}$-NO_2	1.407	-	0.9566	-5.17	
	$C_{E'}$-NO_2	1.435	-	0.9589	+6.28	
22	$C_{C/C'}$-NO_2	1.462	-	0.9055	+0.37	$>40^{213}$
	$C_{E/E'}$-NO_2	1.446	-	0.9350	+3.64	
23	$C_{C/C'}$-NO_2	1.451	-	0.9197	+1.94	
	$N_{D/D'}$-N_2	1.241	-	1.3910	-4.90	3^{213}
	$C_{E/E'}$-NO_2	1.441	-	0.9462	+4.88	
Imidazoles						
24	C_B-NO_2	1.456	-	0.9052	+0.33	$>40^{214}$
	C_D-NO_2	1.454	-	0.9119	+1.08	
25	C_E-NO_2	1.452	-	0.9166	+1.60	$>40^{214}$
26	C_E-NO_2	1.439	-	0.9398	+4.17	$>40^{214}$
	C_D-NO_2	1.463	-	0.8909	-1.25	
27	C_E-NO_2	1.435	-	0.9466	+4.92	3.5^{214}
	N_D-N_2	1.242	-	1.3824	-5.49	
Triazoles						
28	C_E-NO_2	1.445	1.421	0.9279	+2.85	3.5^{210}
	N_D-NO_2	1.407	1.347	0.9590	-4.94	
29	C_E-NO_2	1.444	-	0.9298	+3.06	4^{210}
	N_D-N_2	1.240	-	1.4043	-3.99	
30	C_D-NO_2	1.459	1.442	0.8973	-0.54	24^{210}
	C_E-NO_2	1.459	1.451	0.8989	-0.37	
31	C_E-NO_2	1.448	-	0.9253	+2.56	3^{210}
	N_D-N_2	1.242	-	1.4003	-4.27	
32	C_D-NO_2	1.458	-	0.9005	-0.19	35^{210}
	C_E-NO_2	1.458	-	0.9008	-0.16	
33	C_E-NO_2	1.429	-	0.9613	+6.55	$>40^{210}$
34	C_E-NO_2	1.442	-	0.9341	+3.54	25^{210}
	N_D-NO_2	1.406	-	0.9630	-4.54	
35	C_E-NO_2	1.445	-	0.9365	+3.06	8^{210}
	N_D-N_2	1.241	-	1.4067	-4.00	

[a]MNA is documented as 1.317 Å in the cif and 1.318 Å in the paper by Kettner et al.[215]
[b]NB is documented as 1.464 Å in the cif and 1.467 Å in the paper by Boese et al.[150]

Wiberg Bond Index Analysis of Trigger Bonds

WBIs were calculated from the DFT(M06-2X)/TZVP optimized geometries for the $C-NO_2$, $N-NO_2$ and $N-N_2$ trigger bonds of the 35 novel azole-based energetic materials and compared to the corresponding bond in reference molecules with the same bond type, hybridization and explosophore (**Table 5**). The HEDMs should become more sensitive (i.e., more negative %ΔWBIs) with an increasing number of $C-NO_2$ groups as in the series **5** > **1** (%ΔWBIs = +0.81% and -4.00%, respectively), **5** > **2** (%ΔWBIs = +0.81% and -0.03%, respectively), **20** > **16** (%ΔWBIs = +4.59% and -1.01%, respectively), **22** > **16** (%ΔWBIs = +0.37% and -1.01%, respectively) and **33** > **32** (%ΔWBIs = +6.55% and -0.19%, respectively), consistent with experimental impact sensitivity data. %ΔWBIs indicate the same trend for HEDMs with a lower limit for experimental impact sensitivity (i.e., >40 J), as in the series **8** > **9** (%ΔWBIs = +6.04% and +1.17%, respectively), **8** > **10** (%ΔWBIs = +6.04% and -2.03%, respectively), **4** > **3** (%ΔWBIs = +5.39% and -1.62%, respectively), **25** > **26** (%ΔWBIs = +1.60% and -1.25%, respectively) and **25** > **24** (%ΔWBIs = +1.60% and +0.33%, respectively).

Similarly to our previous study,[49] under-prediction of the sensitivity (i.e., more positive %ΔWBIs than expected) based on %ΔWBIs in the series **16** > **17** (%ΔWBIs = -1.01% (I.S. = 25 J) and -2.19% (I.S. = >40 J), respectively) could be attributed to the differences in the dihedral angles of the nitro group with respect to the ring in the gas-phase versus the condensed-phase (**Table 6**). As the twist of the nitro group increases from planar (0°) to perpendicular with the ring (90°) in NB, the trigger bond becomes more activated from reduced aromatic π-system conjugation.[49] When the dihedral angles are constrained to the values in the X-ray crystal structure of **16** (**Table 6**), the %ΔWBI shifts to -1.60%; however, the series remains inconsistent. Furthermore, %ΔWBI over-prediction of the sensitivity (i.e., more negative %ΔWBIs than

expected) for **17** could be attributed to the differences in the dihedral angles between the phases; however, experimental X-ray crystallographic evidence is needed for validation. Finding shifts in the %ΔWBIs based on constraining the dihedral angles to those in the X-ray crystal structures which lead to over- and under-prediction is consistent with our previous study.[49] Additionally, under- and over-prediction of sensitivity of the azide group could be attributed to differences in the dihedral angles with respect to the ring in the gas-phase versus the condensed-phase (**Table 6**). As shown in our study on simple azides and aromatic azide-based energetic materials in the previous chapter, when the twist of the azide group increases from planar (0°) to perpendicular with the ring (90°) in AzB, the N-N_2 trigger bond becomes deactivated (WBI (%ΔWBIs) = 1.4627 (0.00%) and 1.4745 (+0.80%), respectively) likely from resonance disruption between the aromatic ring system and the azide group.

Table 6. Comparison of available experimental and DFT(M06-2X)/TZVP dihedral angles [°] for C-NO_2, N-NO_2 and N-N_2 bonds of the azole-based HEDMs[210-214] and reference molecules.[150]

HEDM	Bond	φ_{DFT} [°]	φ_{exp} [°]
Reference			
NB	C-NO_2	0.0	1.7
Pyrazoles			
7	C_C-NO_2	0.0	2.6
11	C_C-NO_2	-49.7	-39.8
	C_D-NO_2	-3.2	-8.3
14	C_E-NO_2	3.2	3.7
	C_C-NO_2	-0.1	0.1
	C_C-NO_2	-19.2	-15.1
	$C_{C'}$-NO_2	+19.2	15.2
16	C_D-NO_2	-65.0	-76.8
	$C_{D'}$-NO_2	64.6	76.4
	$C_{E/E'}$-NO_2	±22.2	±14.5
	C_C-NO_2	-51.5	-55.4
19	$C_{C'}$-NO_2	47.4	55.2
	$C_{D/D'}$-NO_2	±5.3	±4.8
	$N_{E/E'}$-N_2	±31.1	±43.6
Triazoles			
28	C_E-NO_2	-8.7	6.1
30	C_D-NO_2	-37.0	-31.6
	C_E-NO_2	-36.1	-29.5

Intramolecular hydrogen bonding strengthens and deactivates C-NO$_2$ trigger bonds. HEDMs with these interactions would be expected to be less sensitive to explosive decomposition. Contributions from resonance structures with C=N double bond character induced by intramolecular hydrogen bonding favor nearly planar nitro groups with shortened C-NO$_2$ bond lengths which are deactivated toward explosive decomposition. Therefore, C-NO$_2$ bonds influenced by hydrogen bonding interactions will not break as easily relative to isolated C-NO$_2$ bonds. Within energetic materials that contain intramolecular hydrogen bonds, not all nitro groups form trigger bonds (**Figure 21**). For example, the C$_C$-NO$_2$ bond in **11** is activated by repulsion while the C$_D$-NO$_2$ bond is deactivated due to hydrogen bonding (%ΔWBIs = -2.42% and +10.71%, respectively). Furthermore, the C-NO$_2$ bonds in **14** are both deactivated due to –NH$_2$ hydrogen bonding interactions. The level of deactivation differs between the C-NO$_2$ bonds due to the number of hydrogen bonding interactions (i.e., one for C$_C$-NO$_2$ (%ΔWBI = +6.96%) and two for C$_E$-NO$_2$ (+12.67%)). The greater deactivation with an increasing number of hydrogen bonding interactions is due to an increase in double-bond character.
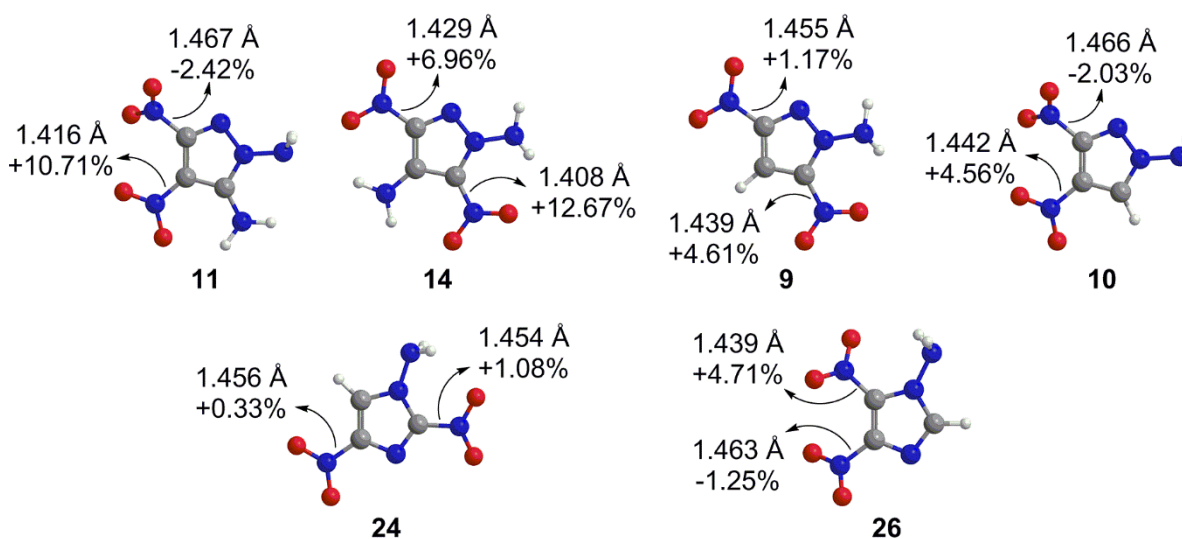
Figure 21. Select bond distances (Å) and %ΔWBIs (%) for trigger bonds in **11**, **14**, **9** and **10**.

The position of the nitro group on the ring influences the sensitivity. For example, **9** and **10** are isomers with two C-NO$_2$ bonds. However, both have a lower limit for experimental impact sensitivity (i.e., > 40 J). Based on %ΔWBIs, **10** would likely be more sensitive than **9** (%ΔWBIs = -2.03% and +1.17%, respectively, **Figure 21**) due to the increased repulsion in **10** from the adjacent nitro groups forcing the twist out of the plane of the ring. The intramolecular hydrogen bonding interaction of **9** likely stabilizes the C$_E$-NO$_2$ bond and a lack of repulsion will keep the C$_C$-NO$_2$ bond in the plane with the ring, thus keeping the bonds deactivated. Additionally, our %ΔWBIs suggest that **26** would be more sensitive than **24** (%ΔWBIs = -1.25% and +0.33%, respectively), but better tests on experimental impact sensitivity are required to confirm our results. In **26**, the increased repulsion of C$_D$-NO$_2$ from increased planarity of the C$_E$-NO$_2$ from the amino group hydrogen bond can account for the potential increase in sensitivity. In **24**, the C$_B$-NO$_2$ is hydrogen bonded with the –NH$_2$ group, while the C$_D$-NO$_2$ bond is coplanar with the ring.

Different combinations of explosophores, including C-NO$_2$, N-NO$_2$ and N-N$_2$, are found in novel azole-based HEDMs. When a C-NO$_2$ is substituted with a C-N$_3$ as in the series **3** > **6** (%ΔWBIs = -1.62% and -4.76%, respectively) and **30** > **31** (%ΔWBIs = -0.54% and -4.27%, respectively), the %ΔWBIs indicate that the azide functional group is more sensitized than a nitro group bonded to an sp^2 carbon (**Figure 22**), in agreement with experimental impact sensitivity values (**Table 5**). The adjacent C-NO$_2$ functional groups remain planar with the ring, thus deactivating the bonds. We also find that the N-NO$_2$ bond is also more activated than C-NO$_2$ (**Figure 23**), in agreement with measures of experimental impact sensitivity (**Table 5**), as in the series **16** < **18** (%ΔWBIs = -1.01% and -7.74%, respectively) and **32** < **34** (%ΔWBIs = -0.19% and -4.54%, respectively). However, based on %ΔWBIs the N-NO$_2$ bond is predicted to be more

activated than N-N₂, but molecules with N-NO₂ groups are less sensitive experimentally (**Table 5**) than the azides, as in **34** > **35** (%ΔWBIs = -4.54% and -4.00%, respectively, **Figure 24a**). This erroneous prediction by the %ΔWBI method could be attributed to secondary solid-state effects on the activation of the explosophores in the condensed phase as the correct order is predicted for some pairs of analogous molecules (i.e., **29** > **28** (%ΔWBIs = -3.99% and -4.94%, respectively, **Figure 24b**). Therefore, %ΔWBIs might not be able to accurately distinguish between sensitivities of these explosophore groups.
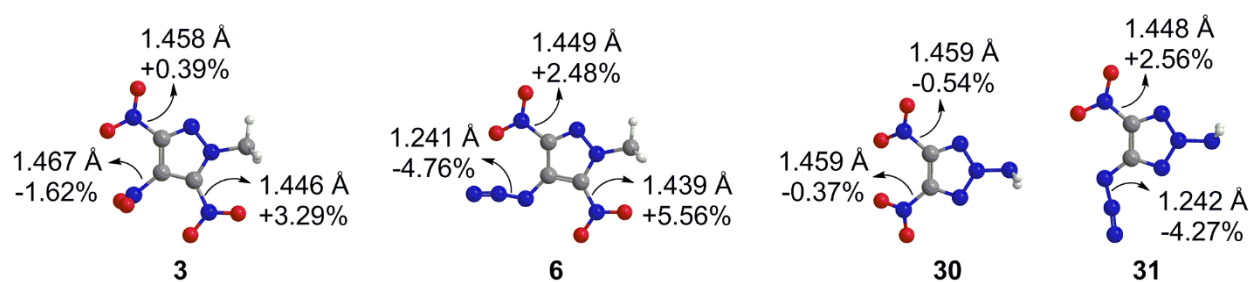
Figure 22. Select bond distances (Å) and %ΔWBIs (%) for trigger bonds in **3**, **6**, **30**, and **31**.
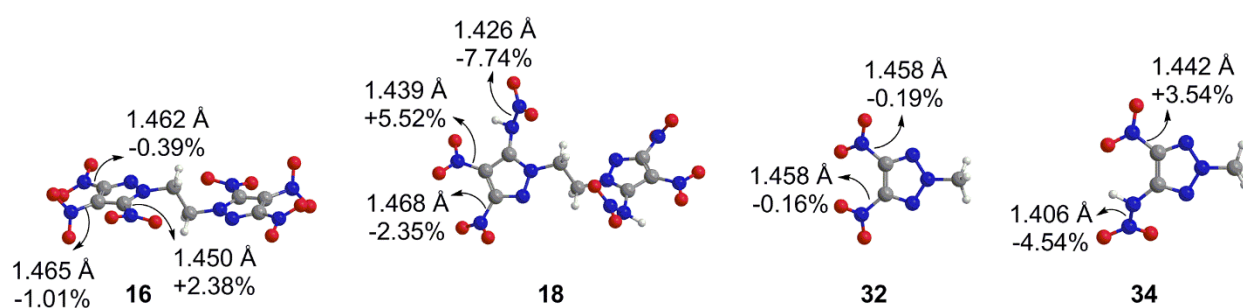
Figure 23. Select bond distances (Å) and %ΔWBIs (%) for trigger bonds in **16**, **18**, **32**, and **34**.
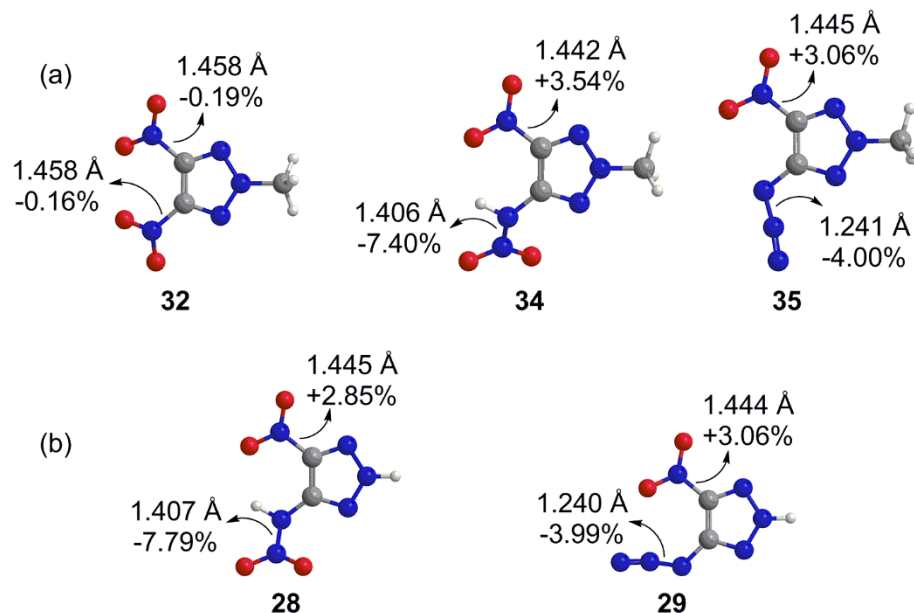
Figure 24. Select bond distances (Å) and %ΔWBIs (%) for trigger bonds in (a) **32**, **34** and **35**, and (b) **28** and **29**.

Substituting $-NH_2$ groups for $N-NO_2$ group increases the sensitivity of the azole-based HEDMs due to an additional nitro group. The %ΔWBIs indicate this trend (**Figure 25**), in agreement with experimental impact sensitivity (**Table 5**), as in the series **5** > **2** (%ΔWBIs = +0.81% and -0.03%) and **33** > **34** (%ΔWBIs = +6.55% and -4.54%). The lack of two hydrogen bonding interactions with the addition of an explosophore (i.e., nitro (-NO_2) group) forces an increase in the %ΔWBIs from greater twists of the nitro groups from repulsion. Additionally, planarity of the nitro group involved in the one hydrogen bonding interaction with the -NH- group induces a decrease in activation based on %ΔWBIs.
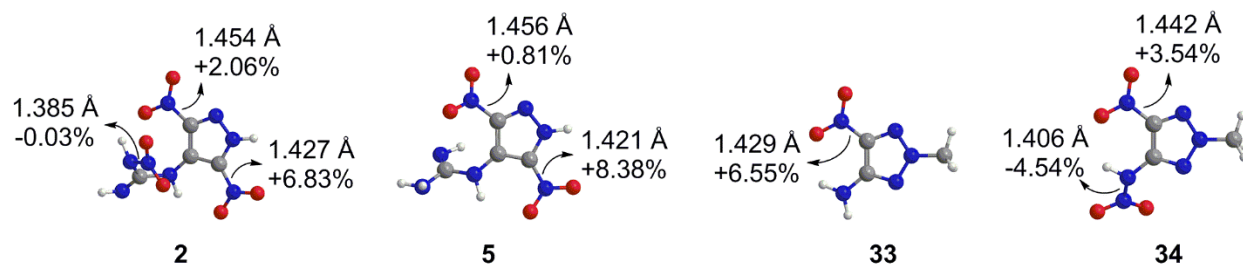
Figure 25. Select bond distances (Å) and %ΔWBIs (%) for trigger bonds in **5**, **2**, **33**, and **34**.

Some pyrazole-based HEDMs consist of two rings linked by an aliphatic backbone (i.e., **16-23**). The HEDMs become more sensitive with the second ring, which could be attributed to the additional explosophores, as in the series **6** > **23** (%ΔWBIs = -4.76% and -4.90%, respectively), in agreement with experimental impact sensitivity (**Table 5**). Within a series with a lower limit for experimental impact sensitivity **4** > **20** (%ΔWBIs = +5.39% and +4.59%, respectively), the same trend is observed. However, the trend does not agree with our %ΔWBIs for the trend **16** > **3** (%ΔWBIs = -1.01% (I.S. 25 J) and -1.62% (I.S. >40 J), respectively), which could be attributed to secondary effects or the twist of the nitro groups crystal packing. Upon constraining the twist in **16**, the %ΔWBIs shift to -1.60% which still does not agree with the trend. However, experimental evidence for **3** is necessary to determine whether the twists of the nitro groups change and thus influence the impact sensitivity.

Assignment of trigger bond strengths through %ΔWBI analysis should agree with experimental sensitivity data. Experimental values were chosen from consistent experimental methods across subsets of the azole-based HEDMs since literature values often vary depending on the technique used.[210-214] Impact sensitivities were selected from a 10 kg drop weight[210] data or the standard BAM fallhammer method[211-214] depending on the subset of the azole-based HEDMs. The correlations between %ΔWBIs and experimental impact sensitivity data for the novel azole-based

HEDMs are not as strong as they were for the nitroaromatic energetic materials,[49] which could be attributed to secondary effects in crystal packing or the lower limit of the drop hammer test. The imperfect R^2 values observed in the correlations for the imidazoles, triazoles and pyrazoles (R^2 = 0.857, 0.534 and 0.589, respectively; **Figure A9**) are likely due to the lower limits of the experimental impact sensitivity data (**Table 5**) and the lack of reproducible results across the literature. However, it could also be due to the different dihedral angles between the gas- and condensed-phases leading to over- and under-prediction of the %ΔWBIs. %ΔWBIs are less predictive for the novel azole-based HEDMs which could be attributed to secondary effects including strong hydrogen bonding networks, intermolecular repulsions, ring strain and other secondary effects in crystal packing. Additionally, the impact sensitivities for the azole-based HEDMs are only reported once in literature and the conventional nitroaromatic energetic materials contain large variations[16, 49] suggesting that the HEDMs would also be dependent on the technique and drop weight used.

Conclusions

WBIs have been used to characterize trigger bonds, defined as the bond most likely to initiate detonation, for a series of azole-based HEDMs. Trigger bonds were determined by comparing WBIs of the energetic materials to those in reference molecules to provide a relative scale for the activation of the bond. $C-NO_2$, $N-NO_2$ and $N-N_2$ trigger bonds were assumed in these HEDMs based on our previous studies.[16, 49] The most activated trigger bond relative to the reference was generally the azide. However, the $N-NO_2$ trigger bond was also significantly activated throughout the azole-based HEDMs. The $C-NO_2$ trigger bonds were strongly influenced by intramolecular hydrogen bonds and were less activated than the $N-NO_2$ and $N-N_2$ trigger bonds,

consistent with our previous work on simple azides and aromatic azide-based energetic materials. As a result, %ΔWBIs can assign trigger bonds to propose initiation for explosive decomposition and interpret energetic properties of novel HEDMs, specifically impact sensitivities. %ΔWBIs do not correlate with impact sensitivity for the azole-based HEDMs likely due to the inconsistent experimental methods and the lack of sufficient data in the literature. Nevertheless, %ΔWBIs could be used as a tool for understanding molecular-level contributions to the origins of energetic properties. %ΔWBI analysis was previously shown to indicate the influence of intramolecular interactions, in agreement with our study; therefore, %ΔWBIs can be used to rationalize the varied sensitivity observed for different explosophore groups across a set of azole-based HEDMs.

CHAPTER 5

INFLUENCE OF PRESSURE ON INTERMOLECULAR INTERACTIONS IN AMMONIUM

NITRATE

Introduction

Generally, conventional, molecular energetic materials undergo explosive decomposition by homolytic cleavage or elimination through X-NO$_2$ (X=N,C,O) and N-N$_2$ trigger bonds.[5, 16, 49] However, energetic materials composed of salts, such as ammonium nitrate, are initiated to decompose by interatomic transfer.[9, 36, 217-219] Ammonium nitrate is the major component used in explosives and propellants since it is a halogen-free, inexpensive oxidizer.[9, 36, 220] The nontoxic detonation products make ammonium nitrate desirable;[9] however, accidental detonation can occur, even when safety precautions are taken.[217, 221] As temperature increases past the melting point (170ºC), different reactions are observed. At lower temperatures (170-200ºC), an endothermic reversible proton transfer reaction occurs as melted ammonium nitrate vaporizes into ammonia and nitric acid (Equation 26):[9, 36, 217, 218, 222]

$$NH_4NO_3(\text{s}) \rightarrow NH_3(g) + HNO_3(g) \tag{26}$$

At higher temperatures and pressures, several dominant and irreversible reactions occur following the explosive hydrogen transfer (Equations 27-35).[9, 36, 217-219] Previous gas-phase theoretical calculations show that the hydrogen transfer is the dominant pathway in the explosive decomposition of ammonium nitrate.[36, 222]

$$HNO_3 \rightarrow \cdot OH + \cdot NO_2 \tag{27}$$

$$\cdot OH + NH_3 \rightarrow \cdot NH_2 + H_2O \tag{28}$$

$$\cdot NH_2 + \cdot NO_2 \rightarrow \cdot H_2NO + \cdot NO \tag{29}$$

$$\cdot NH_2 + \cdot NO_2 \rightarrow N_2O + H_2O \tag{30}$$

$$\cdot NH_2 + \cdot NO \rightarrow N_2H^+ + \cdot OH \tag{31}$$

$$\cdot NH_2 + \cdot NO \rightarrow N_2 + H_2O \tag{32}$$

$$\cdot OH + \cdot OH \rightarrow H_2O + \cdot O \tag{33}$$

$$\cdot OH + HNO_3 \rightarrow H_2O + NO_3^- \tag{34}$$

$$\cdot OH + \cdot H_2NO \rightarrow HNO + H_2O \tag{35}$$
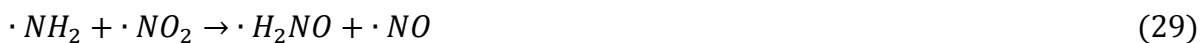
Once hydrogen transfer occurs, nitric acid initiates the chain reaction by breaking the N-O bond (Equation 27) to produce the radicals that propagate the formation of most of the detonation products (Equations 27-35).[222]

Gas-phase calculations serve as a guide for the behavior of energetic materials in the condensed phase;[67] however, because detonation is unique to the condensed phase, characterizing intermolecular interactions are vital for understanding their performance and sensitivities. Studying energetic materials in the solid state provides insight into the stability, efficiency, and environmental compatibility in a crystalline environment. For example, in crystal packing, hydrogen bonding interactions may affect the activation of nitro groups. Many theoretical studies on conventional energetic materials have been performed in the gas phase under ambient conditions (pressure, temperature, etc.),[66, 223] so investigating energetic materials under increased pressure will determine the dependence and influence of intermolecular interactions on their shock-sensitive properties. Other studies in the condensed-phase of conventional energetic materials, such as 2,4,6-trinitrotoluene (TNT), 1,3,5-trinitro-1,3,5-triazacyclohexane (RDX) and ammonium nitrate, have used MD using DFT[65, 224] and reactive force fields (ReaxFF),[225-234] finding structural differences and phase changes,[65, 224-233, 235] confirmed by NMR spectroscopy,[236]

and hot spot formation (i.e., defects in the material (high stress and temperature regions) that promote rapid decomposition).[226-228, 233, 235]

Ammonium nitrate has been widely researched since it is used in various explosive formulations.[9, 36, 220] Through computational and experimental studies, various phases of ammonium nitrate have been determined (**Figure 26**). Phase V is the low temperature phase, confirmed by neutron diffraction studies.[232, 235] At ambient temperatures, the ions rotate to Phase IV, characterized by X-ray crystallography and neutron diffraction.[232, 235] At elevated temperatures, ammonium nitrate forms the disordered Phase III in the presence of small amounts of water.[232, 235] Further heating forces a transition to Phase II, and then Phase I which is disordered and stable up to the melting point.[232, 235] Thus, phase changes observed in the condensed-phase of ammonium nitrate are related to differences in interactions between the ions.

In this study, pressure dependence of ammonium nitrate will be investigated to determine the changes in intermolecular interactions over time. Additionally, the dependence of compressibility on intermolecular interactions and the effect of intermolecular interactions on phase changes will be determined over time with increasing pressure.
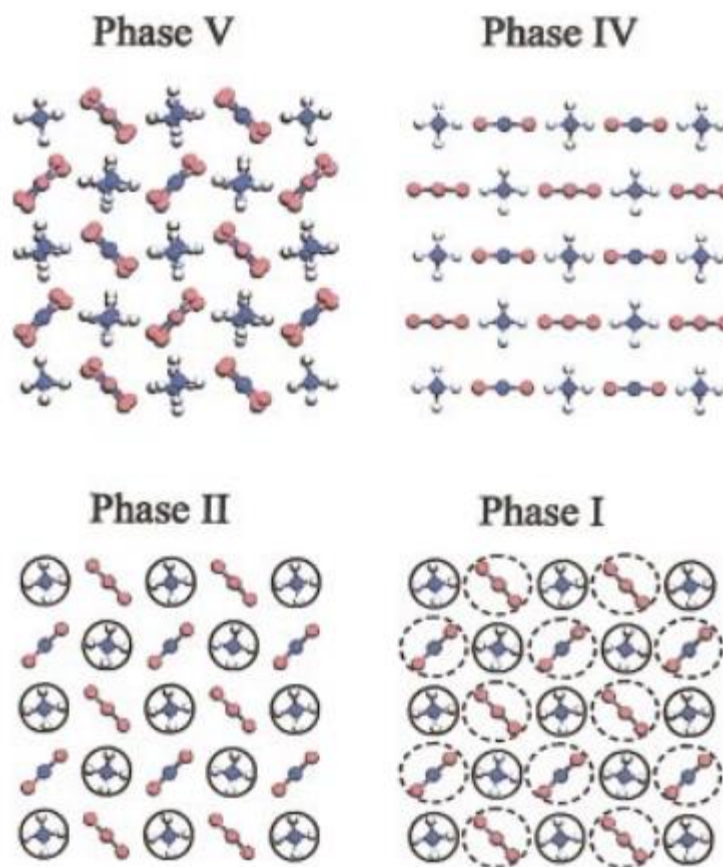
Figure 26. Ammonium nitrate phases V, IV, II, and I with rotational freedom of the ions indicated by circles. Phase III is not shows since it requires moisture. Reprinted from Velardez, G. F.; Alavi, S.; Thompson, D. L. *J. Chem. Phys.* **2004**, *120*, 9151., with the permission of AIP Publishing.

Computational Methods

Geometries were optimized in the condensed-phase, starting from the X-ray crystal structure of Phase IV ammonium nitrate,[237] by Periodic Boundary Conditions (PBC) using Quantum Espresso[47] for a more realistic crystalline environment. The 8-unit cell was used for the ammonium nitrate calculations because it sufficiently models the hydrogen bonding and more importantly the reactivity in a crystalline environment without being too computationally expensive. The Perdew-Burke-Ernzerhof (PBE)[31] pseudopotentials are used for the calculations

due to good correlation to X-ray crystal structural data. Structures were optimized until the energy and forces were well converged, and the molecular dynamics simulations were performed to determine how the optimized structures change over time with increasing pressure. Optimizations were performed using "vc-relax" which allows the optimization of the unit cell parameters as well as all atomic coordinates. Molecular dynamics simulations were conducted using "vc-md" which allows the unit cell parameters and atomic coordinates to fluctuate over time. Pressure was increased incrementally, and the temperature was allowed to equilibrate across the simulation.

Results and Discussion

Optimized Structure of Ammonium Nitrate

Ammonium nitrate was optimized from the X-ray crystal structure at various pressures to determine changes to phase and the hydrogen-bonding between ions. Our optimized structure under ambient conditions (**Figure 27**) is comparable to those previously reported in literature.[232, 234, 237, 238] Our results are consistent with Phase IV of ammonium nitrate, which is reported to be stable up to 323 K.[232, 235] The optimized structure has bond distances in agreement with the X-ray crystal data (i.e., 2.038 Å and 2.326 Å labeled in green, respectively; 2.038 Å and 2.049 Å labeled in yellow, respectively; 1.960 Å and 2.161 Å labeled in pink, respectively).[237] Previous studies indicate that there are five stable conformations of ammonium nitrate at normal pressures and up to the melting point around 442 K, all dependent on the orientation of the ammonium and nitrate ions.[232, 235]
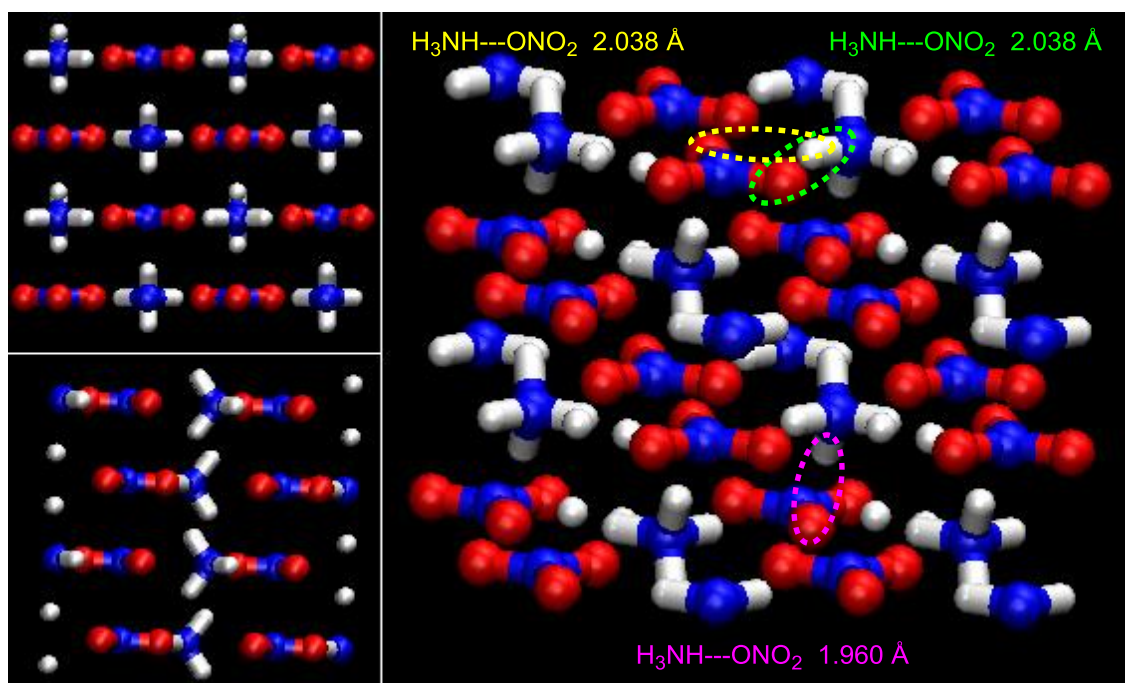
Figure 27. PBC optimized structure of ammonium nitrate under ambient pressure (volume: 1169 Å^3) with hydrogen bonding interactions circled in green, pink and yellow. The hydrogen bonds labeled in green and yellow are identical under ambient pressure.

As the pressure increases from ambient conditions to higher pressures, the unit cell condenses and the hydrogen bonds become shorter. The unit cell appears to retain the Phase IV conformation with slight orientation differences in the ammonium ions as the pressure increases, as seen in **Figures 28-32**. The ammonium ion re-positions to hydrogen bond with the oxygen atom on the nitrate (i.e., circled in yellow) rather than having an equal hydrogen bonding interaction, which is observed under ambient conditions. Upon increasing the pressure to 30 GPa and 35 GPa, the unit cell contains a strong hydrogen bonding network with much shorter hydrogen bonds than those observed under ambient conditions (1.590 Å, 1.575 Å and 2.038 Å, respectively). Therefore, intermolecular interactions are influenced by pressure which decreases the volume and makes the unit cell more compact. The unit cell retains order at the increased pressures, but molecular

dynamics simulations are performed to determine whether changes in orientation and crystal packing occur as the pressure increases along with temperature.
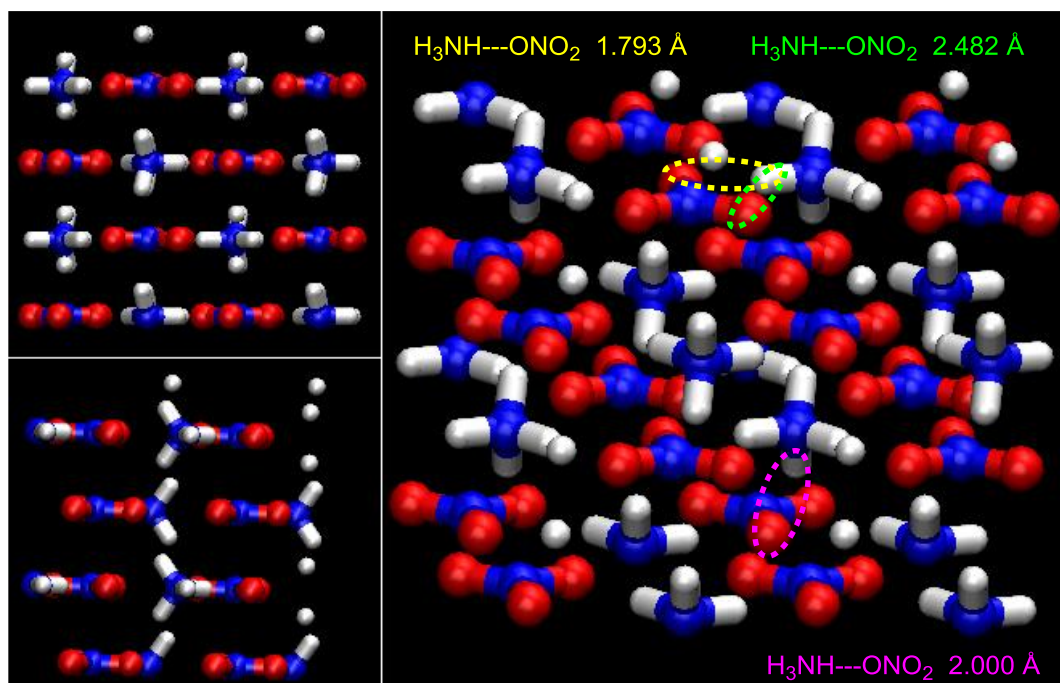
Figure 28. PBC optimized structure of ammonium nitrate at 1 GPa (volume: 1134 Å^3) with hydrogen bonding interactions circled in green, pink and yellow.
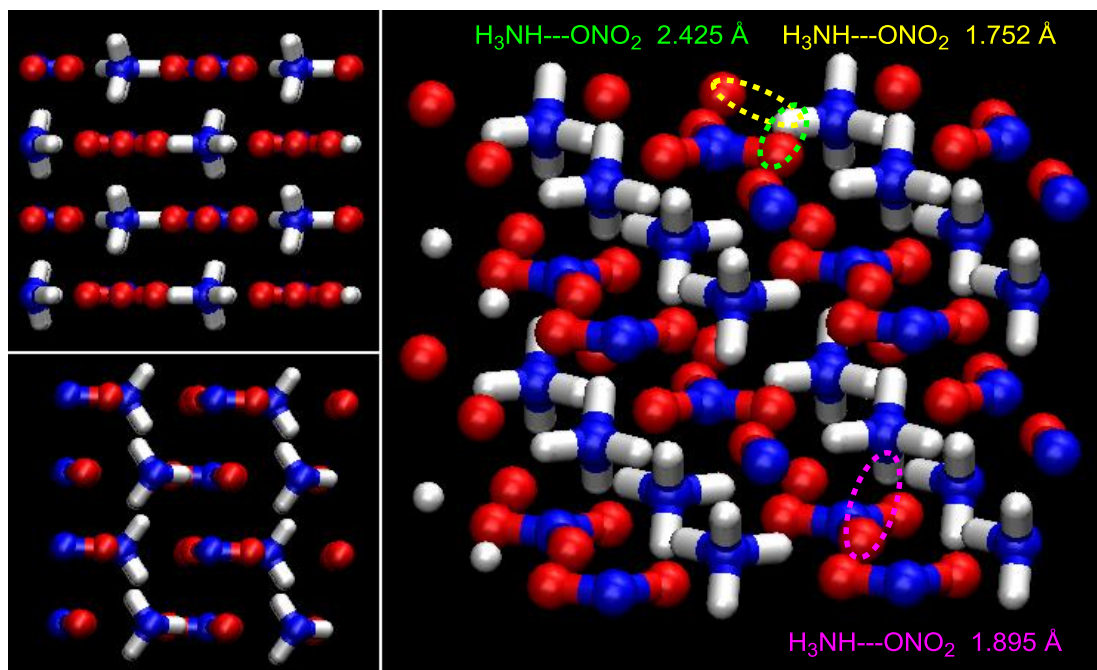
Figure 29. PBC optimized structure of ammonium nitrate at 5 GPa (volume: 1024 Å³) with hydrogen bonding interactions circled in green, pink and yellow.
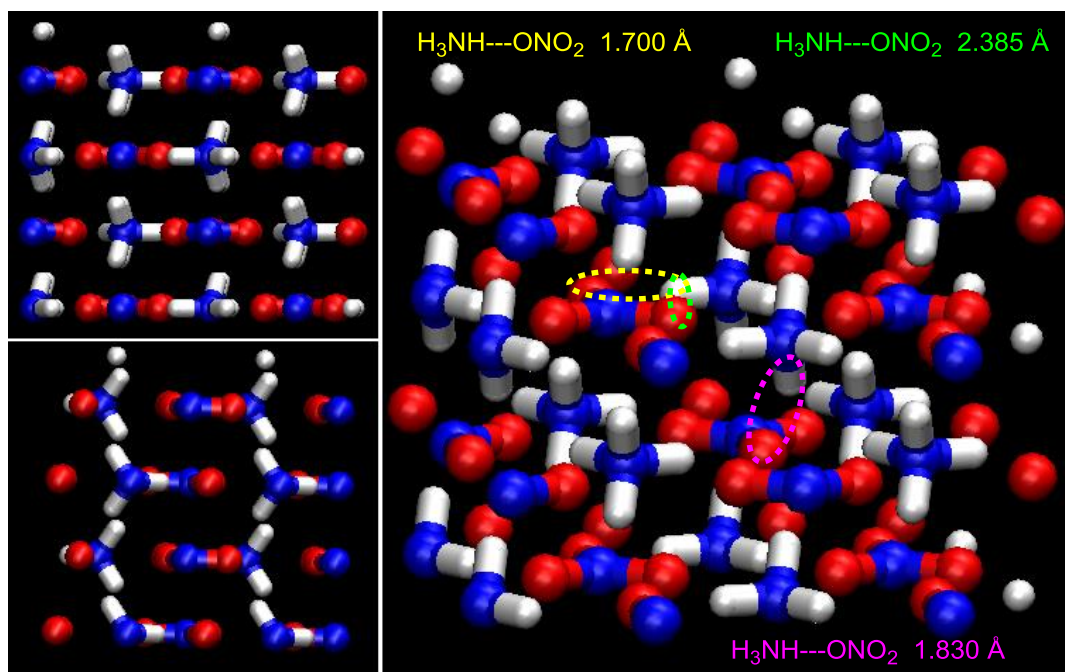
Figure 30. PBC optimized structure of ammonium nitrate at 10 GPa (volume: 947 Å³) with hydrogen bonding interactions circled in green, pink and yellow.
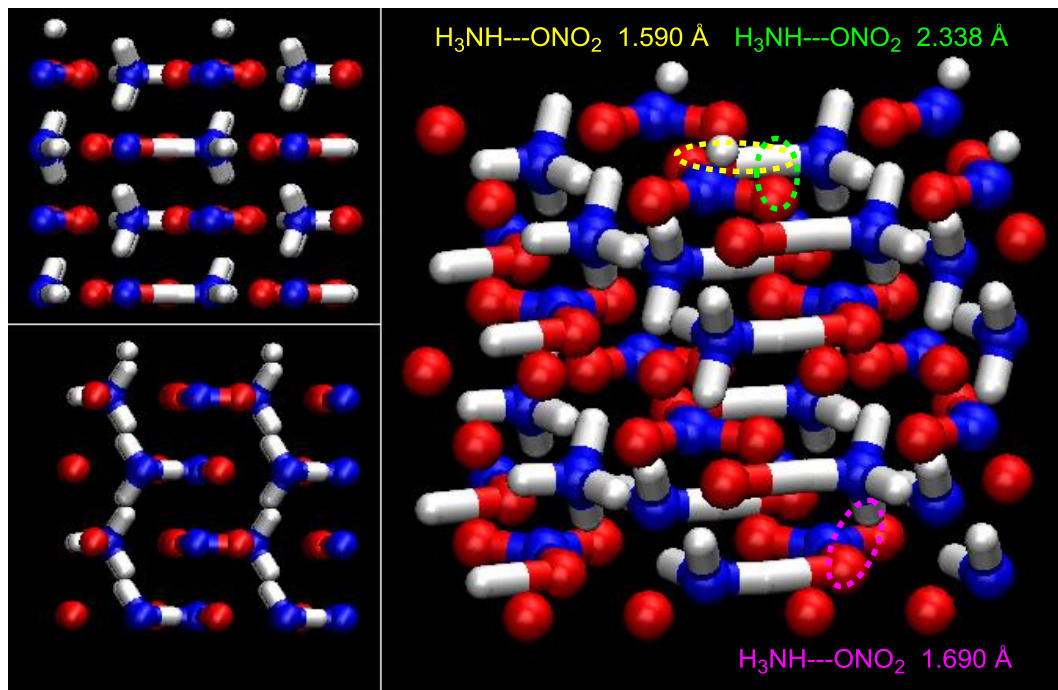
Figure 31. PBC optimized structure of ammonium nitrate at 30 GPa (volume: 792 Å^3) with hydrogen bonding interactions circled in green, pink and yellow.
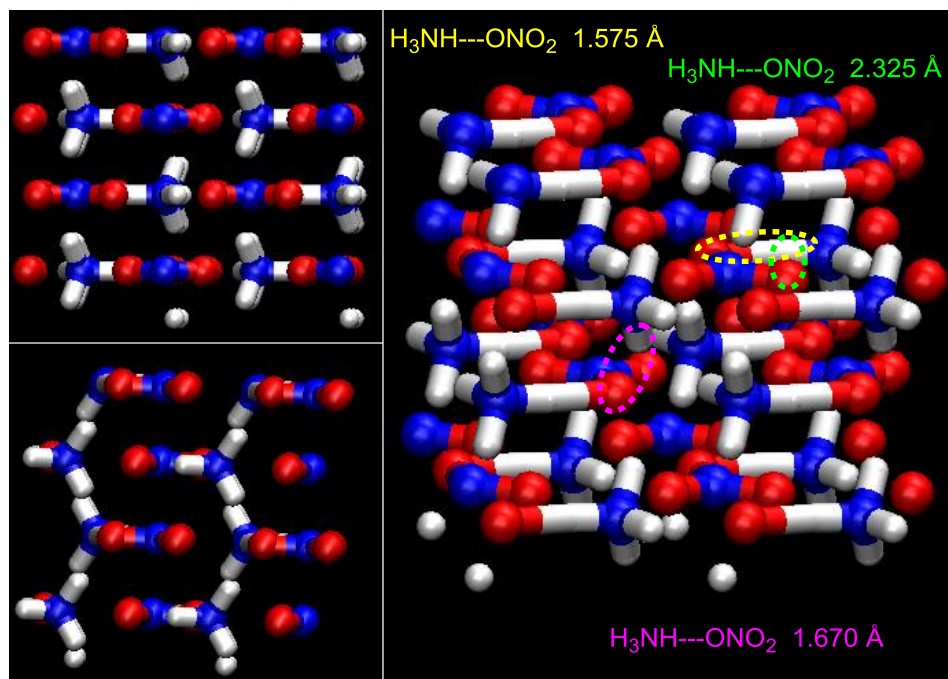
Figure 32. PBC optimized structure of ammonium nitrate at 35 GPa (volume: 768 Å^3) with hydrogen bonding interactions circled in green, pink and yellow.

Detonation Mechanism Analysis of Ammonium Nitrate by Molecular Dynamics

Previous experimental studies[9, 218, 219] have found that ammonium nitrate can undergo several decomposition pathways, with the most common being hydrogen transfer to form ammonia and nitric acid.[9, 234] In the molecular dynamics calculations, we took the optimized structure of ammonium nitrate under ambient conditions and then increased the pressure to see how conformation, orientation and intermolecular interactions change over time. A previous study ReaxFF and a 48-unit cell of ammonium nitrate found that as temperature increased from 0 K to 2500 K, phases I, IV and V are observed.[234] Additionally, the pressure increases to 5 GPa at the highest temperature.[234] Another study found Phase IV is retained at pressures up to 600 GPa and no hydrogen transfer occurs from the ammonium ion to the nitrate ion to form nitric acid and ammonia.[235] Since a phase change is not observed through 600 GPa, better computational methods

are necessary to model structural differences and the energetic nature of compounds like ammonium nitrate.

Under ambient pressure, molecular dynamics simulations indicate that the unit cell retains the Phase IV conformation, as observed with the optimization, without much movement of the ammonium and nitrate ions (**Figure 33**). The $H_3NH\cdots ONO_2$ intermolecular hydrogen bond, labeled in green in **Figure 33**, fluctuates between 1.725 Å and 2.100 Å throughout the simulation. The corresponding N-H bond distance varies (i.e., 1.032 Å and 1.051 Å) but equilibrates around 1.042 Å while the N-O bond distance changes (i.e., 1.256 Å and 1.270 Å) but stabilizes around 1.265 Å Additionally, the $H_3NH\cdots ONO_2$ intermolecular hydrogen bond between the layers of the unit cell, labeled in pink in **Figure 33**, fluctuates between 1.875 Å and 2.275 Å throughout the simulation, finding increased stability around 2.125 Å and 2.025 Å. The corresponding N-H bond distance varies (i.e., 1.024 Å and 1.040 Å) but stabilizes around 1.033 Å while the N-O bond distance changes (i.e., 1.284 Å and 1.298 Å) but stabilizes around 1.292 Å. The temperature equilibrates around 21 K and the energy stabilizes between -6 kcal/mol and -11 kcal/mol (**Figure 34**) while the volume varies around 1195 $Å^3$. Equilibration at such a low temperature could be attributed to the size of the unit cell (i.e., larger volume) and the ambient conditions (i.e., small pressure).
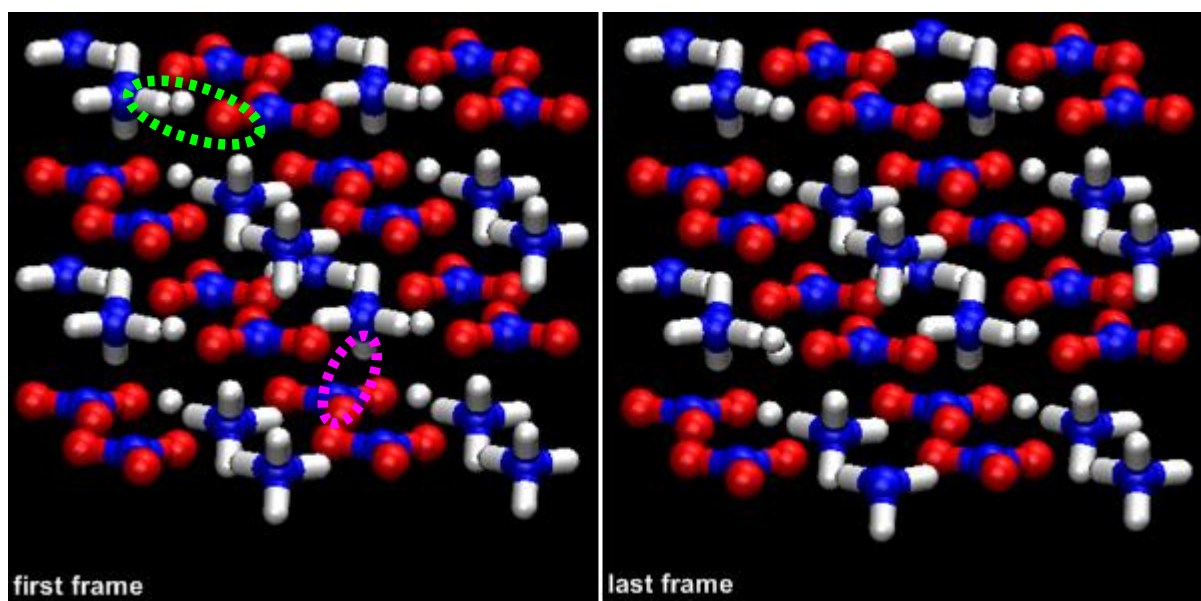
Figure 33. MD structures of ammonium nitrate under ambient pressure with hydrogen bonding interactions circled in green and pink.
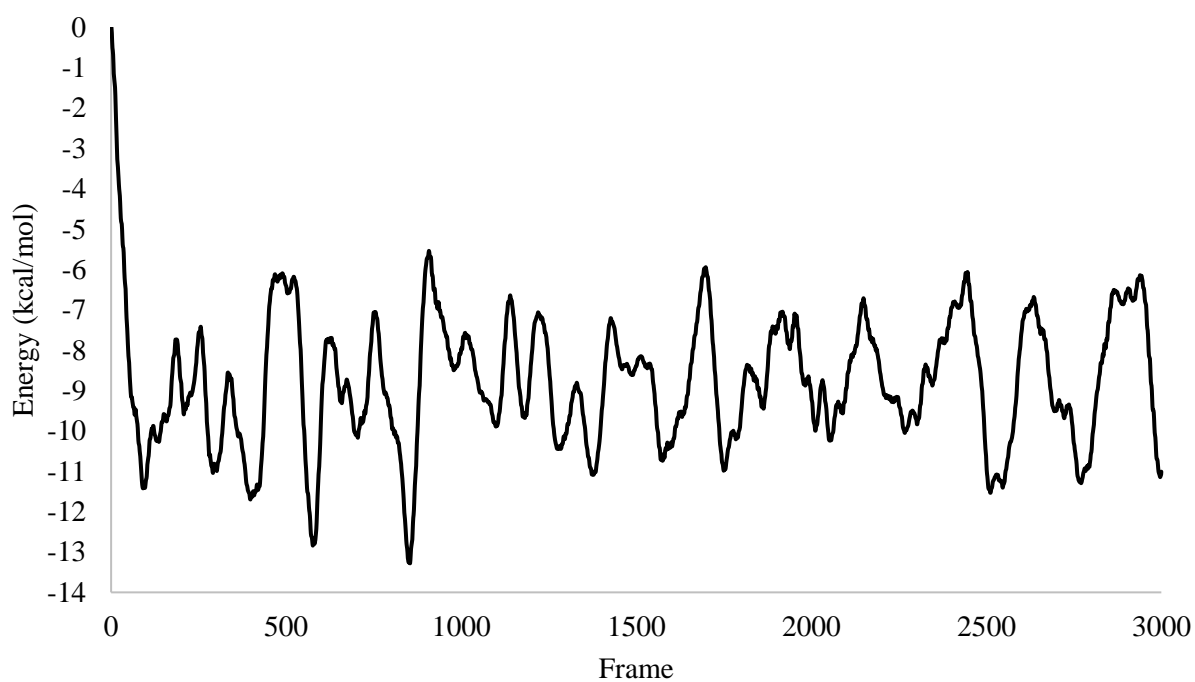
Figure 34. Energy plot of ammonium nitrate at ambient pressure.

The unit cell becomes more compact and starts to deviate slightly from the Phase IV conformation at 5 GPa due to the orientation of the ions across the simulation (**Figure 35**). However, the structure equilibrates back to Phase IV by the end of the simulation. The $H_3NH\cdots ONO_2$ intermolecular hydrogen bond, labeled in green in **Figure 35**, fluctuates between 2.175 Å and 1.650 Å throughout the simulation. The corresponding N-H bond distance varies between 1.023 Å and 1.048 Å while the N-O bond distance changes between 1.258 Å and 1.278 Å. Additionally, the $H_3NH\cdots ONO_2$ intermolecular hydrogen bond between the layers of the unit cell, labeled in pink in **Figure 35**, fluctuates between 1.875 Å and 2.100 Å throughout the simulation. The corresponding N-H bond distance varies between 1.029 Å and 1.037 Å while the N-O bond distance changes between 1.278 Å and 1.295 Å. Additionally, the $H_3NH\cdots ONO_2$ hydrogen bond labeled blue in **Figure 35**, is shortened to around 1.575 Å, indicative of the strong hydrogen bonding network; however, that bond also increases to 2.200 Å in the simulation. An important note is that the hydrogen bond only lasts for a few frames (~0.004 ps), suggesting that a higher pressure will be required for a hydrogen transfer to occur. The temperature plateaus around 138 K, the energy stabilizes around +68 kcal/mol (**Figure 36**), and the volume starts to equilibrate toward the end of the simulation around 1050 $Å^3$. The large variation in the energy over the first half of the simulation can be attributed to the large fluctuation in the unit cell volume across the first 2100 frames.
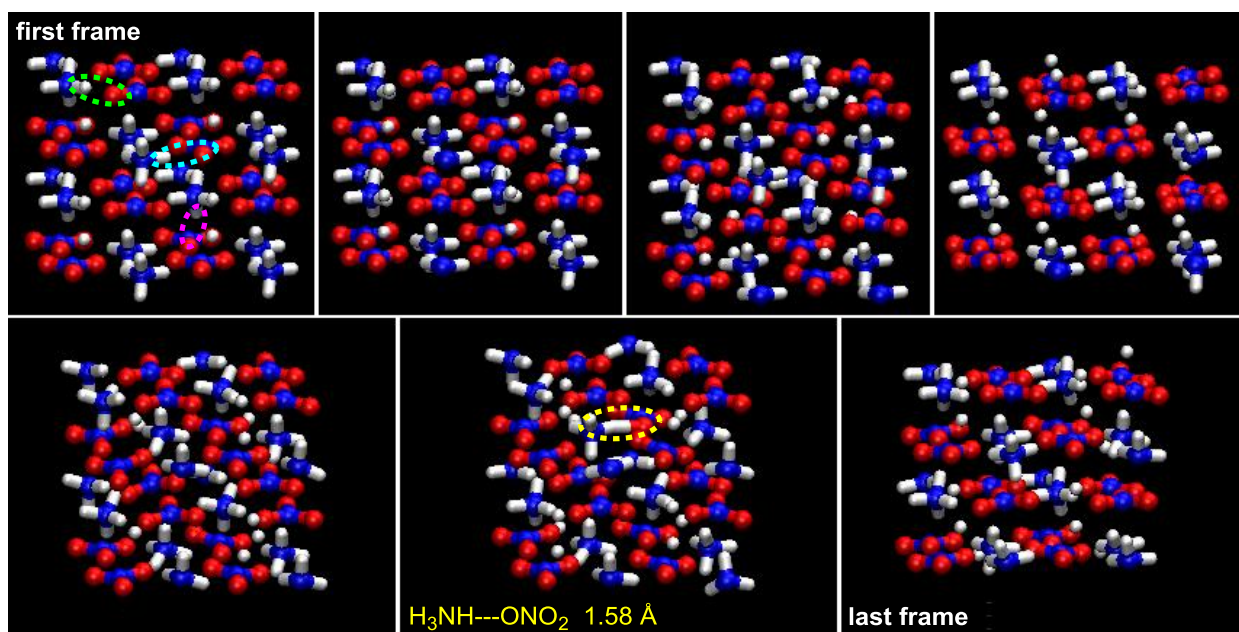
Figure 35. MD structures of ammonium nitrate at 5 GPa with hydrogen bonding interactions circled in green, pink, blue and yellow.
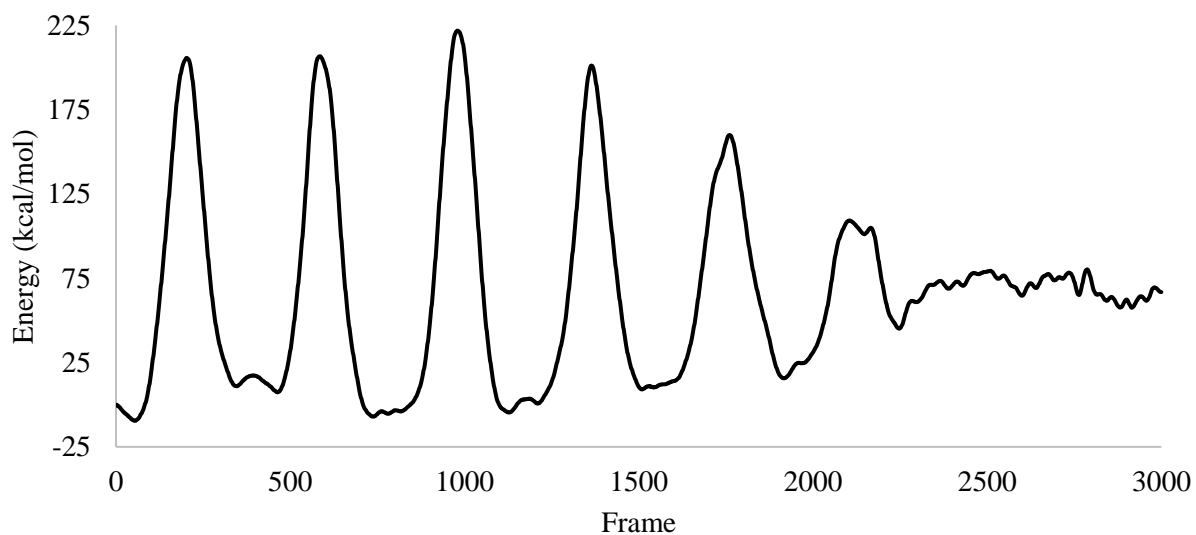
Figure 36. Energy plot of ammonium nitrate at 5 GPa.

As the pressure increases to 35 GPa, the unit cell becomes more compact and disordered as observed in the initial structure (**Figure 37**). Furthermore, the intermolecular $H_3NH\cdots ONO_2$ hydrogen bonding interactions fluctuate drastically. For example, the hydrogen bond labeled in green in the first and last frames in **Figure 37** oscillates between 1.500 Å and 4.000 Å across the simulation, which can be attributed to the rapid rotation of the ammonium and nitrate ions. The corresponding N-H bond distance varies between ~1.000 Å and ~1.300 Å while the N-O bond distance changes between ~1.200 Å and ~1.350 Å. The temperature equilibrates around 1722 K and the volume stabilizes around 820 $Å^3$ while the energy fluctuates, due to the rapid rotation of the ions (**Figure 38**). The temperature equilibrates at a higher value because the volume of the unit cell decreases drastically with greater pressure.
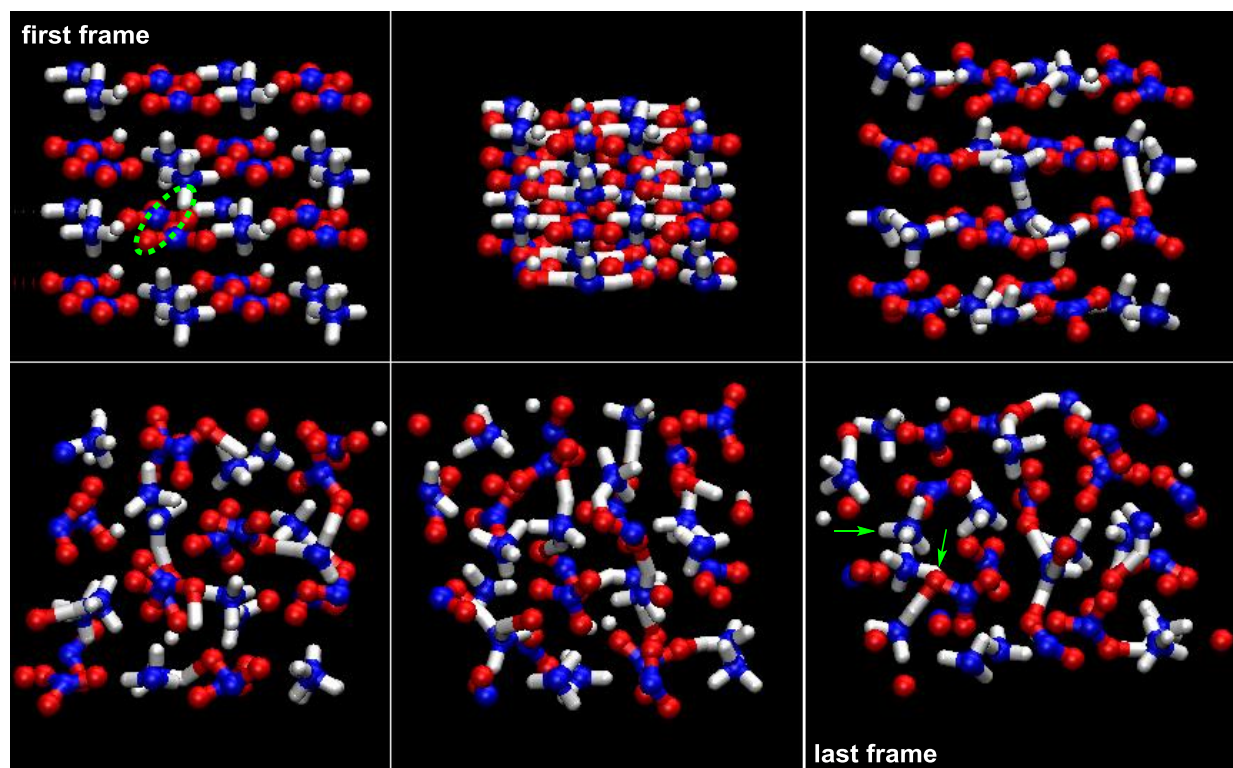
Figure 37. MD structures of ammonium nitrate at 35 GPa with hydrogen bonding interactions circled in green and the green arrows show their reorientation.
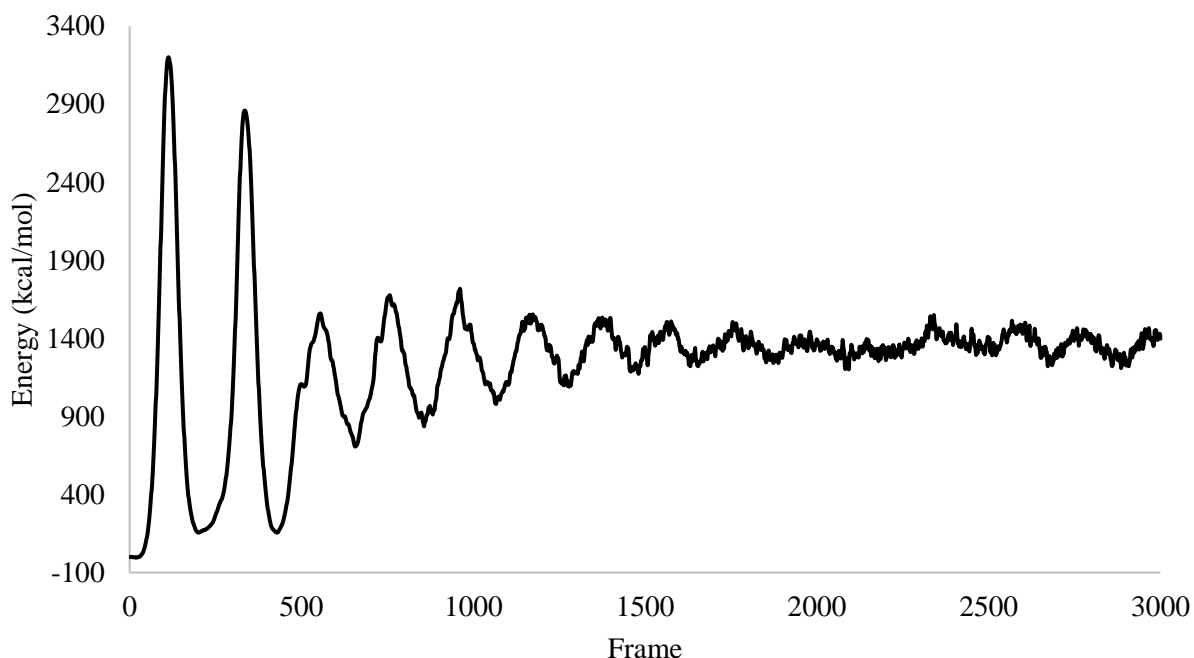
Figure 38. Energy plot of ammonium nitrate at 35 GPa.

As the pressure increases to 40 GPa, the unit cell becomes more compact, the hydrogen bonding network is increased, and then completely loses the Phase IV conformation observed in the initial structure (**Figure 39**), similarly to the simulation at 35 GPa. The temperature equilibrates around 2074 K and the volume stabilizes around 813 Å^3. The energy fluctuates widely at the beginning of the simulation due to the large changes in overall compactness (**Figure 40**), similarly to the results at 35 GPa. A difference between ammonium nitrate at 35 GPa and 40 GPa is that hydrogen transfer occurs toward the end of the simulation, forming ammonia and nitric acid, at 40 GPa (**Figure 39**), which could also contribute to the large energy variation. Looking closer at the energy after hydrogen transfer (**Figure 40**, circled in red), you can see stabilization of the energy around +1580 kcal/mol. The energy is relatively stable in these frames which indicates the increased strength and shortness of the O-H bond from hydrogen transfer to produce ammonia and

nitric acid (**Figure 39**, labeled in pink). The initial hydrogen bond labeled in green in **Figure 39** is traced in **Figure 41**, finding the hydrogen bond transfer toward the end of the simulation (i.e., ~1.000 Å) for the formation of ammonia and nitric acid (**Figure 39**, labeled yellow) accompanied by other strong hydrogen bonding interactions. The results indicate the initial bond breaking and formation that could lead to detonation at 40 GPa. Longer simulations are required in order to show complete detonation of ammonium nitrate.
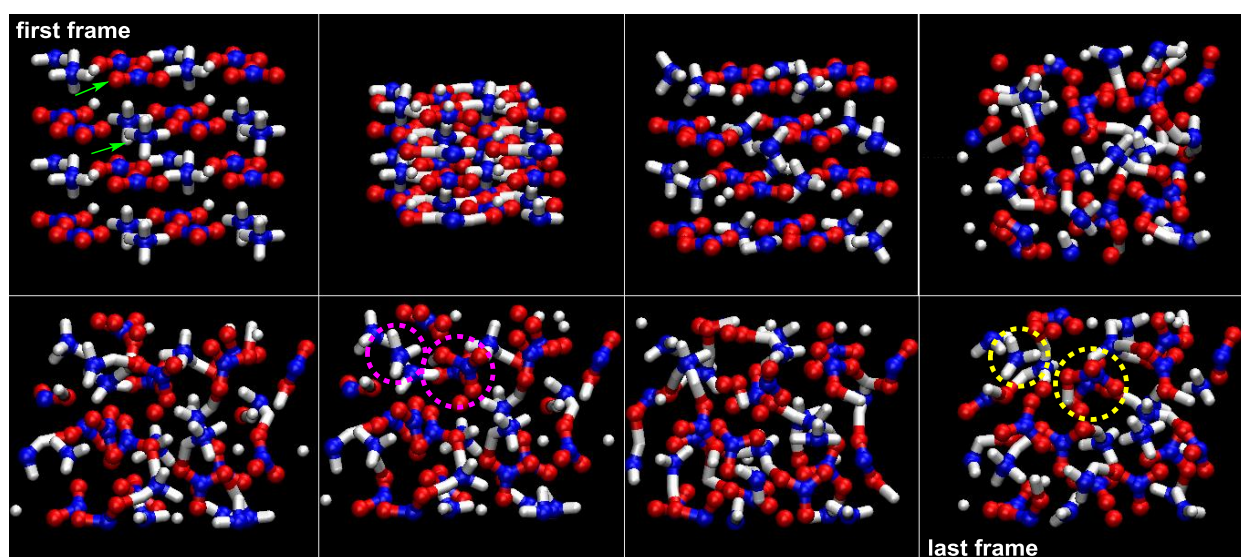
Figure 39. MD structures of ammonium nitrate at 40 GPa. Green arrows indicate the hydrogen that is transferred to the nitrate, which is circled in pink and yellow.
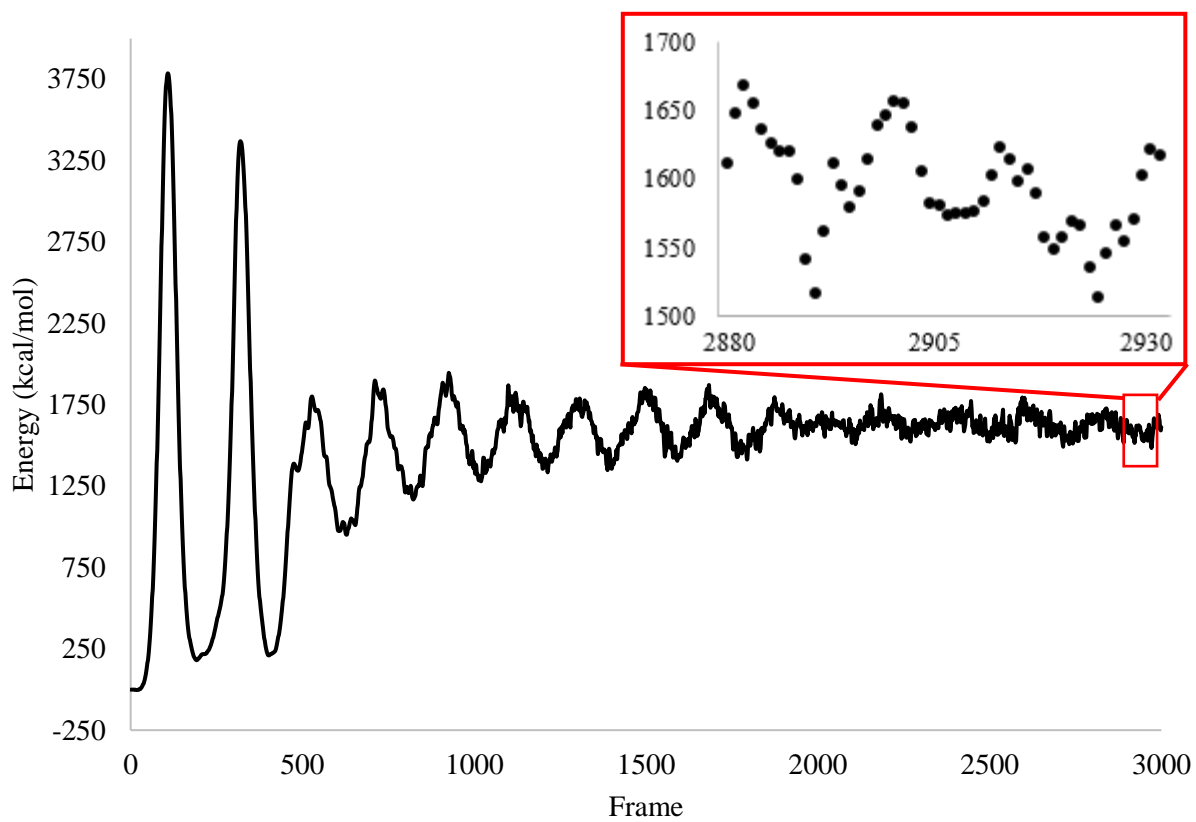
Figure 40. Energy plot of ammonium nitrate at 40 GPa.
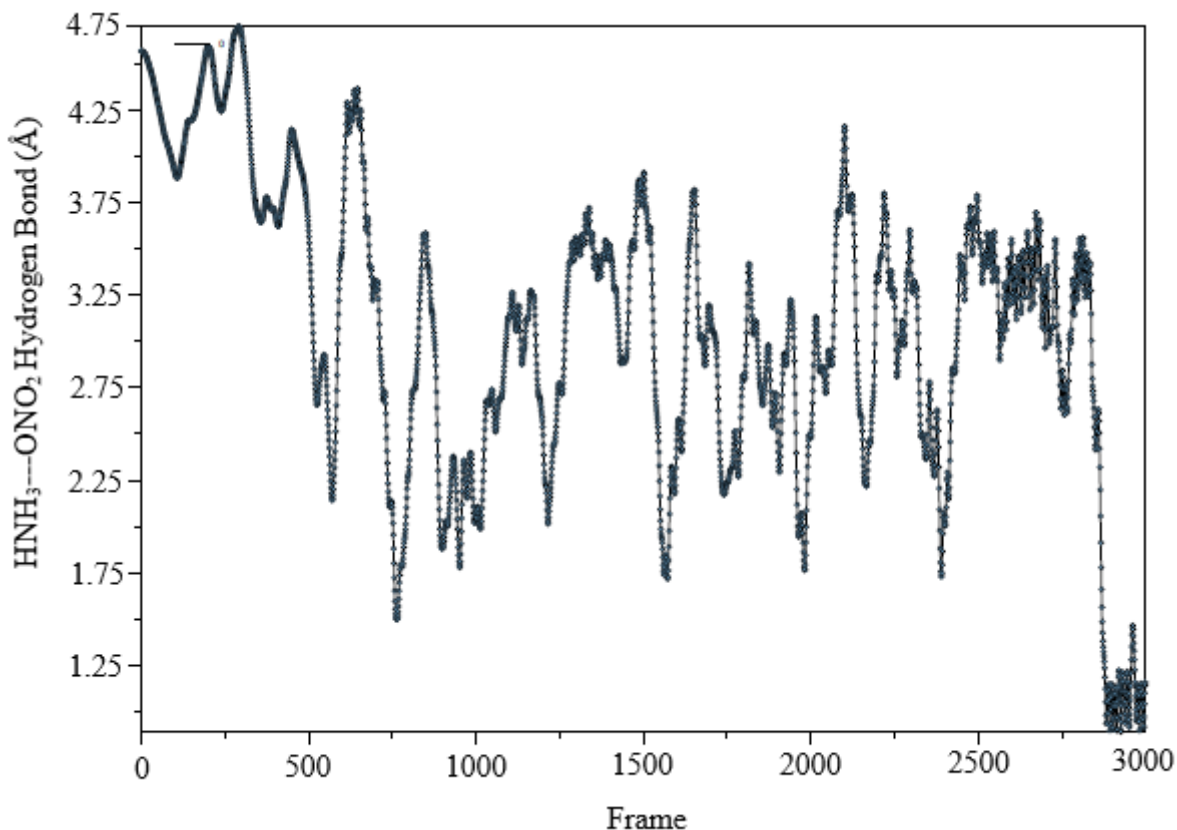
Figure 41. Trace of the intermolecular $H_3NH\cdots ONO_2$ hydrogen bond labeled with green arrows in **Figure 39**.

Conclusions

The pressure dependence of ammonium nitrate is studied since it is a simple energetic material that remains widely used as an oxidizer in propellants and explosives. As the pressure increases, the unit cell becomes more compact and the hydrogen bonds become shorter, indicating an increase in the hydrogen-bonding network. The interactions between ions observed in the optimizations change with increasing pressure, indicating the orientation of the ions are influenced by pressure. Furthermore, the MD simulations suggest that intermolecular hydrogen transfer of ammonium nitrate to form ammonia and nitric acid occurs around 40 GPa. The transfer of hydrogen, even though it only lasted over a few frames in the simulation, is dependent on pressure.

However, the study on ammonium nitrate should be continued to determine the exact pressure at which detonation occurs as well as determine whether the hydrogen transfer can last more than a few frames. By studying ammonium nitrate over a longer time frame, we hope to see the final products from Equations 27-35 become more definitive throughout the MD simulation. Additionally, exploring the detonation mechanisms in novel, 'green' HEDMs can help understand the effect that intermolecular interactions have on the sensitivity of these molecular materials and the activation of trigger bonds by the pressure front of an impact.

CHAPTER 6

CONCLUSION

The development of novel high energy density materials (HEDMs) used in military, aeronautics and planetary sample collection applications depends on understanding how and why detonation occurs in conventional energetic materials. These reactions are highly energetic, making experimental modeling incredibly difficult; therefore, computational tools can be used to build a comprehensive understanding to this phenomenon. Computational methods such as density functional theory (DFT) and molecular dynamics (MD) have been used to propose the bond that breaks to initiate explosive decomposition. The activation of trigger bonds, weak bonds that break to initiate explosive decomposition, are characterized by the Wiberg bond index (WBI), a measure of interatomic electron density.

Potential trigger bonds in HEDMs are based on explosophores substituted to the energetic backbone and most often include $X-NO_2$ (X=N,C,O) and $N-N_2$ bonds. The WBIs of the trigger bonds in HEDMs were compared to those in chemically similar reference molecules with the same bond type, hybridization and explosophore as the HEDM to provide a relative scale for bond activation (%ΔWBIs). The trigger bonds in the HEDMs are expected to be longer and more activated than the bond in the corresponding reference molecule. This measure of the activation of the potential trigger bonds could be applied to guide the synthesis of novel HEDMs by prescreening their energetic potential.

Trigger bonds in the conventional and novel energetic materials were assigned based on the most negative %ΔWBI relative to the corresponding reference molecule. The %ΔWBIs of nitroaromatic energetic materials indicate that $C-NO_2$ trigger bonds are deactivated with

intramolecular hydrogen bonding due to increased double bond character from resonance which stabilize the HEDMs. Nitroanilines deactivate nitro groups due to two hydrogen bonding interactions which increases the double bond character by forcing $-NO_2$ planarity with the ring. Resonance structures induced by hydrogen bonding with $-OH$ groups also enhance double bond character of the *ortho* nitro group. However, the unidirectionality of the hydroxyl hydrogen bond leads to an activating repulsive interaction with the lone pair that forces a twist in the other *ortho* nitro group, resulting in the increased sensitivity of nitrophenols relative to nitroanilines. Steric effects from interactions of neighboring nitro groups also activate $C-NO_2$ trigger bonds by increasing the dihedral angle, and the HEDMs become more sensitive. The $\%\Delta WBIs$ correlated strongly with experimental measures of sensitivity (i.e., impact and electrical spark sensitivities) when compared to bond dissociation energies (BDEs). Aromatic azide-based energetic materials contained both nitro and azide functional groups. The azide trigger bond is more activated than the $C-NO_2$ bond, consistent with previous experimental results. The $N-N_2$ bond will break to release N_2 and then cyclize with an adjacent nitro group to produce a benzofuroxan derivative. However, if the nitro group is *meta* or *para* to the azide, then cyclization cannot occur and instead a nitrene is formed. Our results on novel azole-based HEDMs found that the $C-NO_2$ bond is less activating than $N-NO_2$ and $N-N_2$ trigger bonds. Therefore, $\%\Delta WBIs$ may designate the bond that breaks to initiate explosive decomposition and differentiate between the contributions that different explosophores have on sensitivity, which is important for interpreting the origins of energetic properties at a molecular level. However, gas-phase $\%\Delta WBIs$ can only provide a clue into how intramolecular interactions influence the sensitivity of energetic materials. Since detonation is unique to the solid state, condensed-phase calculations are required to understand the effect of intermolecular interactions on the sensitivity of HEDMs.

Ammonium nitrate, an energetic salt, undergoes explosive decomposition through the hydrogen transfer from ammonium to nitrate to form ammonia and nitric acid. A study of ammonium nitrate demonstrates that the hydrogen transfer occurs with greater frequency as the pressure increases. In optimization calculations, the unit cell became more compact and an increase in the hydrogen bonding network was observed with greater pressure. As pressure increased across a molecular dynamics simulation, hydrogen transfer is observed at 40 GPa. The fact that overcoming the barrier for hydrogen transfer requires such a high pressure could explain why ammonium nitrate is relatively stable and is typically combined with azides or other fuel sources for an explosive mixture.

In future work, extending these modeling studies to HEDMs with different types of explosophores will validate that conventional and novel energetic materials can be categorized by using %ΔWBIs. Additionally, various molecular and ionic HEDMs with more complex functional groups (i.e., nitro (-NO_2) and azide (-N_3) groups) can be modeled in the condensed-phase to determine the influence of intermolecular interactions on their shock-sensitive properties. These calculations will be computationally expensive, but the lessons learned from the modeling of ammonium nitrate will guide those of more complex energetic materials. The insight gained through the gas- and condensed-phase models of contributions of intramolecular and intermolecular interactions to the sensitivity of trigger bond types can be used to guide the synthesis of 'green' HEDMs with superior properties and less hazardous waste.

REFERENCES

1. P. J. Kaste and B. M. Rice, *AMPTIAC Q.*, 2005, **8**, 85-89.
2. E. C. Hayden, *Nature News*, 2011, **479**, 458.
3. M. H. V. Huynh, M. A. Hiskey, T. J. Meyer and M. Wetzler, *Proc. Natl. Acad. Sci. U. S. A.*, 2006, **103**, 5409-5412.
4. A. Witze, *Nature*, 2013, **500**, 509-510.
5. P. Yin, Q. Zhang and J. n. M. Shreeve, *Acc. Chem. Res.*, 2016, **49**, 4-16.
6. T. M. Klapötke, *Chemistry of High-Energy Materials*, De Gruyter, 2012.
7. J. Akhavan, *The Chemistry of Explosives*, Royal Society of Chemistry, Cambridge, UK, 2011.
8. A. Davenas, *J. Propul. Power*, 2003, **19**, 1108-1128.
9. C. Oommen and S. R. Jain, *J. Haz. Mat.*, 1999, **67**, 253-281.
10. J. Giles, *Nature*, 2004, **427**, 580-581.
11. J. Stierstorfer, K. R. Tarantik and T. M. Klapötke, *Chem. Eur. J.*, 2009, **15**, 5775-5792.
12. M. Elvis, *Nature*, 2012, **485**, 549.
13. D. Adam, K. Karaghiosoff and T. M. Klapötke, *Propellants Explos. Pyrotech.*, 2002, **27**, 7-11.
14. G. F. Adams and R. W. Shaw Jr, *Ann. Rev. Phys. Chem.*, 1992, **43**, 311-340.
15. C. F. Melius and J. S. Binkley, *Symp. (Int.) Combust.*, 1988, **21**, 1953-1963.
16. L. K. Harper, A. L. Shoaf and C. A. Bayse, *ChemPhysChem*, 2015, **16**, 3886-3892.
17. S. N. Bulusu, *Chemistry and Physics of Energetic Materials*, Kluwer Academic Publishers, Printed in the Netherlands, 1990.
18. V. Boddu and P. Redner, *Energetic Materials: Theromophysical Properties, Predictions, and Experimental Measurements*, Taylor & Francis, Boca Raton, FL, 2010.
19. J. R. Sabin, *Advances in Quantum Chemistry*, Academic Press, 2014, vol. Volume 69, pp. 1-360.
20. I. N. Levine, *Quantum Chemistry*, Prentice Hall, Upper Saddle River, New Jersey, 5 edn., 2000.
21. J. B. Foresman and Æ. Frisch, *Exploring Chemistry with Electronic Structure Methods*, Gaussian, Inc., Pittsburgh PA, 2nd edn., 1996.
22. C. J. Cramer, *Essentials of Computational Chemistry Theories and Models*, John Wiley & Sons Inc., Hoboken, NJ, 2004.
23. D. Maurice and M. Head-Gordon, *Mol. Phys.*, 1999, **96**, 1533-1541.
24. G. D. Purvis III and R. J. Bartlett, *J. Chem. Phys.*, 1982, **76**, 1910-1918.
25. C. Møller and M. S. Plesset, *Phys. Rev.*, 1934, **46**, 618-622.
26. E. Lewars, *Computational Chemistry Introduction to the Theory and Applications of Molecular and Quantum Mechanics*, Kluwer Academic Publishers, Boston, 2003.
27. W. Koch and M. C. Holthausen, *A Chemist's Guide to Density Functional Theory*, Wiley-VCH, New York, 2nd edn., 2001.
28. W. Kohn and L. J. Sham, *Phys. Rev.*, 1965, **140**, A1133-A1138.
29. R. G. Parr and W. Yang, *Density-Functional Theory of Atoms and Molecules*, Oxford University Press, New York, 1989.
30. S. H. Vosko, L. Wilk and M. Nusair, *Can. J. Phys.*, 1980, **58**, 1200-1211.
31. J. P. Perdew, K. Burke and M. Ernzerhof, *Phys. Rev. Lett.*, 1996, **77**, 3865-3868.

32. J. P. Perdew, J. A. Chevary, S. H. Vosko, K. A. Jackson, M. R. Pederson, D. J. Singh and C. Fiolhais, *Phys. Rev. B*, 1992, **46**, 6671-6687.
33. A. D. Becke, *Phys. Rev. A*, 1988, **38**, 3098.
34. C. Lee, W. Yang and R. G. Parr, *Phys. Rev. B*, 1988, **37**, 785-789.
35. Y. Zhao and D. G. Truhlar, *Theor Chem Acc*, 2008, **120**, 215-241.
36. S. Cagnina, P. Rotureau, G. Fayet and C. Adamo, *Phys. Chem. Chem. Phys.*, 2013, **15**, 10849.
37. Y. Ma, A. Zhang, C. Zhang, D. Jiang, Y. Zhu and C. Zhang, *Cryst. Growth Des.*, 2014, **14**, 4703-4713.
38. S. F. Boys, *Proc. R. Soc. Lond. A*, 1950, **200**, 542-554.
39. F. Jensen, *Introduction to Computational Chemistry*, John Wiley & Sons Inc, Hoboken, NJ, 2nd edn., 2007.
40. R. Ditchfield, W. J. Hehre and J. A. Pople, *J. Chem. Phys.*, 1971, **54**, 724-728.
41. M. J. Frisch, J. A. Pople and J. S. Binkley, *J. Chem. Phys.*, 1984, **80**, 3265-3269.
42. D. E. Woon and T. H. Dunning Jr., *J. Chem. Phys.*, 1993, **98**, 1358-1371.
43. A. Schäfer, H. Horn and R. Ahlrichs, *J. Chem. Phys.*, 1992, **97**, 2571-2577.
44. A. Schäfer, C. Huber and R. Ahlrichs, *J. Chem. Phys.*, 1994, **100**, 5829-5835.
45. R. M. Martin, *Electronic Structure: Basic Theory and Practical Methods*, Cambridge University Press, Cambridge, UK, 2004.
46. M. J. Frisch, G. W. Trucks, H. B. Schlegel, G. E. Scuseria, M. A. Robb, J. R. Cheeseman, G. Scalmani, V. Barone, B. Mennucci, G. A. Petersson, H. Nakatsuji, M. Caricato, X. Li, H. P. Hratchian, A. F. Izmaylov, J. Bloino, G. Zheng, J. L. Sonnenberg, M. Hada, M. Ehara, K. Toyota, R. Fukuda, J. Hasegawa, M. Ishida, T. Nakajima, Y. Honda, O. Kitao, H. Nakai, T. Vreven, J. A. Montgomery Jr., J. E. Peralta, F. Ogliaro, M. J. Bearpark, J. Heyd, E. N. Brothers, K. N. Kudin, V. N. Staroverov, R. Kobayashi, J. Normand, K. Raghavachari, A. P. Rendell, J. C. Burant, S. S. Iyengar, J. Tomasi, M. Cossi, N. Rega, N. J. Millam, M. Klene, J. E. Knox, J. B. Cross, V. Bakken, C. Adamo, J. Jaramillo, R. Gomperts, R. E. Stratmann, O. Yazyev, A. J. Austin, R. Cammi, C. Pomelli, J. W. Ochterski, R. L. Martin, K. Morokuma, V. G. Zakrzewski, G. A. Voth, P. Salvador, J. J. Dannenberg, S. Dapprich, A. D. Daniels, Ö. Farkas, J. B. Foresman, J. V. Ortiz, J. Cioslowski and D. J. Fox, *Journal*, 2009.
47. P. Giannozzi, S. Baroni, N. Bonini, M. Calandra, R. Car, C. Cavazzoni, D. Ceresoli, G. L. Chiarotti, M. Cococcioni, I. Dabo, A. D. Corso, S. d. Gironcoli, S. Fabris, G. Fratesi, R. Gebauer, U. Gerstmann, C. Gougoussis, A. Kokalj, M. Lazzeri, L. Martin-Samos, N. Marzari, F. Mauri, R. Mazzarello, S. Paolini, A. Pasquarello, L. Paulatto, C. Sbraccia, S. Scandolo, G. Sclauzero, A. P. Seitsonen, A. Smogunov, P. Umari and R. M. Wentzcovitch, *J. Phys.: Condens. Matter*, 2009, **21**, 395502.
48. A. Schäfer, C. Huber and R. Ahlrichs, *J. Chem. Phys.*, 1994, **100**, 5829-5835.
49. A. L. Shoaf and C. A. Bayse, *J. Comp. Chem.*, 2018, **39**, 1236-1248.
50. J. P. Foster and F. Weinhold, *J. Am. Chem. Soc.*, 1980, **102**, 7211-7218.
51. A. E. Reed and F. Weinhold, *J. Chem. Phys.*, 1983, **78**, 4066-4073.
52. R. Boese, T. M. Klapötke, P. Mayer and V. Verma, *Propellants Explos. Pyrotech.*, 2006, **31**, 263-268.
53. X. Jin, B. Hu, W. Lu, S. Gao, Z. Liu and C. Lv, *RSC Adv.*, 2014, **4**, 6471-6477.
54. T. M. Klapötke, A. Penger, C. Pfluger, J. Stierstorfer and M. Suceska, *Eur. J. Inorg. Chem.*, 2013, **2013**, 4667-4678.

55. T. Altenburg, T. M. Klapötke, A. Penger and J. Stierstorfer, *Z. Anorg. Allg. Chem.*, 2010, **636**, 463-471.
56. D. E. Chavez, S. K. Hanson, J. M. Veauthier and D. A. Parrish, *Angew. Chem.*, 2013, **125**, 7014-7017.
57. R. Behrens and S. Bulusu, in *MRS Proc.*, Cambridge University Press, 1992, vol. 296, p. 13.
58. R. Behrens and S. Bulusu, *J. Phys. Chem.*, 1991, **95**, 5838-5845.
59. R. Behrens, *Chemistry and Physics of Energetic Materials*, ed. S. Bulusu, Springer, 1990, vol. 309, ch. 15, pp. 347-368.
60. J.-S. Lee, C.-K. Hsu and C.-L. Chang, *Thermochim. Acta*, 2002, **392–393**, 173-176.
61. A. C. Gonzalez, C. W. Larson, D. F. McMillen and D. M. Golden, *J. Phys. Chem.*, 1985, **89**, 4809-4814.
62. D. Chakraborty, R. P. Muller, S. Dasgupta and W. A. Goddard, *J. Phys. Chem. A*, 2000, **104**, 2261-2272.
63. D. Chakraborty, R. P. Muller, S. Dasgupta and W. A. Goddard, *J. Phys. Chem. A*, 2001, **105**, 1302-1314.
64. C. C. Chambers and D. L. Thompson, *J. Phys. Chem.*, 1995, **99**, 15881-15889.
65. R. V. Tsyshevsky, O. Sharia and M. M. Kuklja, *J. Phys. Chem. C*, 2013, **117**, 18144-18153.
66. R. Cohen, Y. Zeiri, E. Wurzberg and R. Kosloff, *J. Phys. Chem. A*, 2007, **111**, 11074-11083.
67. T. B. J. Brill, K. J., *Chem. Rev.*, 1993, **93**, 2667-2692.
68. T. B. Brill and K. J. James, *J. Phys. Chem.*, 1993, **97**, 8759-8763.
69. F. Jianfen and X. Heming, *J. Mol. Struct.: THEOCHEM*, 1996, **365**, 225-229.
70. J. S. Murray, P. Lane, P. Politzer and P. R. Bolduc, *Chem. Phys. Lett.*, 1990, **168**, 135-139.
71. C. Zhang, Y. Shu, Y. Huang, X. Zhao and H. Dong, *J. Phys. Chem. B*, 2005, **109**, 8978-8982.
72. P. Politzer and J. M. Seminario, *Chem. Phys. Lett.*, 1989, **158**, 463.
73. T. B. Brill and K. J. James, *J. Phys. Chem.*, 1993, **97**, 8752-8758.
74. A. G. Green and F. M. Rowe, *J. Chem. Soc.*, 1912, **101**, 2443.
75. A. G. Green and F. M. Rowe, *J. Chem. Soc.*, 1912, **101**, 2452.
76. R. V. Tsyshevsky, O. Sharia and M. M. Kuklja, *Molecules*, 2016, **21**, 236.
77. T. F. Moraes and I. Borges, *Int. J. Quantum Chem.*, 2011, **111**, 1444-1452.
78. E. A. Zhurova, A. I. Stash, V. G. Tsirelson, V. V. Zhurov, E. V. Bartashevich, V. A. Potemkin and A. A. Pinkerton, *J. Am. Chem. Soc.*, 2006, **128**, 14728-14734.
79. N. J. Harris and K. Lammertsma, *J. Am. Chem. Soc.*, 1997, **119**, 6583-6589.
80. F. J. Owens, K. Jayasuriya, L. Abrahmsen and P. Politzer, *Chem. Phys. Lett.*, 1985, **116**, 434-438.
81. K. B. Wiberg, *Tetrahedron*, 1968, **24**, 1083-1096.
82. O. V. Sizova, L. V. Skripnikov and A. Y. Sokolov, *J. Mol. Struct.: THEOCHEM*, 2008, **870**, 1-9.
83. Q. Cao, *J. Mol. Model.*, 2013, **19**, 2205-2210.
84. J. Fen, Z. Gu, H. Ziao and H. Dong, *J. Phys. Org. Chem.*, 1998, **11**, 177-184.
85. J. Li, *Propellants Explos. Pyrotech.*, 2008, **33**, 443-447.
86. Y. Pan, W. Zhu and H. Xiao, *Struct. Chem.*, 2013, **24**, 1071-1087.
87. J.-y. Zhang, H.-c. Du, F. Wang, X.-d. Gong and Y.-s. Huang, *J. Phys. Chem. A*, 2011, **115**, 6617-6621.

88.   X.-H. Li and X.-Z. Zhang, *Can. J. Chem.*, 2013, **91**, 369-374.

89.   X.-H. Li, R.-Z. Zhang, H.-L. Cui and Y.-L. Yong, *Chem. Heterocycl. Compd.*, 2015, **51**, 153-158.

90.   H.-f. Gao, S.-h. Zhang, F.-d. Ren, F. Liu, R.-j. Gou and X. Ding, *Comput. Mater. Sci.*, 2015, **107**, 33-41.

91.   X.-H. Li, R.-Z. Zhang and X.-Z. Zhang, *Can. J. Chem.*, 2013, **91**, 1213-1218.

92.   W.-G. Liu, S. V. Zybin, S. Dasgupta, T. M. Klapotke and W. A. Goddard III, *J. Am. Chem. Soc.*, 2009, **131**, 7490-7491.

93.   W. L. Ng, J. E. Field and H. M. Hauser, *J. Appl. Phys.*, 1986, **59**, 3945-3952.

94.   W. L. Ng, J. E. Field and H. M. Hauser, *J. Chem. Soc. Perkin II*, 1976, **0**, 637-639.

95.   Z. A. Akopyan, Y. T. Struchkov and V. G. Dashevskii, *J. Struct. Chem.*, 1966, **7**, 408.

96.   J. Nie, D. Xu, Z. Li and M. Chiang, *Acta Crystallogr. E*, 2001, **57**, 0827-0828.

97.   W. R. Carper, L. P. Davis and M. W. Extine, *J. Phys. Chem.*, 1982, **86**, 459-462.

98.   N. I. Golovina, A. N. Titkov, A. V. Raevskii and L. O. Atovmyan, *J. Solid State Chem.*, 1994, **113**, 229-238.

99.   R. M. Vrcelj, J. N. Sherwood, A. R. Kennedy, H. G. Gallagher and T. Gelbrich, *Cryst. Growth Des.*, 2003, **3**, 1027-1032.

100.   J. Bryden, *Acta Crystallogr. B*, 1972, **28**, 1395-1398.

101.   A. Anthony, G. R. Desiraju, R. K. R. Jetti, S. S. Kuduva, N. N. L. Madhavi, A. Nangia, R. Thaimattam and V. R. Thalladi, *Cryst. Eng.*, 1998, **1**, 1-18.

102.   K. Amimoto and H. Nishiguchi, *Acta Crystallogr. E*, 2013, **E69**, o425.

103.   N. Okabe, T. Nakamura and H. Fukuda, *Acta Crystallogr. C*, 1993, **C49**, 1678-1680.

104.   J. L. Wardell, J. N. Low and C. Glidewell, *Acta Crystallogr. C*, 2006, **C62**, o318-o320.

105.   J. R. Holden and C. Dickinson, *J. Phys. Chem.*, 1972, **76**, 3597-3602.

106.   Y. Kohno, R. I. Hiyoshi, Y. Yamaguchi, S. Matsumoto, A. Koseki, O. Takahashi, K. Yamasaki and K. Ueda, *J. Phys. Chem. A*, 2009, **113**, 2551-2560.

107.   H. H. Cady and A. C. Larson, *Acta Crystallogr.*, 1965, **18**, 485.

108.   C. Dickinson, J. M. Stewart and J. R. Holden, *Acta Crystallogr.*, 1966, **21**, 663-670.

109.   S. V. Rosokha, J. J. Lu, S. M. Dibrov and J. K. Kochi, *Acta Crystallogr. C*, 2006, **C62**, o464-o466.

110.   S. K. Bhattacharjee and H. L. Ammon, *Acta Crystallogr. B*, 1981, **37**, 2082-2085.

111.   F. Iwasaki and Y. Kawano, *Acta Crystallogr.*, 1977, **B33**, 2455-2459.

112.   T. Kagawa, R. Kawai, S. Kashino and M. Haisa, *Acta Crystallogr. B*, 1976, **B32**, 3171-3175.

113.   F. Iwasaki, M. Sato and A. Aihara, *Acta Crystallogr. B*, 1976, **32**, 102-106.

114.   T. Kolev, M. Berkei, C. Hirsch, H. Preut, P. Bleckmann and V. Radomirska, *Z. Kristallogr. NCS*, 2000, **215**, 483-484.

115.   Y. Sun, Z. Ren and W. Meng, *Asian J. Chem.*, 2013, **25**, 6186-6188.

116.   R. J. Butcher, R. Gilardi, J. L. Flippen-Anderson and C. George, *New J. Chem.*, 1992, **16**, 679-692.

117.   J. Trotter and C. S. Williston, *Acta Crystallogr.*, 1966, **21**, 285-288.

118.   J. Trotter, *Acta Crystallogr.*, 1960, **13**, 95-99.

119.   S. C. Nyburg, C. H. Faerman and L. Prasad, *Acta Crystallogr.*, 1987, **C43**, 686-689.

120.   G. Wójcik, I. Mossakowska, J. Holband and W. Bartkowiak, *Acta Crystallogr. B*, 2002, **B58**, 998-1004.

121. P. K. Thallapally, R. K. R. Jetti, A. K. Katz, H. L. Carrell, K. Singh, K. Lahiri, S. Kotha, R. Boese and G. R. Desiraju, *Angew. Chem., Int. Ed.*, 2004, **43**, 1149-1155.
122. E. Hertel and G. H. Romer, *Z. Physik. Chem.*, 1933, **B22**, 267-279.
123. J. C. Barnes, J. A. Chudek, R. Foster, F. Jarrett, F. Mackie, J. Paton and D. R. Twiselton, *Tetrahedron*, 1984, **40**, 1595-1601.
124. C. M. Gramaccioli, R. Destro and M. Simonetta, *Acta Crystallogr. B*, 1968, **24**, 129-136.
125. J. S. Willis, J. M. Stewart, H. L. Ammon, H. S. Preston, R. E. Gluyas and P. M. Harris, *Acta Crystallogr. B*, 1971, **27**, 786-793.
126. A. L. Rheingold, C. J. Balacchini and C. W. Grote, *J. Crystallogr. Spectrosc. Res.*, 1989, **19**, 25-37.
127. M. Roháč, S. Zeman and A. Růžička, *Chem. Mater.*, 2008, **20**, 3105-3109.
128. K. G. Shipp, *J. Org. Chem.*, 1964, **29**, 2620-2623.
129. A. Cousson, J. Lelievre, A. P. Chatrousse, F. Terrier and P. G. Farrell, *Acta Crystallogr. C*, 1993, **49**, 609-612.
130. S. Furberg and P. Larssen, *Acta Chem. Scand.*, 1952, **6**, 965-966.
131. H. Huang, Z. Zhou, J. Song, L. Liang, K. Wang, D. Cao, W. Sun, X. Dong and M. Xue, *Chem. Eur. J.*, 2011, **17**, 13593-13602.
132. H. Ma, J. Song, F. Zhao, H. Gao and R. Hu, *Chin. J. Chem.*, 2008, **26**, 1997-2002.
133. R. D. Gilardi and R. J. Butcher, *Acta Crystallogr. A*, 2001, **57**, o657-o658.
134. M. Ciechanowicz-Rutkowska, *J. Solid State Chem.*, 1977, **22**, 185-192.
135. J. R. Holden and C. Dickinson, *J. Chem. Soc. D*, 1969, **0**, 144-144.
136. Y. Kohno, K. Mori, R. I. Hiyoshi, O. Takahashi and K. Ueda, *Chem. Phys.*, 2016, **472**, 163-172.
137. I. V. Fedyanin and K. A. Lyssenko, *CrystEngComm*, 2013, **15**, 10086-10093.
138. W. Zhu, T. Wei, X. Zhang and H. Xiao, *J. Mol. Struct.: THEOCHEM*, 2009, **895**, 131-137.
139. L. Xiao-Hong and Z. Xian-Zhou, *Comput. Theor. Chem.*, 2011, **963**, 34-39.
140. P. C. Chen and S. C. Tzeng, *J. Mol. Struct.: THEOCHEM*, 1999, **467**, 243-257.
141. P. C. Hariharan, W. S. Koski and J. J. Kaufman, *Int. J. Quantum Chem.*, 1983, **23**, 1493-1504.
142. M.-J. Huang and J. Leszczynski, *J. Mol. Struct.: THEOCHEM*, 2002, **592**, 105-113.
143. G. Wang, X. Gong, Y. Liu and H. Xiao, *Int. J. Quantum Chem.*, 2010, **110**, 1691-1701.
144. J. Clarkson, W. E. Smith, D. N. Batchelder, D. A. Smith and A. M. Coats, *J. Mol. Struct.*, 2003, **648**, 203-214.
145. D. D. Sharipov, D. L. Egorov, D. V. Chachkov, A. G. Shamov and G. M. Khrapkovskii, *Russ. J. Gen. Chem.*, 2011, **81**, 2273-2287.
146. Z. Chaoyang, S. Yuanjie, Z. Xiaodong, D. Haishan and W. Xinfeng, *J. Mol. Struct.: THEOCHEM*, 2005, **728**, 129-134.
147. J. Chandrasekaran, S. Balaprabhakaran and B. Babu, *Optik*, 2013, **124**, 4296-4299.
148. V. Bertolasi, P. Gilli and G. Gilli, *Cryst. Growth Des.*, 2011, **11**, 2724-2735.
149. M. J. Kamlet and H. G. Adolph, *Propellants Explos. Pyrotech.*, 1979, **4**, 30-34.
150. R. Boese, D. Bläser, M. Nussbaumer and T. M. Krygowski, *Struct. Chem.*, 1992, **3**, 363-368.
151. F. W. Mackison, R. S. Stricoff and L. J. Partridge Jr., *Occupational Health Guielines for Chemical Hazards*, The National Institute for Occupational Safety and Health, Washington, D.C., 1981.
152. B. M. Rice and J. J. Hare, *J. Phys. Chem. A*, 2002, **106**, 1770-1783.

153. M. Vaullerin and A. Espagnacq, *Propellants Explos. Pyrotech.*, 1998, **23**, 237-239.
154. D. E. Bliss, S. L. Christian and W. S. Wilson, *J. Energ. Mater.*, 1991, **9**, 319-345.
155. D. Mathieu and T. Alaime, *J. Phys. Chem. A*, 2014, **118**, 9720-9726.
156. P. J. Davies and A. Provatas, *Characterization of 2,4-Dinitroanisole: An Ingredient for use in Low Sensitivity Melt Cast Formulations*, Weapons Defense Division, Edinburgh South Australia, Australia, 2006.
157. J. Li, *J. Phys. Chem. B*, 2010, **114**, 2198-2202.
158. H. D. Mallory, *The Development of Impact Sensitivity Tests at the Explosives Research Laboratory*, U.S. Naval Ordnance Laboratory, White Oak, Silver Spring, Maryland, 1956.
159. S. Zeman and M. Krupka, *Propellants Explos. Pyrotech.*, 2003, **28**, 249.
160. X. Hu, N. Chen and W. Li, *J. Mol. Model*, 2016, **22**, 170.
161. C. An, H. Li, X. Geng, J. Li and J. Wang, *Propellants Explos. Pyrotech.*, 2013, **38**, 172-175.
162. N. Zohari, M. H. Keshavarz and S. A. Seyedsadjadi, *J. Therm. Anal. Calorim.*, 2014, **117**, 423-432.
163. J. Zhang, P. Wu, Z. Yang, B. Gao, J. Zhang, P. Wang, F. Nie and L. Liao, *Propellants Explos. Pyrotech.*, 2014, **39**, 653-657.
164. B. M. Dobratz, P. C. Crawford and L. L. N. Laboratory, *LLNL Explosives Handbook: Properties of Chemical Explosives and Explosive Simulants*, Lawrence Livermore National Laboratory, University of California, 1985.
165. W. S. Wilson, D. E. Bliss, S. L. Christian and D. J. Knight, *Explosive Properties of Polynitroaromatics*, Naval Weapons Center, China Lake, CA, 1990.
166. X. Song, X. Cheng, X. Yang, D. Li and R. Linghu, *J. Haz. Mat.*, 2008, **150**, 317-321.
167. B. M. Rice, S. Sahu and F. J. Owens, *J. Mol. Struct.: THEOCHEM*, 2002, **583**, 69-72.
168. M. H. Keshavarz, *J. Haz. Mat.*, 2008, **153**, 201-206.
169. J. Harris, *Friction Sensitivity of Primary Explosives*, Army Armament Research and Development Command, Watervliet, NY, 1982.
170. P. Griess, *Philos. Trans. R. Soc. London*, 1864, **13**, 377.
171. D. Huang and G. Yan, *Adv. Synth. Catal.*, 2017, **359**, 1600-1619.
172. C. Gao, H. He, L. Zhou, X. Zheng and Y. Zhang, *Chem. Mater.*, 2009, **21**, 360-370.
173. P. Roger, L. Renaudie, C. Le Narvor, B. Lepoittevin, L. Bech and M. Brogly, *Eur. Polym. J.*, 2010, **46**, 1594-1603.
174. C. Bonini, L. Chiummiento, M. D. Bonis, M. Funicello, P. Lupattelli, G. Suanno, F. Berti and P. Campaner, *Tetrahedron*, 2005, **61**, 6580-6589.
175. H. Bock, R. Dammel and S. Aygen, *J. Am. Chem. Soc.*, 1983, **105**, 7681-7685.
176. J. P. Costantino, H. W. Richter, C. H. Lee Go and W. H. Waddell, *J. Am. Chem. Soc.*, 1985, **107**, 1744-1747.
177. C. H. Lee Go and W. H. Waddell, *J. Am. Chem. Soc.*, 1984, **106**, 715-718.
178. C. Wentrup and B. Freiermuth, *J. Anal. Appl. Pyrolysis*, 2016, **121**, 67-74.
179. W. H. Waddell and C. H. Lee Go, *J. Am. Chem. Soc.*, 1982, **104**, 5804-5805.
180. E. Gibney, *Nature*, 2016, **529**, 14-15.
181. C.-C. Chen and M. J. McQuaid, *J. Phys. Chem. A*, 2012, **116**, 3561-3576.
182. J. F. Arenas, J. I. Marcos, I. López-Tocón, J. C. Otero and J. Soto, *J. Chem. Phys.*, 2000, **113**, 2282.
183. J. F. Arenas, J. I. Marcos, J. C. Otero, A. Sánchez-Gálvez and J. Soto, *J. Chem. Phys.*, 1999, **111**, 551.

184. J. F. Arenas, J. C. Otero, A. Sánchez-Gálvez and J. Soto, *J. Phys. Chem. A*, 1998, **102**, 1146-1151.
185. P. Cardillo, L. Gigante, A. Lunghi, A. Fraleoni-Morgera and P. Zanirato, *New J. Chem.*, 2008, **32**, 47-53.
186. W.-H. Fang and G.-Q. Shao, *J. Mol. Struct.: THEOCHEM*, 1996, **369**, 183-188.
187. G. Rauhut and F. Eckert, *J. Phys. Chem. A*, 1999, **103**, 9086-9092.
188. M. Tho Nguyen, *Chem. Phys. Lett.*, 1985, **117**, 290-294.
189. M. Tho Nguyen, D. Sengupta and T.-K. Ha, *J. Phys. Chem.*, 1996, **100**, 6499-6503.
190. J. Yang, X. Gong and G. Wang, *Struct. Chem.*, 2015, **26**, 1077-1082.
191. A. M. Astakhov, R. S. Stepanov, L. A. Kruglyakova and A. A. Nefedov, *Russ. J. Org. Chem.*, 2001, **37**, 577-582.
192. G. L'Abbe and G. Mathys, *J. Org. Chem.*, 1974, **39**, 1778.
193. G. L'Abbé, A. Vandendriessche and S. Toppet, *Tetrahedron*, 1988, **44**, 3617-3626.
194. A. I. Lesnikovich, O. A. Ivashkevich, S. V. Levchik, A. I. Balabanovich, P. N. Gaponik and A. A. Kulak, *Thermochim. Acta*, 2002, **388**, 233-251.
195. M. Besora and J. N. Harvey, *J. Chem. Phys.*, 2008, **129**, 044303.
196. C. L. Currie and B. d. Darwent, *Can. J. Chem.*, 1963, **41**, 1552.
197. M. S. O'Dell and B. d. Darwent, *Can. J. Chem.*, 1970, **48**, 1140.
198. H. Bock and R. Dammel, *J. Am. Chem. Soc.*, 1988, **110**, 5261-5269.
199. H. Bock, R. Dammel and L. Horner, *Chem. Ber.*, 1981, **114**, 220-226.
200. H. Bock and R. Dammel, *Angew. Chem.*, 1987, **25**, 504-526.
201. M. T. Nguyen, D. Sengupta and T.-K. Ha, *J. Phys. Chem.*, 1996, **100**, 6499-6503.
202. J. F. Arenas, J. I. Marcos, J. C. Otero, I. L. Tocón and J. Soto, *Int. J. Quantum Chem.*, 2001, **84**, 241-248.
203. W. C. Lineberger and W. T. Borden, *Phys. Chem. Chem. Phys.*, 2011, **13**, 11792-11813.
204. N. R. Wijeratne, M. Da Fonte, A. Ronemus, P. J. Wyss, D. Tahmassebi and P. G. Wenthold, *J. Phys. Chem. A*, 2009, **113**, 9467-9473.
205. E. Özkaramete, N. Şenocak, K. E. İnal, S. Öz, I. Svoboda and O. Atakol, *Propellants Explos. Pyrotech.*, 2013, **38**, 113-119.
206. T. Takayama, M. Kawano, H. Uekusa, Y. Ohashi and T. Segawara, *Helv. Chim. Acta*, 2003, **86**, 1352.
207. C. M. Nunes, I. Reva, S. Kozuch, R. J. McMahon and R. Fausto, *J. Am. Chem. Soc.*, 2017, **139**, 17649-17659.
208. Y.-H. Joo and J. n. M. Shreeve, *Angew. Chem. Int. Ed.*, 2009, **48**, 564-567.
209. S. G. Cho, J. R. Cho, E. M. Goh, J.-K. Kim, R. Damavarapu and R. Surapaneni, *Propellants Explos. Pyrotech.*, 2005, **30**, 445-449.
210. Y. Zhang, D. A. Parrish and J. n. M. Shreeve, *J. Mater. Chem. A*, 2013, **1**, 585.
211. C. He, J. Zhang, D. A. Parrish and J. n. M. Shreeve, *J. Mater. Chem. A*, 2013, **1**, 2863.
212. P. Yin, J. Zhang, C. He, D. A. Parrish and J. n. M. Shreeve, *J. Mater. Chem. A*, 2014, **2**, 3200.
213. P. Yin, J. Zhang, D. A. Parrish and J. n. M. Shreeve, *Chem. Eur. J.*, 2014, **20**, 16529-16536.
214. P. Yin, Q. Zhang, J. Zhang, D. A. Parrish and J. n. M. Shreeve, *J. Mater. Chem. A*, 2013, **1**, 7500.
215. M. A. Kettner, T. M. Klapötke, T. G. Müller and M. Sućeska, *Eur. J. Inorg. Chem.*, 2014, **2014**, 4756-4771.

216. B. Krebs, J. Mandt, R. E. Cobbledick and R. W. H. Small, *Acta Crystallogr. B*, 1979, **35**, 402-404.
217. D. M. Laboureur, Z. Han, B. Z. Harding, A. Pineda, W. C. Pittman, C. Rosas, J. Jiang and M. S. Mannan, *J. Haz. Mat.*, 2016, **308**, 164-172.
218. J. Park and M. C. Lin, *J. Phys. Chem. A*, 2009, **113**, 13556-13561.
219. Y.-i. Izato and A. Miyake, *J. Therm. Anal. Calorim.*, 2015, **122**, 595-600.
220. Y. Yamamoto, S. Kubota, T. Saburi, Y. Wada and A. Miyake, *Appl. Mech. Mater.*, 2014, **556**, 385-390.
221. V. Babrauskas, *Fire and Mater.*, 2017, 1-9.
222. Y.-i. Izato, M. Koshi and A. Miyake, *Int. J. Chem. Kin.*, 2017, **49**, 83-99.
223. Y. A. Gruzdkov, Z. A. Dreger and Y. M. Gupta, *J. Phys. Chem.*, 2004, **108**, 6216.
224. E. F. C. Byrd and B. M. Rice, *J. Phys. Chem. C*, 2007, **111**, 2787-2796.
225. Z. Yu and E. R. Bernstein, *J. Chem. Phys.*, 2011, **135**, 154305.
226. D. Bedrov, J. B. Hooper, G. D. Smith and T. D. Sewell, *J. Chem. Phys.*, 2009, **131**, 034712.
227. M. J. Cawkwell, T. D. Sewell, L. Zheng and D. L. Thompson, *Phys. Rev. B*, 2008, **78**, 014107.
228. R. M. Eason and T. D. Sewell, *J. Phys. Chem. C*, 2012, **116**, 2226-2239.
229. D. Furman, R. Kosloff, F. Dubnikova, S. V. Zybin, W. A. Goddard, N. Rom, B. Hirshberg and Y. Zeiri, *J. Am. Chem. Soc.*, 2014, **136**, 4192-4200.
230. A. Pereverzev, T. D. Sewell and D. L. Thompson, *J. Chem. Phys.*, 2013, **139**, 044108-044107.
231. L. A. Rivera-Rivera, T. D. Sewell and D. L. Thompson, *J. Chem. Phys.*, 2013, **138**, 084512.
232. G. F. Velardez, S. Alavi and D. L. Thompson, *J. Chem. Phys.*, 2004, **120**, 9151-9159.
233. T.-T. Zhou and F.-L. Huang, *J. Phys. Chem. B*, 2011, **115**, 278-287.
234. T.-R. Shan, A. C. T. Van Duin and A. P. Thompson, *J. Phys. Chem. A*, 2014, **118**, 1469-1478.
235. D. C. Sorescu and D. L. Thompson, *J. Phys. Chem. A*, 2001, **105**, 720-733.
236. T. Giavani, H. Bildsøe, J. Skibsted and H. J. Jakobsen, *J. Phys. Chem. B*, 2002, **106**, 3026-3032.
237. J. R. Holden and C. W. Dickinson, *J. Phys. Chem.*, 1975, **79**, 249-256.
238. H. Yu, D. Duan, H. Liu, T. Yang, F. Tian, K. Bao, D. Li, Z. Zhao, B. Liu and T. Cui, *Sci. Rep.*, 2016, **6**, 1-9.
239. X. Zhang and X. Gong, *J. Comput. Aided Mol. Des.*, 2015, **29**, 471-483.
240. G. Wang, X. Gong, Y. Liu, H. Du, X. Xu and H. Xiao, *J. Haz. Mat.*, 2010, **177**, 703-710.
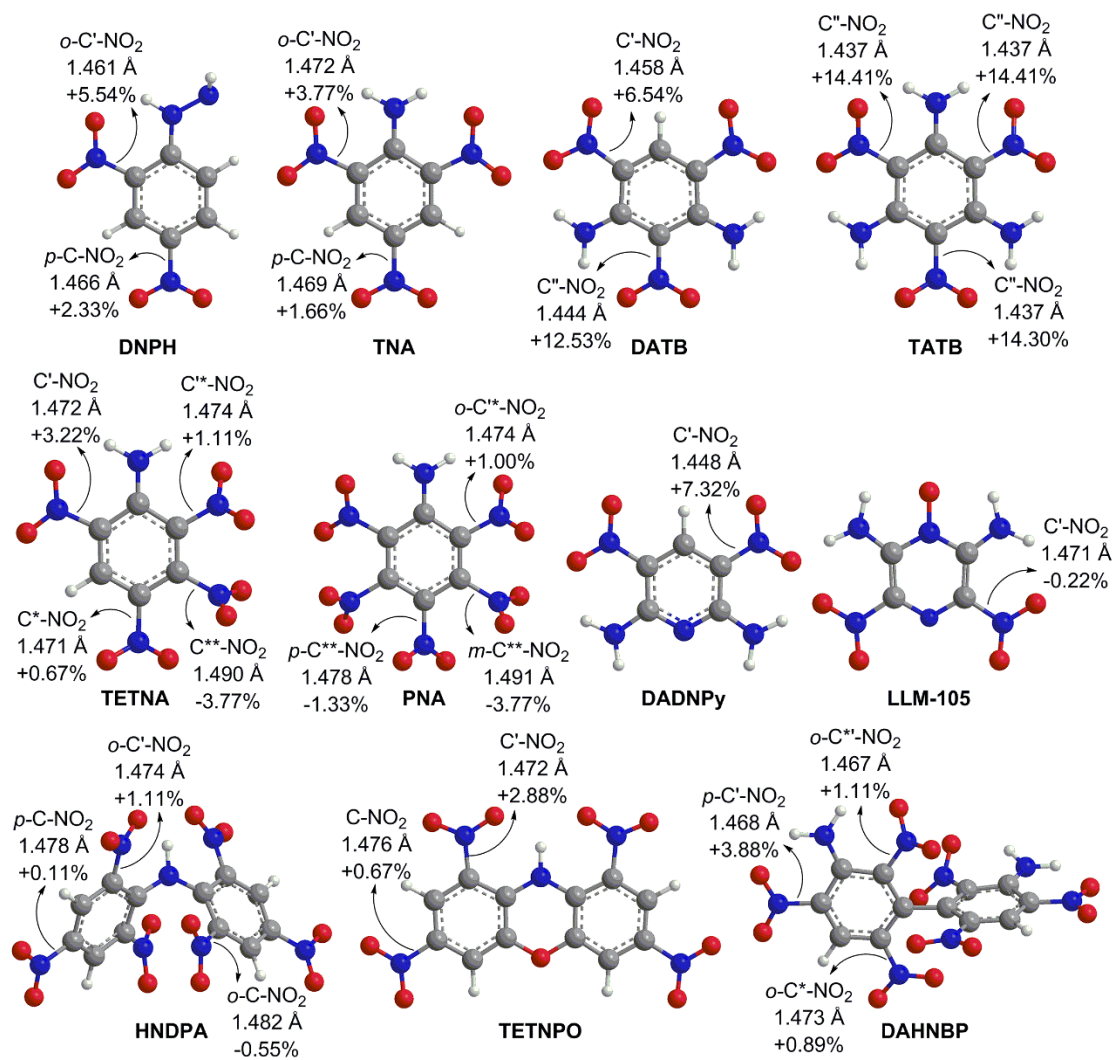
APPENDICES
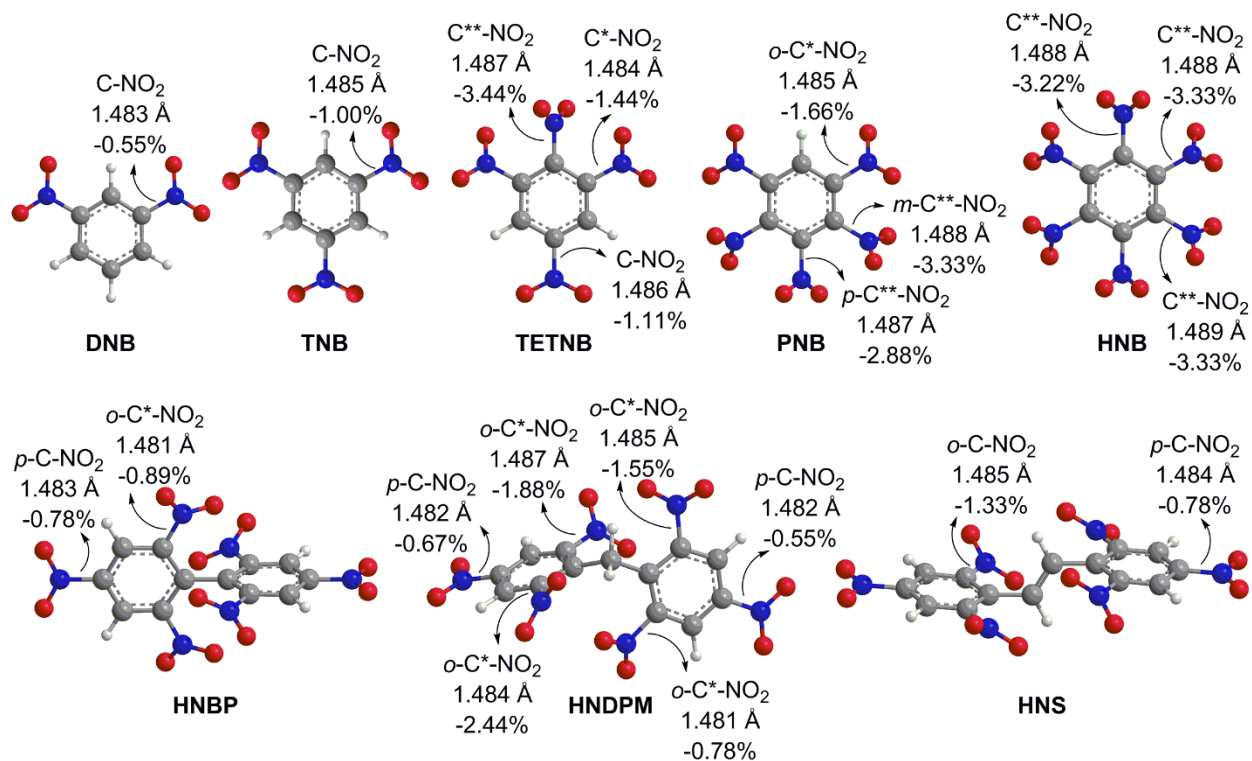
Figure A1. DFT(M06-2X)/TZVP optimized structures of the nitrobenzenes with selected bond distances (Å) and %ΔWBIs (%) labeled based on descriptions in **Table 2**.
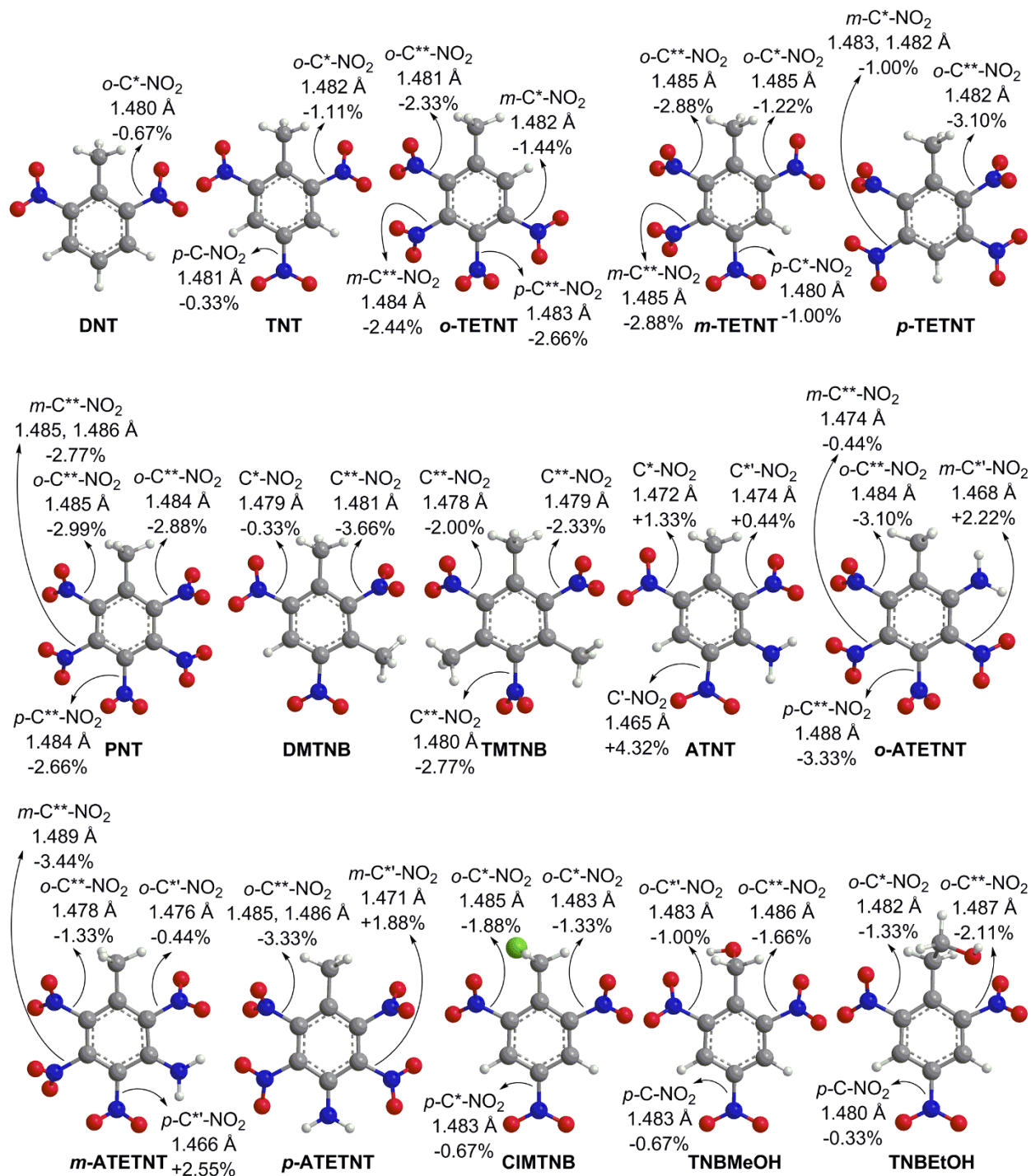
Figure A2. DFT(M06-2X)/TZVP optimized structures of the nitrobenzyls with selected bond distances (Å) and %ΔWBIs (%) labeled based on descriptions in **Table 2**.
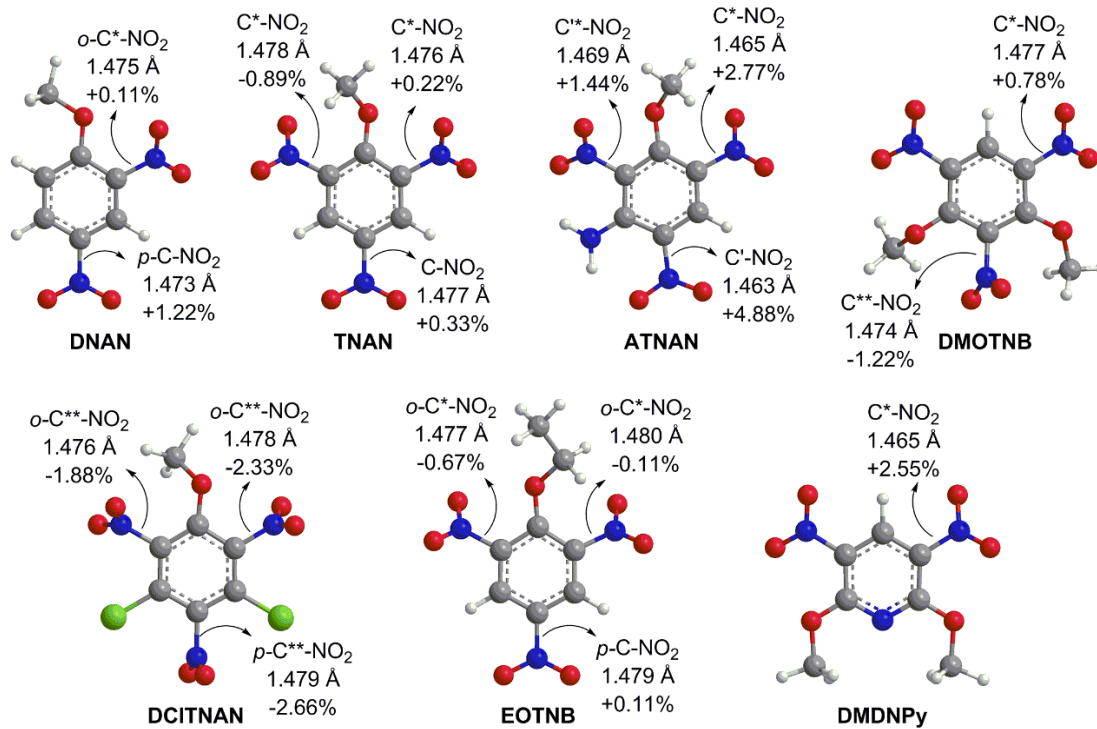
Figure A3. DFT(M06-2X)/TZVP optimized structures of the nitroanisoles with selected bond distances (Å) and %ΔWBIs (%) labeled based on descriptions in **Table 2**.

Figure A4. DFT(M06-2X)/TZVP optimized structures of the nitroanilines with selected bond distances (Å) and %ΔWBIs (%) labeled based on descriptions in **Table 2**.
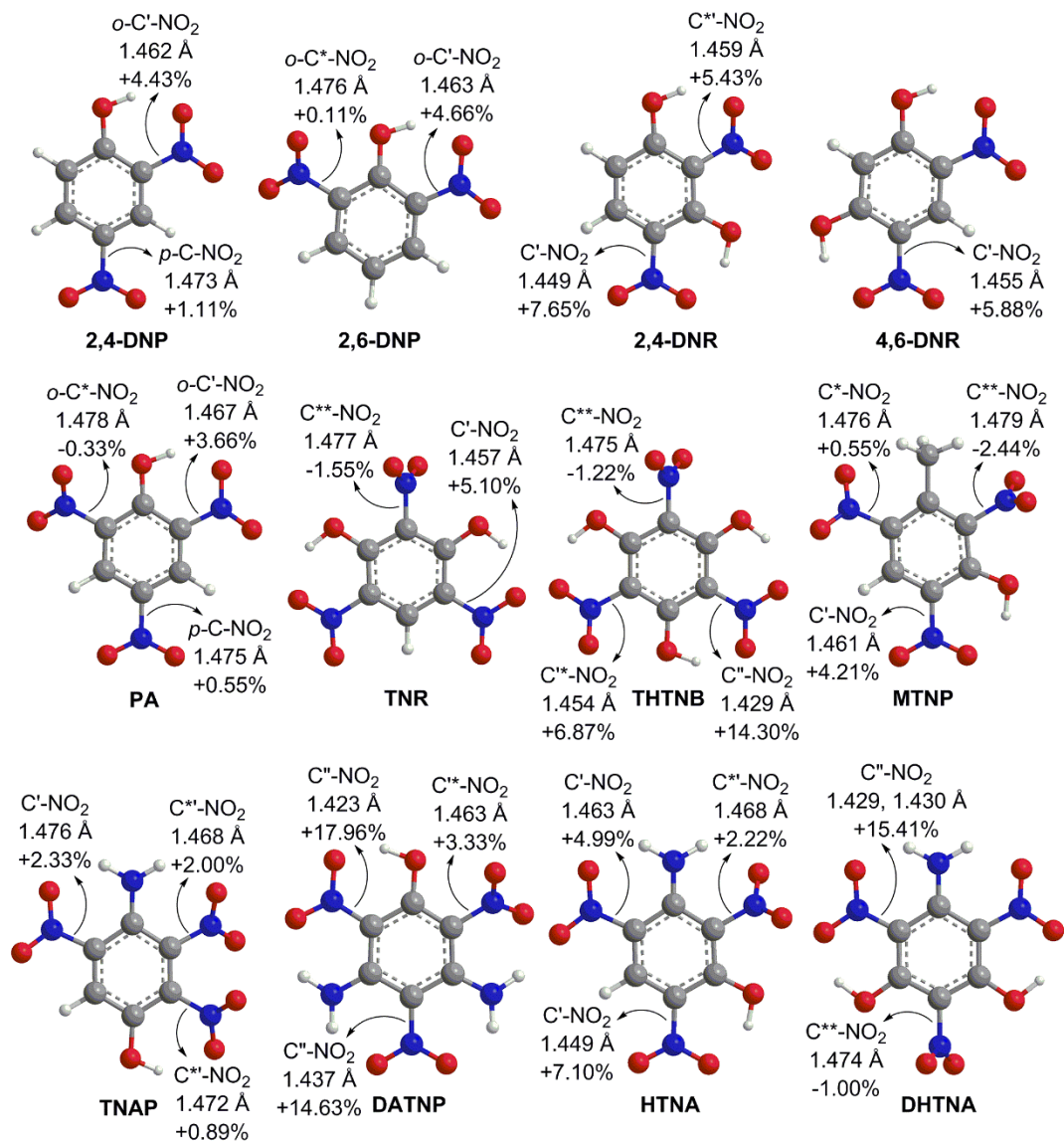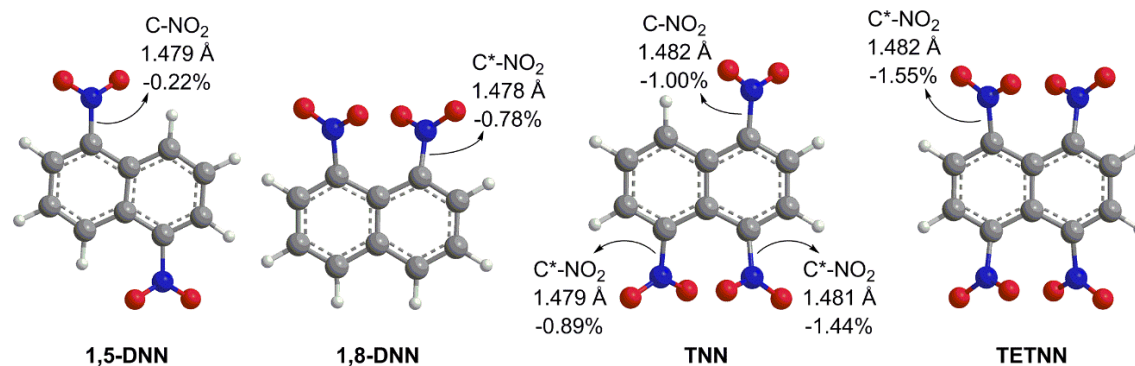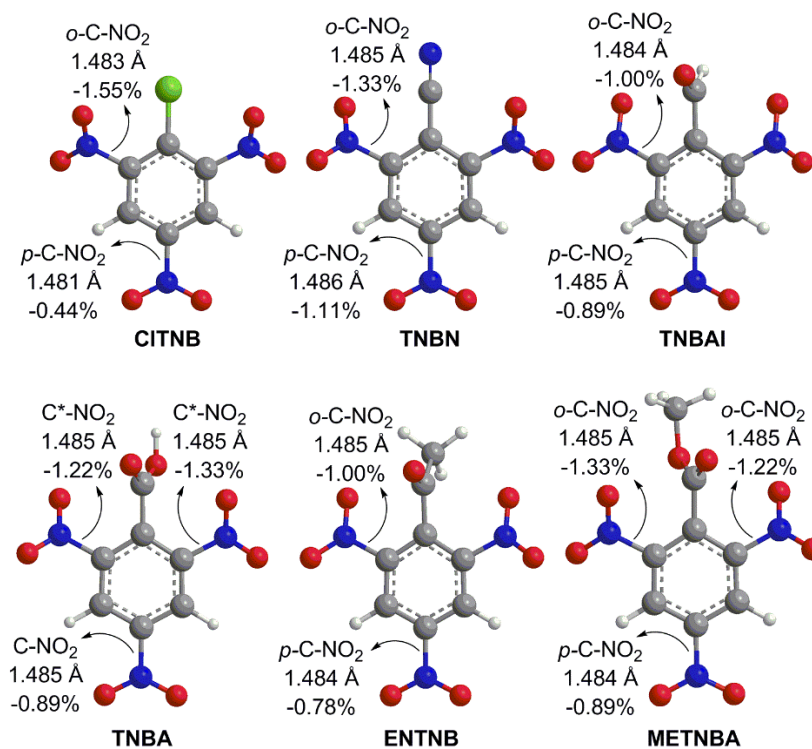
Figure A5. DFT(M06-2X)/TZVP optimized structures of the nitrophenols with selected bond distances (Å) and %ΔWBIs (%) labeled based on descriptions in **Table 2**.

Figure A6. DFT(M06-2X)/TZVP optimized structures of the nitronaphthalenes with selected bond distances (Å) and %ΔWBIs (%) labeled based on descriptions in **Table 2**.

Figure A7. DFT(M06-2X)/TZVP optimized structures of the miscellaneous energetic materials with selected bond distances (Å) and %ΔWBIs (%) labeled based on descriptions in **Table 2**.
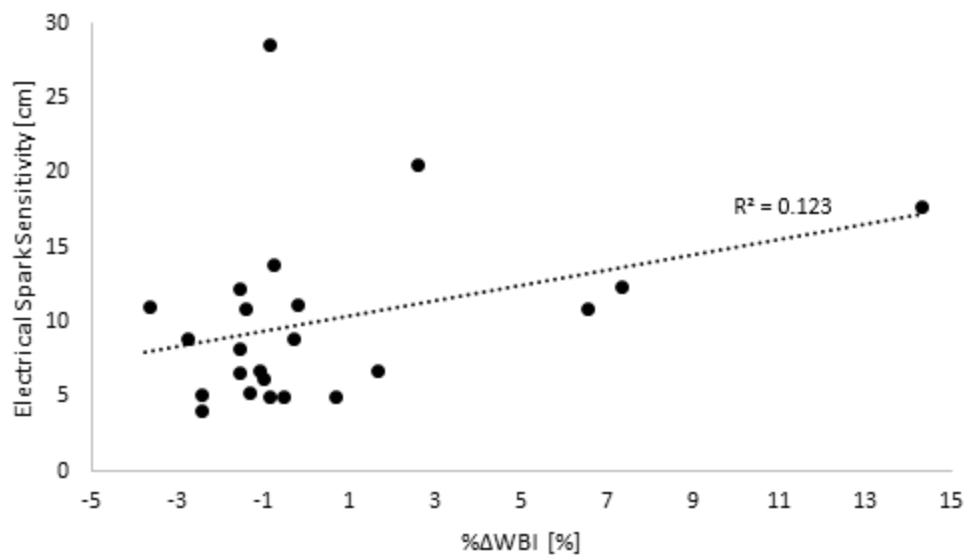
Figure A8. Correlation between %ΔWBIs (from **Table 2**) and experimental electrical spark sensitivity (from **Table A1**).

Table A1. Comparison of available previous theoretical and DFT(M06-2X)/TZVP BDEs with experimental electrical spark sensitivities and zero point energies of the nitroaromatic energetic materials. Trigger bonds assigned by %ΔWBIs are designated by *italics* as necessary.

Compound	Bond	$BDE_{DFT(M06-2X/TZVP)}$ [kcal/mol]	BDE_{DFT} [kcal/mol]	E.S. [J][168]	ZPE [Hartree/Particle]
Reference					
NB	C-NO$_2$	73.63	N/A	N/A	-436.610908
Nitrobenzenes					
DNB	C-NO$_2$	74.86	N/A	N/A	-641.101435
TNB	C-NO$_2$	68.43	66.47[a], 67.93[b], 64.0[c]	6.31	-845.590220
TETNB	C**-NO$_2$	*55.57*	52.75[a], 54.49[b], 50.3[c]	N/A	-1050.043200
	C*-NO$_2$	62.25			
	C-NO$_2$	66.94			
PNB	*o*-C-NO$_2$	60.70	51.96[a], 53.59[b]	N/A	-1254.500294
	m-C-NO$_2$	*55.88*			
	p-C-NO$_2$	58.81			
HNB	C-NO$_2$	53.15	50.1[c]	N/A	-1458.958418
HNBP	*o*-C-NO$_2$	*66.50*	66.71[a], 68.28[b]	5.03	-1689.985689
	p-C-NO$_2$	68.05			
HNDPM	*o*-C-NO$_2$	*60.31*	N/A	4.1	-1729.259440
	p-C-NO$_2$	68.47			
HNS	*o*-C-NO$_2$	*63.60*	N/A	5.32	-1767.340457
	p-C-NO$_2$	68.01			
Nitrobenzyls					
DNT	*o*-C-NO$_2$	65.62	68.15[f]	N/A	-680.374779
TNT	*o*-C-NO$_2$	*64.67*	61.38[a], 62.98[b], 58.9[c]	6.85	-884.861064
	p-C-NO$_2$	69.69			
o-TETNT	*o*-C-NO$_2$	60.73	N/A	N/A	-1089.317043
	m-C**-NO$_2$	58.65			
	p-C-NO$_2$	*57.09*			
	m-C*-NO$_2$	61.53			
m-TETNT	*o*-C**-NO$_2$	*59.15*	61.12[f]	N/A	-1089.321274
	m-C-NO$_2$	*57.16*			
	p-C-NO$_2$	60.99			
p-TETNT	*o*-C*-NO$_2$	62.53	N/A	N/A	-1089.323228
	o-C-NO$_2$	*58.66*			
	m-C-NO$_2$	63.10			
PNT	*o*-C-NO$_2$	*58.44*	54.83[f]	N/A	-1293.783121
	m-C-NO$_2$	57.49			
	p-C-NO$_2$	56.78			
DMTNB	C**-NO$_2$	*63.08*	65.60[f]	11.11	-924.140676
	C*-NO$_2$	66.69			
TMTNB	C-NO$_2$	65.27	62.23[f]	8.98	-963.420204
ATNT	C*'-NO$_2$	*64.66*	64.84[a], 66.52[b]	N/A	-940.210287
	C'-NO$_2$	71.48			
	C*-NO$_2$	68.19			

Table A1 (continued)

Compound	Bond	BDE$_{DFT(M06-2X/TZVP)}$ [kcal/mol]	BDE$_{DFT}$ [kcal/mol]	E.S. [J][168]	ZPE [Hartree/Particle]
o-ATETNT	*o*-C-NO$_2$	59.82	N/A	N/A	-1144.665440
	m-C**-NO$_2$	62.18			
	p-C-NO$_2$	*55.76*			
m-ATETNT	*m*-C*'-NO$_2$	64.96	N/A	N/A	-1144.670534
	o-C**-NO$_2$	61.88			
	m-C-NO$_2$	*54.96*			
	p-C-NO$_2$	64.02			
p-ATETNT	*o*-C*'-NO$_2$	63.67	N/A	N/A	-1144.670494
	o-C-NO$_2$	*57.43*			
	m-C-NO$_2$	63.83			
ClMTNB	*o*-C-NO$_2$	*61.59*	N/A	N/A	-1344.456126
	p-C-NO$_2$	68.26			
TNBMeOH	*o*-C-NO$_2$	*62.07*	N/A	N/A	-960.069545
	p-C-NO$_2$	68.34			
TNBEtOH	*o*-C-NO$_2$	*65.42*	N/A	N/A	-999.354215
	p-C-NO$_2$	69.56			
Nitroanisoles					
DNAN	*o*-C-NO$_2$	*66.63*	N/A	N/A	-755.580151
	p-C-NO$_2$	73.00			
TNAN	*o*-C-NO$_2$	*64.86*	N/A	28.59	-960.054480
	p-C-NO$_2$	*69.28*			
ATNAN	C'*-NO$_2$	*62.84*	N/A	N/A	-1015.406142
	C'-NO$_2$	72.53			
	C*-NO$_2$	69.24			
DMOTNB	C**-NO$_2$	*56.71*	53.56[a], 54.04[b]	N/A	-1074.528971
	C*-NO$_2$	61.54			
DClTNAN	*o*-C-NO$_2$	63.04	N/A	N/A	-1879.229241
	p-C-NO$_2$	*61.30*			
EOTNB	*o*-C-NO$_2$	*61.42*	N/A	N/A	-999.339180
	p-C-NO$_2$	71.98			
DMDNPy	C-NO$_2$	68.65	N/A	20.57	-886.130503
Nitroanilines					
DNPH	*o*-C-NO$_2$	74.71	N/A	N/A	-751.746974
	p-C-NO$_2$	*75.27*			
TNA	*o*-C-NO$_2$	70.02	70.51[a], 72.06[b], 66.5[c], 66.49[d]	6.85	-900.937800
	p-C-NO$_2$	*72.02*			
DATB	C'-NO$_2$	*73.27*	72.39[a], 75.00[b], 69.2[c], 69.89[d]	10.97	-956.285840
	C''-NO$_2$	71.30			
TATB	C-NO$_2$	72.49	84.80[a], 88.50[b], 69.4[c], 74.09[d]	17.75	-1011.630059
TETNA	C'-NO$_2$	63.49	48.1[c]	N/A	-1105.394849
	C*-NO$_2$	53.95			
	C**-NO$_2$	*65.67*			
	C'*-NO$_2$	68.63			

Table A1 (continued)

Compound	Bond	BDE$_{DFT(M06-2X/TZVP)}$ [kcal/mol]	BDE$_{DFT}$ [kcal/mol]	E.S. [J][168]	ZPE [Hartree/Particle]
PNA	o-C-NO$_2$	62.78	57.29[a], 59.18[b], 47.1[c]	N/A	-1309.852902
	m-C-NO$_2$	54.98			
	p-C-NO$_2$	61.40			
DADNPy	C-NO$_2$	76.48	N/A	12.4	-767.867396
LLM-105	C-NO$_2$	68.13	65.44[a], 67.57[b], 83.34[e]	N/A	-859.059426
HNDPA	o-C'-NO$_2$	67.25	65.77[a], 67.83[b]	5.02	-1745.323580
	p-C-NO$_2$	69.25			
	o-C-NO$_2$	62.65			
TETNPO	C'-NO$_2$	69.19	N/A	5.12	-1410.409137
	C-NO$_2$	70.63			
DAHNBP	o-C*-NO$_2$	66.05	65.77[a], 67.83[b]	N/A	-1800.686625
	p-C'-NO$_2$	70.03			
	o-C*'-NO$_2$	71.29			
Nitrophenols					
2,4-DNP	o-C-NO$_2$	67.12	72.42[g]	N/A	-716.331858
	p-C-NO$_2$	65.33			
2,6-DNP	C-NO$_2$	67.13	N/A	N/A	-716.319900
2,4-DNR	C*'-NO$_2$	79.84	N/A	N/A	-791.550646
	C'-NO$_2$	71.16			
4,6-DNR	C-NO$_2$	75.41		N/A	-791.561651
PA	o-C*-NO$_2$	64.52	60.1[c]	8.98	-920.806846
	p-C-NO$_2$	70.86			
	o-C'-NO$_2$	72.48			
TNR	C'-NO$_2$	74.69	62.07[g]	12.3	-996.033185
	C**-NO$_2$	64.89			
	C'*-NO$_2$	70.50			
THTNB	C''-NO$_2$	77.50	67.67[g]	N/A	-1071.249766
	C**-NO$_2$	64.84			
MTNP	C**-NO$_2$	63.01	N/A	5.21	-960.086992
	C'-NO$_2$	73.74			
	C*-NO$_2$	67.32			
TNAP	C*'-NO$_2$	68.42	62.8[c]	N/A	-976.140296
	C*'-NO$_2$	61.96			
	C'-NO$_2$	61.94			
DATNP	C''-NO$_2$	77.06	66.90[a], 69.14[b]	N/A	-1031.505530
	C''-NO$_2$	72.82			
	C'*-NO$_2$	68.27			
HTNA	C*'-NO$_2$	66.77	65.56[a], 67.61[b]	N/A	-976.159238
	C'-NO$_2$	76.20			
	C'-NO$_2$	71.75			
DHTNA	C''-NO$_2$	76.40	N/A	N/A	-1051.380147
	C**-NO$_2$	65.72			
Nitronaphthalenes					
1,5-DNN	C-NO$_2$	67.72	N/A	11.2	-794.672531
1,8-DNN	C-NO$_2$	63.25	N/A	13.9	-794.668024

Table A1 (continued)

Compound	Bond	BDE$_{DFT(M06-2X/TZVP)}$ [kcal/mol]	BDE$_{DFT}$ [kcal/mol]	E.S. [J][168]	ZPE [Hartree/Particle]
TNN	C*-NO$_2$	62.12			
	C*-NO$_2$	*60.47*	N/A	10.97	-999.150230
	C-NO$_2$	65.59			
TETNN	C-NO$_2$	59.57	N/A	8.26	-1203.625458
Miscellaneous					
ClTNB	*o*-C-NO$_2$	*61.56*	N/A	6.71	-1305.165985
	p-C-NO$_2$	68.20			
TNBN	*o*-C-NO$_2$	*61.87*	57.0*c*	N/A	-937.802013
	p-C-NO$_2$	66.94			
TNBAl	*o*-C-NO$_2$	*64.51*	N/A	N/A	-958.879415
	p-C-NO$_2$	67.68			
TNBA	*o*-C-NO$_2$	*65.02*	N/A	N/A	-1034.132395
	p-C-NO$_2$	67.62			
ENTNB	*o*-C-NO$_2$	*65.79*	N/A	N/A	-998.172241
	p-C-NO$_2$	68.11			
METNBA	*o*-C-NO$_2$	*65.62*	N/A	N/A	-1073.399457
	p-C-NO$_2$	68.02			

*a*Calculations completed using UB3LYP/6-31G**.[157]

*b*Calculations performed at UB3P86/6-31G**.[157]

*c*Calculations completed using B3LYP/6-31G*.[167]

*d*Calculations performed at B3LYP/6-31G*.[239]

*e*Calculations completed using B3LYP/6-311++G**.[132]

*f*Calculations performed at B3LYP/6-31G*.[240]

*g*Calculations completed using B3LYP/6-31G*.[143]

Energetic materials with ' indicate the number of hydrogen bonding interactions and * indicate the number of steric effects and/or repulsions.
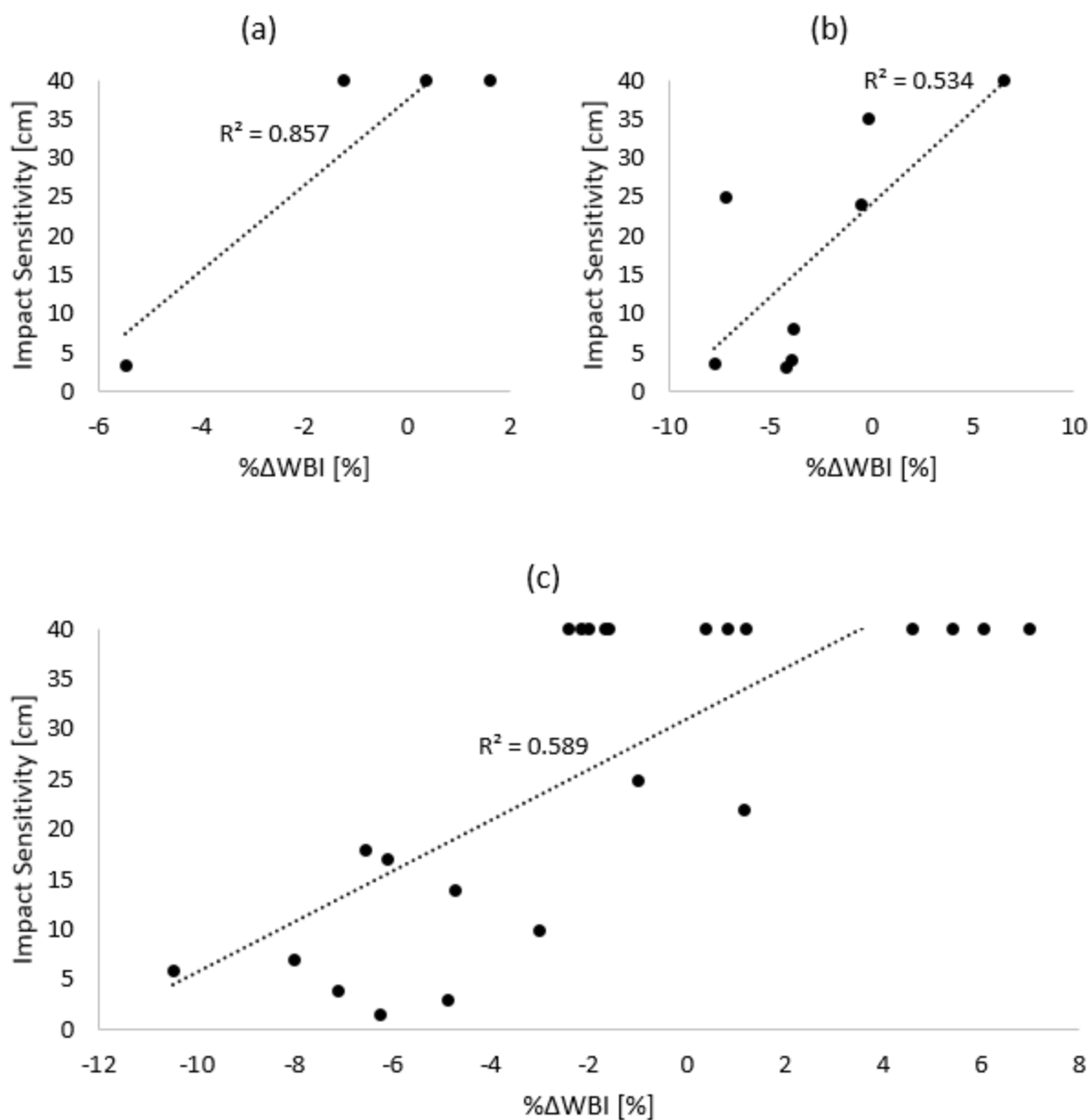
Figure A9. Correlations between %ΔWBIs and experimental impact sensitivities (cm) (**Table 5**) for the (a) imidazoles, (b) triazoles and (c) pyrazoles.

VITA

Ashley Lauren Shoaf

Department of Chemistry and Biochemistry

Old Dominion University

Norfolk, VA 23529

Education

Ph.D., Old Dominion University, Norfolk, VA, December 2018

B.S., Palm Beach Atlantic University, West Palm Beach, FL, May 2013

Professional Experience

Research Assistant for Dr. Craig A. Bayse and Teaching Assistant (ODU), 2013 – 2018

ODU College of Sciences Graduate Dominion Scholar Recipient, 2016 – 2018

Graduate Research Fellowships through the Virginia Space Grant Consortium, 2016 – 2018

Publications

Shoaf, Ashley L.; Bayse, Craig A. *J. Comp. Chem.* **2018**, *39*, 1236-1248.

Shoaf, Ashley L.; Bayse, Craig A. *New J. Chem.* **2016**, *40*, 413-422.

Harper, Lenora K.; Shoaf, Ashley L.; Bayse, Craig A. *ChemPhysChem* **2015**, *16*, 3886-3892.

Bayse, Craig A.; Shoaf, Ashley L. *Molecules* **2015**, *20*, 10244-10252.

Presentations

Shoaf, A. L.; Bayse, C. A. 250th ACS National Meeting in Boston, MA, August 16-20, 2015.

Shoaf, A. L.; Bayse, C. A. Gordon Research Conference on Energetic Materials in Stowe, VT, June 5-10, 2016.

Shoaf, A. L.; Bayse, C. A. SERMACS in Charlotte, North Carolina, November 7-11, 2017.

Shoaf, A. L.; Bayse, C. A. 255th ACS National Meeting in New Orleans, LA, March 18-22, 2018.